

MMC FILE COPY

1

INVESTIGATION OF THE IMPACT PERFORMANCE  
OF VARIOUS GLASS AND CERAMIC SYSTEMS

AD-A202 443

Principal Investigator Dr J.E. Field

August 1988

FINAL TECHNICAL REPORT

UNITED STATES ARMY  
EUROPEAN RESEARCH OFFICE OF THE U.S. ARMY,  
LONDON, ENGLAND.

CONTRACT NUMBER DAJA45-85-C-0021

DTIC  
ELECTE  
S DEC 01 1988 D  
D

Cavendish Laboratory,  
Department of Physics,  
University of Cambridge,  
Madingley Road,  
Cambridge CB3 0HE, U.K.

Approved for Public Release; distribution unlimited

Best Available Copy

88 12 1 045

Unclassified

SECURITY CLASSIFICATION OF THIS PAGE

ADA202443

REPORT DOCUMENTATION PAGE				Form Approved OMB No 0704 0188 Exp Date Jun 30 1986	
1a REPORT SECURITY CLASSIFICATION Unclassified			1b RESTRICTIVE MARKINGS		
2a SECURITY CLASSIFICATION AUTHORITY			3 DISTRIBUTION / AVAILABILITY OF REPORT Approved for public release; distribution unlimited		
2b. DECLASSIFICATION / DOWNGRADING SCHEDULE					
4. PERFORMING ORGANIZATION REPORT NUMBER(S)			5. MONITORING ORGANIZATION REPORT NUMBER(S) R&D 5087-MS-01		
6a. NAME OF PERFORMING ORGANIZATION University of Cambridge		6b. OFFICE SYMBOL (if applicable)		7a. NAME OF MONITORING ORGANIZATION USARDSG-UK	
6c. ADDRESS (City, State, and ZIP Code) Cavendish Laboratory, Department of Physics Madingley Road, Cambridge, CB3 0HE, UK			7b. ADDRESS (City, State, and ZIP Code) Box 65 FPO NY 09510-1500		
8a. NAME OF FUNDING / SPONSORING ORGANIZATION USARDSG-UK ARO-E		8b. OFFICE SYMBOL (if applicable)		9. PROCUREMENT INSTRUMENT IDENTIFICATION NUMBER DAJA45-85-C-0021	
8c. ADDRESS (City, State, and ZIP Code) Box 65 FPO NY 09510-1500			10. SOURCE OF FUNDING NUMBERS		
			PROGRAM ELEMENT NO 61103A	PROJECT NO 1L161103BH5	TASK NO 04
11. TITLE (Include Security Classification) (U) Investigation of the Impact Performance of Various Glass and Ceramics Systems					
12. PERSONAL AUTHOR(S) Dr. J.E. Field					
13a. TYPE OF REPORT Final		13b. TIME COVERED FROM 3.7.85 TO 30.6.88		14 DATE OF REPORT (Year, Month, Day) 1988, August 31	
15 PAGE COUNT 45p + 50 figs.					
16. SUPPLEMENTARY NOTATION					
17. COSATI CODES			18. SUBJECT TERMS (Continue on reverse if necessary and identify by block number)		
FIELD	GROUP	SUB-GROUP			
11	02		CERAMICS, GLASSES, IMPACT, FRACTURE, TOUGHNESS. HARDNESS, HIGH SPEED PHOTOGRAPHY. (JES) ←		
19	09				
19. ABSTRACT (Continue on reverse if necessary and identify by block number)					
<p>This report describes our research on the impact behaviour of various glass and ceramic systems. The first section describes the liquid impact technique and experiments in which high velocity liquid jets were fired at specimens over a range of velocities and the "post impact" (i.e. "residual") strength measured. The jet technique is a convenient method for applying an intense stress pulse and studying the dynamic response of a material. If impact experiments are made over a range of velocities, it is possible to plot "residual" strength versus impact velocity. Such curves give the threshold velocity for damage and also show how rapidly the strength decreases for impacts above the threshold condition. Further, if the materials <math>K_{Ic}</math> is known, it is possible to calculate an "equivalent flaw" size. The residual strength curves obtained for the various materials are discussed. The second section describes a study of the impact behaviour of glass and ceramic materials when impacted by solids. It covers the</p>					
20. DISTRIBUTION / AVAILABILITY OF ABSTRACT <input checked="" type="checkbox"/> UNCLASSIFIED/UNLIMITED <input checked="" type="checkbox"/> SAME AS RPT. <input checked="" type="checkbox"/> DTIC USERS			21. ABSTRACT SECURITY CLASSIFICATION Unclassified		
22a. NAME OF RESPONSIBLE INDIVIDUAL Dr. Wilburn C. Simmons			22b. TELEPHONE (Include Area Code) 01-409 4423		22c. OFFICE SYMBOL AMXSN-UK-RM

DD FORM 1473, 84 MAR

83 APR edition may be used until exhausted  
All other editions are obsolete.SECURITY CLASSIFICATION OF THIS PAGE  
Unclassified

apparatus for projecting solid spheres, techniques and methods used to measure hardness, fracture toughness, acoustic velocities, and crack velocities, and gives high-speed photographic results of impacts. Projectile materials included steel, lead, and tungsten carbide spheres. The ceramics included various glass and alumina ceramics and boron carbide. In section 3, there is a discussion and analysis of the results, and in section 4 a summary of the main conclusions. The report summarises a large amount of data on the impact behaviour of a wide range of ceramic systems obtained using high speed photography, a momentum balance and post impact microscopy. Glass ceramics have the advantage of relatively low density compared with the aluminas so that for a given weight thicker samples can be used. This allows the base diameter of the cone of debris to be larger. However, their hardnesses are less than steel and they do not damage the projectile significantly. Experiments with layered systems have shown that a front plate of alumina or other hard material (if of sufficient thickness) can break up a steel projectile. Such systems can then use a lower hardness and/or cheaper backing ceramic. The cone not only spreads the load but produces fragments of relatively low velocity. It is reasonably easy to "catch" such material with a polymer fabric or composite. The work has shown that several of the properties of a ceramic are important. However, it appears that  $K_{Ic}$  is not particularly important. A key ratio is that of  $H/p$  where  $H$  is the hardness and  $p$  the density with the added restriction that the hardness of the ceramic needs to be greater than that of the projectile.

## TABLE OF CONTENTS

- 1.1 Introduction
- 1.2 The Water Jet Technique
- 1.3 Impact Damage in Brittle Materials
- 1.4 Impact Damage Assessment for Brittle Materials
- 1.5 A Comparison of the Liquid Impact Performance of Various Brittle Materials
- 1.6 Conclusions

- 2.1 Introduction
- 2.2 Apparatus
- 2.3 Materials Description:
  - 2.3.1 Crack Velocity
  - 2.3.2 Discussion
- 2.4 Results
  - 2.4.1 CDM Glass Ceramic
    - (a) Hardened Steel Sphere
    - (b) Tungsten Carbide Sphere
  - 2.4.2 Ceran Glass Ceramic
    - (a) Hardened Steel Sphere
    - (b) Tungsten Carbide Sphere
    - (c) Lead Sphere
  - 2.4.3 Robax Glass Ceramic and Soda-lime Glass
  - 2.4.4 Alumina
    - (a) Hardened Steel
    - (b) Tungsten Carbide
  - 2.4.5 Boron Carbide
    - (a) Hardened Steel
    - (b) Tungsten Carbide
  - 2.4.6 Front Surface Photography
  - 2.4.7 Double Layer Ceramics
  - 2.4.8 Momentum Balance
  - 2.4.9 Glass plus Metal Layer Targets
  - 2.5.0 Front Surface Photography of Impacts on Glass



- 3.1 Fracture modes
- 3.2 Energetics of Impact
  - (a) Alumina
  - (b) Glass Ceramic
- 3.3 The Cone
- 3.4 Variation of Cone Angle with Velocity

## FIGURE CAPTIONS

ACCUSSION FILE	
NHIS CRIM	<input checked="" type="checkbox"/>
DIC TAT	<input checked="" type="checkbox"/>
Unassigned	
JAIL	
TOTAL	
FILED	
CHECKED	
SERIALIZED	
INDEXED	
RECEIVED	
DATE	
TIME	

A-1

## "Investigation of the impact performance of various glass and ceramic systems"

This report describes our research on the impact behaviour of various glass and ceramic systems. The first section describes the liquid impact technique and experiments in which high velocity liquid jets were fired at specimens over a range of velocities and the "post impact" (i.e. "residual") strength measured. The jet technique is a convenient method for applying an intense stress pulse and studying the **dynamic** response of a material. If impact experiments are made over a range of velocities, it is possible to plot "residual" strength versus impact velocity. Such curves give the **threshold** velocity for damage and also show how rapidly the strength decreases for impacts above the threshold condition. Further, if the materials  $K_{IC}$  is known, it is possible to calculate an "equivalent flaw" size. The residual strength curves obtained for the various materials are discussed.

The second section describes a study of the impact behaviour of glass and ceramic materials when impacted by solids. It covers the apparatus for projecting solid spheres, techniques and methods used to measure hardness, fracture toughness, acoustic velocities, and crack velocities, and gives high-speed photographic results of impacts. Projectile materials included steel, lead, and tungsten carbide spheres. The ceramics included various glass and alumina ceramics and boron carbide. In section 3, there is a discussion and analysis of the results, and in section 4 a summary of the main conclusions.

### 1. LIQUID IMPACT TECHNIQUE

#### 1.1 Introduction

The impact of a mass of liquid on a solid target comprises two distinct regimes of behaviour. Consider the impact of a cylindrical mass of liquid of radius  $r$  on a solid surface with velocity  $V$  (fig.1). The liquid initially behaves in a compressible manner until release waves, generated at the circumference of the jet, have reached the jet axis. The pressure,  $P$ , during this stage of the impact is given by

$$P = V \rho_1 c_1 \rho_2 c_2 / \rho_1 c_1 + \rho_2 c_2 \quad (1)$$

where  $\rho_1 c_1$  and  $\rho_2 c_2$  are the densities and shock wave velocities of the liquid and target material respectively. For a cylindrical jet of liquid the duration,  $t$ , of the compressible phase is given by

$$t = r/c \quad (2)$$

The initial high pressure stage is followed by incompressible flow of the liquid. The impact pressure drops to the Bernoulli stagnation pressure,  $P_B$ , given by:

$$P_B = \rho V^2 / 2 \quad (3)$$

The pressure during this second stage of impact is very much lower

(for example, 10% of the initial pressure for  $V = 500 \text{ m s}^{-1}$ ). For this reason most of the impact damage in a brittle material is associated with the initial compressible phase.

### 1.2 The Water Jet Technique

The high velocity water jets are produced by a technique originally developed by Bowden and Brunton (1961) and subsequently modified by Field et al. (1979a and 1979b, 1983). The apparatus is illustrated in fig.2. A lead slug is fired from an air rifle into the rear of a water-filled stainless steel chamber. The forward motion of the sealing neoprene disc extrudes the water at high velocity through the orifice section at the front of the chamber. By careful design of the chamber, water jets with a coherent core of liquid can be produced. High-speed photographs of jets are illustrated in Field et al. (1979b). The system is calibrated so that by varying the firing pressure, a jet of a given velocity can be attained.

### 1.3 Impact Damage in Brittle Materials

Most of the damage in a brittle material is associated with the initial high pressure regime of the impact process. Dynamic loading of the solid during this stage generates compressive, shear, and Rayleigh surface waves (Bowden and Field 1964; Swain and Hagan 1980). Tensile components of the propagating surface wave cause extension of surface defects already present in the material during the loading time of the pulse (typically  $\leq 0.3 \mu\text{s}$ ). The resulting damage consists of an annulus of short circumferential cracks around the impact site (fig.3). The central area of the impact, corresponding approximately to the jet diameter, is undamaged by the compressive loading of the impact process. As the surface wave propagates, it initiates fracture at all the surface defects above a critical size. The short duration of the loading pulse,  $\leq 0.3 \mu\text{s}$ , means that the crack extension is limited. The liquid impact process can, therefore, be used to determine the distribution of surface defects in a material by examination of the impact damage produced.

### 1.4 Impact Damage Assessment for Brittle Materials

Optical examination of the impact damage is important but only provides qualitative information about the failure of the material. The impact damage in brittle materials can be assessed quantitatively by measuring the post-impact or residual strength. Disc specimens of the material are impacted at the centre and the fracture stress measured using a hydraulic bursting technique (Gorham and Rickerby 1975; Matthewson and Field 1980). The apparatus is illustrated schematically in fig.4. A thin disc specimen is supported near its edge by a perfectly flat, hardened tool-steel ring. Hydrostatic pressure is transmitted from the oil to the rear of the specimen by a neoprene gasket. The pressure is increased until failure occurs. From the bursting pressure and position of the fracture origin, the fracture stress of the material can be calculated.

The main advantages of the hydraulic bursting technique compared with other strength measuring methods are:

- 1) Edge failures, which are caused by machining damage, are largely eliminated.
- 2) A large proportion of the specimen surface is tested.
- 3) The stress field is circularly symmetric with radial and tangential stresses of the same order of magnitude. The measured fracture stress is, therefore, virtually independent of the flaw orientation.
- 4) The ease and rapidity of operation.
- 5) The possibility of miniaturization; specimens down to 25 mm can be used.

The measured fracture stress,  $\sigma_f$ , and fracture toughness,  $K_{Ic}$ , can be used to calculate the size of the surface flaw,  $c$ , which caused the failure of the specimen in the strength test. In general, the equivalent flaw size can be calculated from the relation

$$c = \alpha [K_{Ic}/\sigma_f]^2 \quad (4)$$

where  $\alpha$  is a dimensionless constant depending on the flaw and stress field geometry.

Figure 5 shows a plot of fracture strength against impact velocity for soda-lime glass (van der Zwaag and Field 1983). The residual strength curve is typical of a brittle material. A reduction in strength of the material is observed above a critical velocity. Liquid impacts below this threshold velocity do not produce sufficient stress to extend the surface defects. The surface flaw size distribution is not affected, therefore the post-impact strength is comparable to that for the unimpacted material. The threshold velocity is followed by a transition region in which the average fracture stress decays rapidly with increasing impact velocity. Field et al. (1970a) observed a bi-modal distribution of fracture stress in this region. Some specimens are undamaged by the impact, while others fail at a low stress due to extension of surface flaws. The variation in strength is attributed to the statistical nature of the flaw distribution in the specimen surface. A reduction in strength of the specimen will only be observed if there is a large enough surface defect present near the impact site to satisfy the conditions for crack growth. For high impact velocities, the average fracture stress is a much weaker function of impact velocity. All specimens show a loss in strength due to the impact. The increased pulse strength enables many more surface defects to propagate, but the short duration of the pulse limits their extension.

The residual strength curve is slightly modified for multiple jet impacts (van der Zwaag and Field 1983). The cracks are able to grow for each loading cycle of the impact providing the critical stress intensity is exceeded. An increase in the number of impacts therefore results in a decrease in the fracture stress of damaged specimens and a narrower transition region. The threshold velocity for impact damage is independent of the number of impacts. The

accuracy in predicting the threshold velocity can be increased by using a multiple impact technique.

The residual strength technique provides accurate measurement of the threshold velocity for impact damage in brittle materials. The technique can also be used to assess changes in the impact performance of a material.

### 1.5 A Comparison of the Liquid Performance of Various Brittle Materials

The residual strength curves for soda-lime glass, single crystal sapphire, polycrystalline alumina, a hot-pressed silicon nitride and macro-defect-free (MDF) cement (an ICI product) are shown in fig.6. Table 1 gives the threshold velocity for impact damage and the unimpacted fracture strength of these materials along with the fracture toughness, Vickers hardness, and inherent defect size, (that defects of this size were present was confirmed by examination of the fracture origins by scanning electron microscopy).

The single crystal sapphire has the highest fracture strength of the materials tested due to the small inherent flaw size, ca.  $10\text{ }\mu\text{m}$ . The small surface defects contribute to the reasonably high threshold velocity,  $V_T$ , of  $300\text{ m s}^{-1} < V_T < 350\text{ m s}^{-1}$ . Above the threshold, the impact performance of this material is poor due to the low fracture toughness and high crack velocity, i.e. once fracture has initiated, the cracks extend considerably during the loading time of the impact pulse. Field (1962) observed that the maximum fracture velocity in single crystal sapphire is ca.  $4500\text{ m s}^{-1}$ .

The polycrystalline alumina exhibited a low fracture strength,  $146 \pm 8\text{ MPa}$ , which could be improved by a better surface preparation. The threshold velocity for alumina is similar to the value for single crystal sapphire, but the impact performance above the threshold is greatly improved. This can be attributed to the high toughness and low crack velocity of the alumina. Variability in porosity, grain size, and composition of alumina affects the fracture toughness and impact performance (Ferguson and Rice 1971; de With 1984). It is, therefore, important to control these parameters in the material used. In spite of a small inherent flaw size (ca.  $40\text{ }\mu\text{m}$ ), soda-lime glass has a low fracture strength and low threshold velocity due to a low fracture toughness. The MDF cement shows that a very respectable performance can be achieved if the large defects are eliminated. However, as shown later, the materials low hardness restricts its ballistic capabilities.

From the materials tested, the hot-pressed silicon nitride gave the best performance. A high initial strength and a very high threshold velocity were observed. Good impact performance above the threshold for damage arises from the high fracture toughness.

The impacts have been performed with water jets, but the equivalent threshold velocity,  $V'$ , can be estimated for other projectiles from the expression



$$P = V\rho_{\omega}c_{\omega}/(\rho_{\omega}c_{\omega} + \rho_2c_2) = V'\rho_sc_s/(\rho_sc_s + \rho_2c_2) \quad (5)$$

where  $(\rho_{\omega}c_{\omega})$ ,  $(\rho_sc_s)$  and  $(\rho_2c_2)$  are the densities and shock wave velocities for water, the other projectile materials (for example, steel) and the target material respectively. For the impact of a mild steel cylindrical projectile, the equivalent threshold velocities are given in Table 1. Equation (5) holds reasonably well if the pulse durations are of similar magnitude.

Hot-pressed silicon nitride has the highest predicted threshold velocity for impact damage by a mild steel projectile. The high hardness of this material will also contribute to give an excellent impact performance. The threshold velocity for alumina and sapphire are similar. Alumina will have the better performance due to its high toughness and low crack velocity. These calculations indicate that soda-lime glass will have the lowest threshold velocity for impact damage initiation by a mild steel solid particle. This results from the low fracture toughness and low modulus.

## 1.6 Conclusions

For the range of brittle materials included in this investigation, the jet technique and hydraulic strength test provide quantitative information on the threshold for damage, the size of the inherent defects and crack propagation during the loading pulse of the impact. The form of the residual strength curve can be related to the defects, the fracture toughness and crack velocity of the material. From the threshold velocity measurements the onset of impact damage by a solid particle can be predicted, thus providing a method of quantitatively ordering the materials with respect to damage initiation.

## 2. SOLID PARTICLE IMPACT

### 2.1 Introduction

The impact behaviour of various glass and ceramic materials has been investigated. The impacts were performed with hardened steel, tungsten carbide, and lead spheres on tile specimens of the materials at velocities in the range  $30 \text{ m s}^{-1}$  to  $1000 \text{ m s}^{-1}$ . These controlled impacts were photographed at microsecond framing intervals with an image converter camera (Imacon). A momentum balance was designed during the project and this allowed the momentum of the projectile (if it penetrated) and any target debris to be measured. Fracture patterns of the impacted specimens and the damage to the projectiles were recorded for each impact experiment. Results from these experiments have identified the various failure modes of the material during the impact process.

In addition to the impact experiments a number of the mechanical properties of the materials under investigation have been measured. These properties include hardness, fracture toughness, longitudinal and shear wave velocities, bulk, shear and Young's moduli, and density and maximum crack velocity. These

various techniques were fully discussed in the last Annual Report (Townsend and Field, 1987) and only brief reference will be made here.

## 2.2 Apparatus

A small bore, single stage gas gun was used to accelerate the projectiles (fig.7). It consists of a cold drawn steel barrel, length 2 m and internal diameter 13.3 mm, connected by means of a breech to a pressure reservoir. The projectile, typically a hardened steel sphere 3 mm to 6 mm diameter, is mounted on the front face of a cylindrical, polyethylene sabot, length 25 mm. On firing, the sabot is accelerated down the barrel and then stopped by the muzzle block allowing the projectile to continue unimpeded. Reproducible impact velocities are obtained by using a double-diaphragm bursting technique (Hutchings and Winter, 1975). For a firing pressure  $P$ , diaphragms of a suitable material (e.g. copper foil) are chosen with a bursting pressure between  $P/2$  and  $P$ . The diaphragms are inserted into the breech as shown in fig.12. The reservoir and inter-diaphragm space are pressurised to  $P/2$  and then section B is isolated. Gas pressure in the reservoir is increased to  $P$ . Firing is achieved by venting the inter-diaphragm space to atmosphere. The pressure across the first diaphragm rises to  $P$  and it subsequently ruptures. Failure of the second diaphragm then occurs allowing the unimpeded gas flow to drive the sabot down the barrel. Using this technique, with gas pressures up to 4 MPa, projectile velocities in the range  $250 \text{ m s}^{-1}$  to  $1000 \text{ m s}^{-1}$  can be achieved with an accuracy of  $\pm 5\%$ . For lower velocities, the breech mechanism is replaced by a fast-acting solenoid valve. The range of velocities in this case is  $30 \text{ m s}^{-1}$  to  $400 \text{ m s}^{-1} \pm 3\%$ . The propellant gas can be either nitrogen or helium. Higher velocities are attained with helium due to its high acoustic wave velocity and low molecular weight (Seigel, 1965). Reducing the mass of the sabot by hollowing out the centre portion produces an increase in velocity of approximately 20%.

The impact velocity is determined from the time for the projectile to travel a measured distance in free flight. Two parallel light beams intersecting the path of the projectile define this distance (fig.8). The flash unit and image converter camera are triggered from the interruption of the second light beam. The triggering pulse is delayed to allow time for the projectile to reach the target before the camera and flash are activated. By placing the target close to the second light beam,  $< 20 \text{ mm}$ , small variations in velocity have a negligible effect on the delay time. With this experimental arrangement, more than 90% of the impact events are successfully recorded. For experiments involving a long flight path, a more complicated method for determining the delay time is necessary to ensure the same high success rate. In this case, the time of flight between the two beams is electronically processed while the projectile is in motion to give the delay time prior to impact (Pope, 1985). Care must be taken in both cases to ensure that the light level has reached full intensity before the camera is activated.

The specimen is supported along the upper and lower edges by

two metal plates lined with neoprene rubber (fig.8). This method of support minimises the energy transmitted across the boundaries of the specimen by stress wave interaction.

The position of the camera and flash unit can be varied to record different views of the impact process under various lighting conditions.

### 2.3 Materials Description

The materials investigated in this report comprised various polycrystalline alumina, boron carbide, glass ceramics (CDM, Ceran and Robax), and soda-lime glass (see Tables 2 and 3). All the materials were in the form of tile specimens typically, 50 mm x 50 mm, with thickness in the range 3 mm to 20 mm. For each specimen, the impact was made at the centre of the square face.

A series of experiments were performed in order to determine the mechanical properties of the materials. The techniques used are summarised in Table 4. Details of low hardnesses, toughnesses and stress wave velocities were measured and are given in Townsend and Field (1987) and will not be repeated here.

#### 2.3.1 Crack Velocity

Crack velocity is an important parameter in the study of the failure of brittle materials. High-speed photography can be employed to monitor crack growth in transparent materials and several examples of crack propagation in soda-lime glass and Robax are presented later. For opaque or transparent materials alternative techniques must be employed. Kerkhof and his co-workers (see reviews by Schardin 1959; Field 1971) developed an elegant technique for studying crack propagation. This technique involves sending a beam of distortional (transverse) ultrasonic waves down through a specimen at the time of fracture. The oscillating tension, when superimposed on the main tension opening up the crack, modulates the growing fracture causing permanent "ripple" markings on the fracture face. The frequency of the imposed wave is accurately measured; therefore, the spacing of the ripple markings gives a measure of the crack velocity to high precision.

Figure 9a shows the experimental configuration employed here for measuring crack velocity. A notched specimen is loaded in tension. A quartz shear transducer, bonded to the edge of the specimen is driven at a frequency of  $5 \times 10^6$  Hz from a 500 W power supply. In order to ensure that the maximum shear wave amplitude is attained within the specimen, a lead zirconate titanate shear transducer is bonded to the lower edge of the specimen. The driving frequency is adjusted until the maximum output is observed on this second transducer. Careful electrical screening of each component is necessary to avoid spurious signal pick-up from the driving circuit. The ultrasonic shear stress waves are maintained during loading of the specimen until failure occurs. Figures 9b and c show examples of the ripples. As is clear from the figure, a precise and permanent record of the whole fracture process is obtained with this technique. The ripples are only of micron

height and the ultrasonics has no significant effect in reducing the fracture velocity. By measuring the spacing of the ripples prior to the onset of roughening of the fracture surface and subsequent crack branching, the maximum crack velocity in the material can be determined. These crack velocities are:

Material	Maximum Crack Velocity
Soda-lime glass	$1550 \pm 50 \text{ m s}^{-1}$
Ceran	$2200 \pm 50 \text{ m s}^{-1}$
Robax	$2300 \pm 50 \text{ m s}^{-1}$

The value observed for soda-lime glass is in good agreement with the values obtained by Field (1971),  $1580 \text{ m s}^{-1}$ , and Chaudhri et al. (1976),  $1400\text{--}1500 \text{ m s}^{-1}$ . Further, the crack velocity for Robax and soda-lime glass corresponds exactly with the velocities determined by high-speed photography.

Attempts to measure the crack velocity in alumina, boron carbide, and CDM glass ceramic were unsuccessful. This is due to the relatively rough fracture surface of these materials which obscures the ripple pattern. Typically the ripple pattern is only of micron dimensions. Other techniques are being investigated for determining the crack velocity in these materials.

### 2.3.2 Discussion

The materials investigated fall into two distinct groups:

- (a) Glass ceramics and glasses with low elastic moduli and stress wave values i.e.  $E < 100 \text{ GPa}$  and  $C_1 < 6500 \text{ m s}^{-1}$ .
- (b) Alumina and boron carbide with high moduli and stress wave values i.e.  $E > 250 \text{ GPa}$  and  $C_1 > 8500 \text{ m s}^{-1}$ .

Group (b) materials also have higher hardnesses and fracture toughnesses than the group (a) materials.

The measured stress wave velocities and elastic constants for soda-lime glass are in good agreement with literature values (see e.g. Kaye and Laby 1973). Ceran, Robax, and CDM glass ceramic exhibit slightly higher stress wave velocities and elastic moduli than soda-lime glass. Further information concerning the composition and structure is needed to explain these differences in the elastic properties of the materials.

Shear modulus measurements on Ceran are in good agreement with the value of  $37 \text{ GPa}$  from Schott Glass (1984). Ridges on the surface of the Ceran specimens prohibited longitudinal stress wave velocity measurements. Values of  $E$  and  $\nu$  for this material were obtained from Schott Glass (1984) and the stress wave velocity calculated from the elastic constants.

The series of alumina specimens investigated show an increase

in Young's modulus as the density of the material increases. This observation is in accord with the relationship between porosity and modulus for ceramics (for reviews see Rice 1977; Dorre and Hubner 1984). The values of the elastic constants for the various types of alumina correspond closely with previously reported results (Lynch 1975; Morrell 1985).

In general the presence of a second phase in a ceramic system also produces a reduction in the elastic moduli. The high moduli of the zirconia toughened alumina are, therefore, attributable to the very low porosity of these specimens.

Boron carbide exhibits high stress wave velocities and correspondingly high elastic moduli. These values of moduli are, however, low compared to data quoted by Morrell (1985) indicating that impurities may be present in the material. Difficulties in measuring the high stress wave velocity in this material may also account for the discrepancy.

## 2.4 Results

### 2.4.1 CDM Glass Ceramic

The impact experiments were performed with a 5 mm diameter hardened steel and tungsten carbide sphere at velocities in the range  $40 \text{ m s}^{-1}$  to  $900 \text{ m s}^{-1}$ . The limited number of specimens available prevented the impact of lead balls to be studied; however, a description of the impact of lead on a glass ceramic, Ceran, is given in the following section (2.4.2).

#### (a) Hardened Steel Sphere

Fig.10 shows an example of a glass ceramic specimen after impact at  $240 \text{ m s}^{-1}$ . A schematic representation of the crack systems and the deformed zone is given in fig.11. Impact velocities of ca.  $40 \text{ m s}^{-1}$  generated a Hertzian-type ring crack on the surface of the specimen and a short cone crack in the material. Above  $55 \text{ m s}^{-1}$ , the cone cracks propagate to the rear of a 10 mm thick glass ceramic specimen resulting in the expulsion of a cone of material. As the velocity of impact increases, the semi-apex angle of the cone crack produced **decreases** (Fig. 13). A detailed discussion of the formation of the cone cracks and the variation of the semi-apex angle,  $\theta$ , with impact velocity will be given later, when data from other materials have been presented.

The lateral crack system in the glass ceramic is evident at impact velocities greater than  $80 \text{ m s}^{-1}$ . Increasing the velocity of the impact increases the extent of the suitable defects at the elastic/plastic boundary of the deformed zone (Hagan and Swain 1978). These cracks propagate under the action of the residual stresses caused by the mismatch at the boundary between the irreversible deformed material and the surrounding elastic matrix. They propagate in a saucer-like shape towards the surface of the material (fig.11). At high impact velocities ( $> 200 \text{ m s}^{-1}$ ), the lateral cracks reach the surface of the glass ceramic specimen causing removal of material and thereby producing a "double cone" feature at the impact site. Higher impact velocities result in the removal of more material from the impact face by lateral crack

growth. Traces where the lateral cracks reached the surface can be seen on the impact face of the specimen shown in fig.10.

Failure of the rear surface of an impacted glass ceramic specimen is caused by spalling combined with propagation of the cone crack and radial crack system. The impact of the sphere on the target produces a compression wave in the material. Reflection of this wave at the rear surface of the specimen produces a tensile stress wave. At a sufficient stress level, the reflected tensile stress wave can initiate spall failure close to the rear face of the specimen (see, for example, Johnson 1972). Spall failure is evident in the glass ceramic at velocities above ca.  $120 \text{ m s}^{-1}$ .

Radial cracks are caused by bending of the specimen during the impact loading and result in fragmentation of the tile. Impact velocities greater than  $60 \text{ m s}^{-1}$  cause radial cracking of the tile specimens. The number of radial cracks increases as the velocity of the impact increases due to the higher loads generated by the impact. In general the expelled cone of material, caused by the cone cracks reaching the rear surface of the specimen, contains radial fractures. These fractures align with the radial fractures in the specimen, thus indicating that the radial cracks initiate from the rear surface of the specimen before the cone cracks have extended through the thickness of the tile (fig.12).

For sufficiently high impact velocities, a second cone crack may form. This second cone failure initiates at a larger contact radius than the first cone and is consequently much shallower i.e. larger semi-apex angle. Woodward and Field (1974) have observed that for steel ball impacts on glass the second ring crack initiates before the first ring crack, from which the first cone crack propagates has been completed. Secondary cone cracks are observed in the glass ceramic for impact velocities above ca.  $300 \text{ m s}^{-1}$ . In general, measurements of the semi-apex angle of the secondary cone are difficult; however, a trend of decreasing cone angle with increasing impact velocity was observed. For very high impact velocities,  $> 600 \text{ m s}^{-1}$ , multiple cone cracks of progressively shallower angles (i.e. greater  $\theta$  values) are observed.

Penetration of the 9.8 mm thick glass ceramic specimen by the projectile was achieved for impact velocities greater than  $450 \text{ m s}^{-1}$ . The mechanism and criterion for penetration is not clear at the present time. For penetration to occur, the loading time of the impact must be longer than the time for the cone crack to propagate through the specimen and secondly, the residual energy of the projectile must be capable of overcoming the frictional drag caused by abrasion with the crushed glass ceramic.

The hardened steel sphere, on impact with the glass ceramic, suffers a small degree of plastic deformation. It should be noted that the steel sphere is slightly harder than the glass ceramic. High-speed Imacon sequences (fig.14) of the impact show that a plume of fine high velocity particles, p, is produced from the contact area. This jetting of material results from deformation and crushing of the material beneath the sphere during impact.

Scanning electron micrographs of the projectile (fig.15) after impact show areas, e, where the high velocity jetting material has eroded the projectile surface. Around this area is a region, g, in which the fine glass particles have remained embedded in the hardened steel sphere.

The central region of the projectile, u, is relatively undamaged. It is proposed that this central undamaged region corresponds to the initial contact area in which the contact velocity between the sphere and the target is greater than the velocity with which the crushed zone propagates through the material (fig.16). In this regime the fine particles generated in the crushed zone are essentially trapped beneath the sphere. As the contact velocity falls below the propagation velocity of the crushed zone, these particles can escape and form the jetting material shown in fig.14. High-speed photography of the formation of the crushed zone in transparent materials (figs.17 and 18) show that initially the crushed zone propagates at a velocity close to the terminal crack velocity in the material.

#### (b) Tungsten Carbide Sphere

A limited number of impacts were performed on the CDM glass ceramic with 5 mm diameter tungsten carbide spheres. Impact velocities of ca.  $100 \text{ m s}^{-1}$  produced extensive failure of the tile specimen. Cone cracks were observed together with extensive lateral cracking. Several radial cracks were formed, resulting in break-up of the specimen. Spall failure was also observed from the rear face of the specimen. A high-speed photographic sequence of the impact event shows that the projectile rebounds from the surface of the specimen. The projectile appears to be undamaged by the impact. Further, the sequence shows that a plume of fine high velocity material is produced from the contact area. Increasing the impact velocity produced progressively more damage to the tile specimen. This increase in damage comprised of formation of multiple cone cracks, a greater number of radial failures and an increase in material loss by lateral cracking, spalling and jetting of fine high velocity material from the impact site. As in the case of the hardened steel sphere impacts, the angle of the first cone crack **decreases** as the impact velocity increases. For impact velocities greater than  $400 \text{ m s}^{-1}$  the tungsten carbide projectile passed through the CDM specimen (this compares with ca.  $450 \text{ m s}^{-1}$  for the steel projectiles). In this series of experiments, the tungsten carbide sphere was not damaged by the impact.

The damage produced by the tungsten carbide projectile in the CDM glass ceramic was qualitatively greater than that produced by a hardened steel ball with the same velocity. This increase in damage is attributed to the higher impact pressures produced by the tungsten carbide projectile due to the higher density and shock wave velocity of this material compared to that of hardened steel.

An estimate of the impact pressure,  $P$ , during the initial stages of the impact can be made from equation (1). It should be noted that equation (1) is derived from considering the normal impact of cylindrical rods; however, it can be applied to a first

approximation to estimate the impact pressure on the central axis for the case considered here. By evaluating equation (1) for hardened steel and tungsten carbide impacts on CDM it is found that:

$$P_{\text{tungsten carbide}} = 1.14 P_{\text{hardened steel}} \quad (6)$$

Clearly, a more complex model and theory are required to describe the impact process fully; however, this simple equation illustrates the increase in impact pressure produced by using tungsten carbide projectiles which corresponds to the observed enhanced specimen damage and lower penetration velocity. The ratio of the penetration velocities for steel and tungsten carbide projectiles is 1.13 (i.e. 450/400) which is close to that predicted by equation (6).

#### 2.4.2 Ceran Glass Ceramic

A series of impacts performed with hardened steel, tungsten carbide and lead spheres at velocities up to  $900 \text{ m s}^{-1}$  on tile specimens (50 mm x 50 mm x 10 mm) of ceran glass ceramic. This glass ceramic, which was red in colour, had a slightly higher Young's modulus and density, but lower hardness and toughness than the other glass ceramics (see Tables 2 and 3). The damage modes occurred at lower velocities than with the CDM glass ceramics.

##### (a) Hardened Steel Sphere

The response of Ceran to an impact by a 5 mm diameter hardened steel sphere is similar to that observed for the CDM glass ceramic. Fig.11 shows schematically the crack systems produced in Ceran by the impact. Projectile impacts of approximately  $20 \text{ m s}^{-1}$  generated a Hertzian type ring crack on the surface of the specimen and a short cone crack in the material. Above  $40 \text{ m s}^{-1}$  the cone crack propagates to the rear of 10 mm thick specimens, resulting in the expulsion of a cone of material. The corresponding velocity for 8 mm thick specimens is  $32 \text{ m s}^{-1}$ . The onset of lateral cracking and secondary cone crack formation in Ceran is observed for impact velocities greater than  $80 \text{ m s}^{-1}$ . Further, radial cracks are formed in the specimen at this velocity, resulting in break-up of the specimen. The radial cracks arise from bending of the specimen during the impact loading and initiate from the rear surface of the specimen (fig.12). Impact velocities in excess of  $100 \text{ m s}^{-1}$  generate sufficient stress within the specimen to cause spall failure of the rear face. At  $150 \text{ m s}^{-1}$  high-speed jetting of fine material from the impact site is observed. The onset of this phenomenon coincides with removal of material from the impact face by lateral crack propagation. Increasing the impact velocity produces correspondingly more damage in the target specimen. The semi-apex angle of the first cone crack produced in the specimen was found to decrease from a static value of  $69 \pm 3^\circ$  as the impact velocity increases. See figs. 19 and 20; a fuller discussion of these data are given later. Penetration of the 10 mm thick Ceran specimen by a hardened steel sphere was observed for impact velocities greater than  $300 \text{ m s}^{-1}$ . The hardened steel sphere suffers very little damage even at impact velocities in excess of  $800 \text{ m s}^{-1}$ . A small degree of plastic deformation is observed, along with the embedment of fine glass ceramic particles caused by



the high-speed jetting. Views of 8 mm thick samples after impact are shown in fig. 21.

#### (b) Tungsten Carbide Sphere

The impact damage produced by a tungsten carbide sphere in the ceran glass ceramic is similar to that produced by a hardened steel sphere. The principal difference is that for a given impact velocity the damage produced by tungsten carbide is qualitatively greater than that arising from the hardened steel impact. For example a  $30 \text{ m s}^{-1}$  tungsten carbide impact causes the cone crack to propagate to the rear of a 10 mm thick specimen. This compares with an impact of  $40 \text{ m s}^{-1}$  with hardened steel to produce the same damage. Tungsten carbide sphere impacts with a velocity greater than  $100 \text{ m s}^{-1}$  produce multiple cone cracking, lateral cracks, radial failure of the specimen, a plume of high velocity particles from the contact area, and spall failure. As in previous cases, the extent of this damage increased as the impact velocity increased. At velocities greater than  $270 \text{ m s}^{-1}$  the tungsten carbide projectile penetrates the Ceran (10 mm thick) specimen. For the range of impact velocities studied, the tungsten carbide projectile appeared to be undamaged by the impact.

The increase in damage produced by the tungsten carbide projectile is attributed to the higher impact pressures generated. From equation (6) the relation between the initial impact pressures for tungsten carbide and hardened steel on Ceran at the same impact velocity is:

$$P_{\text{tungsten carbide}} = 1.15 P_{\text{hardened steel}}$$

The higher impact pressure produced by tungsten carbide accounts for the enhanced specimen damage. The above ratio predicts the lower threshold velocities found with tungsten carbide reasonably well. For example, the ratio of velocities steel/tungsten carbide are for the ejection of a cone crack (1.33), and penetration (1.11).

#### (c) Lead Sphere

A series of impact experiments were performed with lead spheres of nominal diameter 5 mm. Projectile velocities below  $100 \text{ m s}^{-1}$  produced no observable damage in the Ceran specimen. The lead sphere, however, suffered severe plastic deformation resulting in the formation of a flat. Impact velocities above  $100 \text{ m s}^{-1}$  gave rise to cone cracks in the specimen. At  $180 \text{ m s}^{-1}$ , the cone cracks propagate to the rear of the specimen resulting in the expulsion of a cone of material, and there is significant radial cracking. Extensive plastic flow of the projectile and some penetration of projectile material was observed at this velocity. Impact velocities in excess of  $200 \text{ m s}^{-1}$  did not result in lateral crack formation. Clearly the impact pressure is not sufficient to generate the residual stresses below the contact area which are necessary for lateral crack growth. Further impacts need to be performed at higher velocity to establish whether lateral cracks

can be formed in this system.

For the same impact velocity, the damage produced by the lead sphere is considerably less than a hardened steel or tungsten carbide projectile. From equation (6) the relation between the initial impact pressures is:

$$P_{\text{lead}} = 0.78 P_{\text{hardened steel}}$$

The lower impact pressures produced by lead projectiles accounts to some extent for the reduction in specimen damage. A more comprehensive model must be employed, however, to describe the incompressible flow which follows the initial compressible behaviour stage. The lead impact is probably best modelled by analyses developed for liquid impact (Bowden and Field 1964).

#### 2.4.3 Robax Glass Ceramic and Soda-lime Glass

A small number of the optically transparent Robax glass ceramic specimens were available. In order to take full advantage of these specimens, high-speed photography was used to observe crack formation in the material resulting from high velocity impact. Examples of the high-speed sequences obtained for Robax and soda-lime glass are shown in figs.17 and 18.

The impact velocity of the steel ball is  $250 \text{ m s}^{-1}$ . The crack velocity was estimated from the propagation of the cracks, c. These were chosen because they appear to be singly developing cracks, rather than fracture paths made up from multiply-nucleated cracks. The cracks are clearly near their limiting (maximum) velocity since there is evidence of crack branching. For Robax the maximum crack velocity is  $2300 \pm 100 \text{ m s}^{-1}$  and for soda-lime glass,  $1480 \pm 50 \text{ m s}^{-1}$ . These values are in excellent agreement with those obtained with the ultrasonic technique (section 2.3.1). The value observed for soda-lime glass is in good agreement with the values obtained by Field (1971),  $1580 \text{ m s}^{-1}$ , and Chaudhri et al. (1976),  $1400\text{-}1500 \text{ m s}^{-1}$ .

Surface defects in the material, r, are extended by the Rayleigh surface wave generated by the impact (Bowden and Field 1964). For this impact configuration, reflection of the loading pulse from the rear surface of the specimen (i.e. right-hand side of picture) did not significantly influence the crack propagation, though a small effect on the crack paths can be detected.

High-speed sequences,  $0.95 \mu\text{s}$  interframe time, of the impact process on thinner specimens are shown in fig.18. Fig.18(a) shows a 3 mm diameter hardened steel sphere impact on a glass ceramic. Reflection of the compressive loading pulse as a tensile stress wave at the rear surface of the specimen causes the surface cracks, s. Lateral cracks, l, develop in frames 10-14 and reach the surface, resulting in the eventual removal of material from the impact face of the specimen. Similar crack patterns are observed in the soda-lime glass specimen shown in fig.18(b).

The propagation velocity of the crushed zone beneath the

impact site can be estimated from these high-speed sequences. The crushed zone propagates at approximately  $1500 \text{ m s}^{-1}$  and  $2200 \text{ m s}^{-1}$  for soda-lime glass and the Robax glass ceramic respectively. These velocities are equal to the terminal crack velocity in these materials.

#### 2.4.4 Alumina

A number of alumina specimens were supplied with different composition and sample thickness. In general, the impact response of all these materials was similar. The following description of the impact behaviour is, principally, based upon observation of Sintox alumina but can be applied to the other alumina compositions.

##### (a) Hardened Steel

Impacts were performed on 2"x 2" tile specimens, thickness 6-11 mm, of alumina. High-speed Imacon sequences of the impact of a 5 mm diameter hardened steel sphere on alumina are shown in fig.22. For impact velocities up to approximately  $200 \text{ m s}^{-1}$ , the sphere rebounds from the surface of the material. (Occasionally, fig. 34a is an example, rebound occurred at higher velocities.) High impact pressures generated, due to the high hardness of the alumina, result in extensive plastic deformation of the projectile and formation of a flat, F. As the impact velocity is increased, fracture of the projectile occurs. Fig.23 shows a scanning electron micrograph of a hardened steel sphere after impact at  $200 \text{ m s}^{-1}$  on an alumina specimen. The cracks, C, are clearly visible along with the flat, F, caused by plastic deformation on impact. Increasing the velocity of impact produced more extensive deformation and fragmentation of the steel sphere. A schematic representation of the failure observed in the projectile is shown in fig.24. An "inverted cone", n, is formed in the projectile, the base area of this cone corresponding to the initial contact area between the sphere and the specimen. For sufficiently high impact loads, fracture planes, r, form in the sphere resulting in fragmentation. Scanning electron micrographs of the sphere fragments are shown in fig.25. This figure shows the flat formed, f, the fracture plane in the sphere, c, the flow lines, l, caused by extensive deformation of the material, and the cone of material, n, produced from the contact area. At sufficiently high impact velocities ( $> 400 \text{ m s}^{-1}$ ) the fragments of the projectile flow radially outwards across the surface of the tile producing a metallic deposit on the specimen. Fig.26 shows a hardened steel ball after impact at  $460 \text{ m s}^{-1}$  on an alumina specimen. The sphere has undergone extensive plastic deformation and the base of the "inverted cone" formed at the contact area, n, is shown along with the radial flow of material, q. At progressively higher impact velocities, the extent of deformation and fracture in the projectile increases. For all impact velocities, however, a cone of material formed during the initial contact is observed. Similar failure features have been observed for the fracture of brittle spheres on impact (Arbiter et al. 1969; Tilly and Sage 1970).

The impact of a hardened steel sphere on an alumina tile specimen produces a Hertzian-type cone failure over the range of

impact velocities investigated ( $50\text{--}1000\text{ m s}^{-1}$ ). For impact velocities greater than ca.  $200\text{ m s}^{-1}$  the cone crack propagates through the thickness of the specimen resulting in a cone of material as shown in figs. 27, 28, 29 and 49. The cone of material consists of an upper smooth area and a lower roughened region. This roughened region is caused by the interaction of the propagating cone crack with the reflected tensile wave from the rear face of the specimen. In fig. 28 the cone has fractured along the initial line of interaction. The reflected tensile wave also produces a change in the cone angle during the later stages of cone crack propagation. Fig. 30 is a schematic representation of the cone crack formed in the alumina by the impact. The initial point of contact is represented by  $p$  and the image source of the reflected tensile pulse by the point  $p'$ . The point of interaction between the reflected tensile wave and the cone crack is shown at the position  $Y$ . Before the interaction, the tensile stress at the crack tip will be normal to the growing fracture, i.e.,  $a a'$ . The tensile wave will effectively superimpose a stress  $b b'$  to give a resultant  $R R'$ , which will cause the cone crack to change direction because tensile fracture propagates normal to the maximum tension at the crack tip. At sufficiently high impact velocities,  $> 500\text{ m s}^{-1}$ , radial failure is observed in the cone of material following the radial crack trajectories present in the tile specimen.

The quasi-static semi-apex cone angle for indentation of alumina with a 5 mm diameter hardened steel sphere for a 5000 N indent was  $64^\circ \pm 3^\circ$ . Measurements for a range of impact velocities are given in figs. 19 and 20. The values are all **less** than the static value. The mechanism for this is discussed later (section 3.6). However, the trend with increasing velocity is a small but definite **increase** in angle rather than the decrease found with the glass ceramic!

High-speed Imacon sequences of the impact of a hardened steel sphere on an alumina specimen (figs. 22 and 31a) show that the high velocity plume of fine particles, evident with the glass ceramic, is not present. This indicates that the extent of deformation and/or crushing in the alumina is small. The alumina is harder than the steel projectile (Table 2). In addition, lateral cracks are not observed in the alumina. The lateral crack system propagates under the action of residual stresses, caused by permanent deformation in the material, during the unloading cycle. Deformation of alumina during impact is minimal; consequently, the residual stresses are not sufficient to nucleate and propagate the lateral crack system.

#### (b) Tungsten Carbide

Tungsten carbide sphere impacts were performed on the sintox alumina at impact velocities up to  $750\text{ m s}^{-1}$ . At low impact velocities,  $\sim 50\text{ m s}^{-1}$ , radial cracks are evident in the tile specimens. A ring crack was observed at the impact site, but the cone crack had not developed. The impact had caused compaction of the alumina in the contact area. There was also evidence of small lateral cracks propagating from the bottom of this deformed zone. The tungsten carbide projectile appeared to be undamaged by the

impact.

Increasing the impact velocity resulted in extensive damage to the projectile. For an impact velocity of  $\sim 80 \text{ m s}^{-1}$ , brittle failure of the projectile occurred producing two pieces of approximately equal size. The fracture plane in the projectile was normal to the impact face of the specimen. It is thought that this failure initiated from the rear of the projectile by the action of a reflected tensile wave. A compacted zone beneath the projectile contact area and small lateral cracks causing removal of material from the impact face were observed in the tile specimen at this impact velocity. Short cone cracks which did not reach the rear surface of the specimen were evident. Lateral crack formation made measurement of the cone angle and initiation point difficult. Values of the cone angle are given in Table 4. Essentially the same damage was observed in the tile specimen for impact velocities up to approximately  $120 \text{ m s}^{-1}$ . Extensive brittle failure of the projectile was observed at these impact velocities.

Further increase in the impact velocity resulted in more damage to the specimen and projectile. The number of radial cracks in the tile increased with increasing impact velocity. At  $\sim 175 \text{ m s}^{-1}$  the cone cracks propagated through the thickness of the specimen (8.6 mm). Radial fractures were observed in the cone cracked area of material which coincide with those in the remainder of the specimen. This indicates that the radial failure initiates before the cone cracks reach the rear surface of the specimen (see fig.12).

Impact velocities above  $200 \text{ m s}^{-1}$  generate a reflected tensile wave from the rear surface which, when combined with the stress associated with the propagating cone crack, produces a resultant stress which is of sufficient intensity to cause fracture of the cone along a line parallel to the impact face. As described previously the interaction of the reflected wave with the propagating cone crack also causes an increase in the cone angle (fig.30). At impact velocities greater than  $300 \text{ m s}^{-1}$ , the reflected tensile wave causes spall failure from near the rear surface of the specimen. In addition, secondary cone cracks, with large cone angles, were observed for this velocity range.

Examination of the specimens after impact indicates that significant compaction of the alumina occurs at the impact site. At high impact velocities,  $> 400 \text{ m s}^{-1}$ , high-speed photographic sequences indicate that some of this crushed material is expelled as a high velocity plume of fine particles. As the impact velocity increases the damage to the tile increases. This extensive damage comprises of multiple cone cracking, a large number of radial cracks, plus removal of the target material by lateral cracking, spall failure, and jetting from the contact area.

Impact velocities up to  $\sim 50 \text{ m s}^{-1}$  produced no significant damage to the projectile. Brittle failure of the projectile was observed for all impact velocities greater than  $\sim 80 \text{ m s}^{-1}$ . Qualitative examination of the projectile fragments after impact

indicates that as the impact velocity increases the extent of failure in the projectile increases. There is very little evidence for plastic deformation occurring in the projectile during the impact process. Metallic deposits from the projectile were observed on the impact face of the tile at velocities greater than  $\sim 200 \text{ m s}^{-1}$ . For the range of impact velocities investigated,  $< 750 \text{ m s}^{-1}$ , penetration of the tile specimen by the tungsten carbide projectile was not observed. Small fragments produced by break-up of the projectile are unable to penetrate the specimen. Further this break-up of the projectile effectively distributes the impact energy over a large area of the specimen.

Cone crack failure was evident in all the alumina specimens impacted at a velocity greater than  $80 \text{ m s}^{-1}$ . The measured semi-apex cone angles for various impact velocities are presented in table 4. The spread in cone angle values is partly due to asymmetry of the cone crack. In addition, extensive damage in the contact area prevents accurate measurement of the cone angle.

The results presented in Table 5 indicate that there is a trend of decreasing semi-apex cone angle with increasing impact velocity for tungsten carbide sphere impacts on alumina. This variation in cone angle with impact velocity is interestingly enough similar to the results obtained for CDM glass ceramic and Ceran. For further discussion see section 3.6.

The tungsten carbide projectile produces significantly more damage than a hardened steel sphere with the same impact velocity. As discussed in previous examples, this increase in damage can be partly attributed to the increase in impact pressure. From equation (1) it can be shown that:

$$P_{\text{tungsten carbide}} = 1.26 P_{\text{hardened steel}}$$

It is evident that the impact pressure alone is not sufficient to characterise the response of the target and projectile. At modest impact velocities,  $\sim 400 \text{ m s}^{-1}$ , lateral cracks and jetting are produced in alumina by a tungsten carbide projectile. These failure modes could not be produced by a hardened steel sphere impact at high velocity,  $\sim 900 \text{ m s}^{-1}$ . Further, high velocity impact of lead projectiles produced very little damage in the alumina specimen but extensive plastic flow of the projectile. Clearly, the hardness or yield stress of the materials must be taken into account when describing the behaviour of the system as this will determine the maximum impact load.

#### 2.4.5 Boron Carbide

##### (a) Hardened Steel

A series of hardened steel sphere impacts were performed on boron carbide tile specimens ( $50 \text{ mm} \times 50 \text{ mm} \times 6.7 \text{ mm}$ ) at velocities in the range  $120 \text{ m s}^{-1}$  to  $850 \text{ m s}^{-1}$ . At an impact velocity of  $120 \text{ m s}^{-1}$ , plate bending due to the impact load generated six radial cracks in the specimen. Primary and secondary cone cracks are evident at this impact velocity. These cone cracks propagate

through the specimen, resulting in the expulsion of a cone of material. In general the cone of material contains radial fractures which coincide with those in the tile specimen. At this impact velocity the reflected tensile wave from the rear surface of the specimen appears to have little influence on the propagation of the cone crack. There is no evidence of compaction, lateral cracking, or spall failure in the boron carbide material. High impact pressures generated, due to the high hardness of the boron carbide, result in plastic deformation of the projectile and formation of a flat on the sphere. The degree of plastic deformation produced in the hardened steel by an impact at  $120 \text{ m s}^{-1}$  on boron carbide is approximately equivalent to that produced by a  $180 \text{ m s}^{-1}$  on alumina.

Increasing the impact velocity produced essentially the same failure modes in the specimen. Fig.32 shows a boron carbide specimen after impact at  $255 \text{ m s}^{-1}$ . Extensive radial failure of the specimen is observed. The cross section of the specimen shows the traces of the second cone crack, semi-apex angle  $\sim 60^\circ$ . Fragments from the tile specimen indicate that the first cone which formed inside the secondary cone had a semi-apex angle of  $\sim 39^\circ$ . High-speed Imacon sequences of the impact event (see fig.31b) shows the projectile suffers extensive fracture and deformation on impact. Fracture in the projectile initiates from the surface furthest from the impact face and is caused by a reflected tensile wave.

As the impact velocity was increased the extent of damage to the specimen increased; however, the modes of failure remained the same. There was no evidence of compaction, lateral cracking, or jetting of fine material up to velocities in excess of  $800 \text{ m s}^{-1}$ . At these velocities the tile was damaged to such an extent that it was not possible to establish whether spalling occurred. Impact velocities up to  $\sim 400 \text{ m s}^{-1}$ , however, did not produce spall failure. The impact pressure generated is limited by the hardness or yield stress of the hardened steel projectile. This was not sufficient to cause compaction of the boron carbide; consequently jetting did not occur and further, there are no residual stresses generated on unloading to propagate the lateral crack system.

Primary and secondary cone angles for various impact velocities are presented in Table 6. Above  $\sim 350 \text{ m s}^{-1}$  extensive failure of the specimen prohibited measurement of the cone angles. From the limited number of results available there appears to be a trend of decreasing primary cone angle with increasing impact velocity. This variation is similar to the results obtained for CDM glass ceramic, Ceran and tungsten carbide impacts on alumina. Similarly, the expanding contact area during the initial stages of the impact accounts for the change in cone crack angle. Initially this result appears contradictory to the observed increase in cone angle with increasing impact velocity produced by hardened steel sphere impacts on alumina. One possible explanation is that in the alumina case, radial flow of the projectile over the specimen surface generated extra shear stresses which affect cone crack propagation. For the boron carbide, however, the Imacon sequence

(fig.31b) shows clearly that fracture of the hardened steel projectile occurs, resulting in a dramatic reduction in the radial flow of the projectile. Consequently, the extra shear stresses which influence the cone crack are not generated. Fracture of the hardened steel ball is more likely to occur on impact with boron carbide due to the more intense shock wave, and hence reflected tensile wave, generated by the impact and the higher strain-rate loading.

The secondary cone crack angle appears to be independent of the impact velocity. This cone forms later in the impact process when the rate of expansion of the contact area has reduced and therefore has little effect on the cone crack propagation.

Extensive failure of the hardened steel projectile was observed for all impacts above  $\sim 200 \text{ m s}^{-1}$ . Penetration of the specimen by the projectile fragments was not observed for the range of impact velocities investigated,  $< 830 \text{ m s}^{-1}$ . By causing break-up of the projectile, the impact energy is distributed over a larger area of the specimen.

In a number of specimens, stress waves generated by the impact resulted in spalling of flakes from defects in the boron carbide. The site of such a spall is shown in fig.32 in the upper right-hand portion of the tile. Clearly these defects may influence the impact performance of the tile and should, therefore, be eliminated.

#### **(b) Tungsten Carbide**

Tungsten carbide sphere impacts were performed on the boron carbide at impact velocities up to  $\sim 800 \text{ m s}^{-1}$ . At a velocity of  $\sim 105 \text{ m s}^{-1}$ , radial failure of the specimen was produced. A cone crack of semi-apex angle  $51^\circ \pm 2^\circ$  was formed; however, no lateral cracking or specimen compaction occurred. The projectile on impact suffered extensive brittle failure. Increasing the impact velocity to approximately  $225 \text{ m s}^{-1}$  increased the number of radial failures. Secondary cone cracking was also observed at this impact velocity. A similar response was also observed at  $\sim 345 \text{ m s}^{-1}$ , the degree of damage being greater. In both these cases, the projectile failure was to such an extent that no piece larger than  $0.5 \text{ mm}$  was found! It was not possible to establish whether spall failure occurred because of the extensive damage in the specimen.

A high-speed Imacon sequence of a  $760 \text{ m s}^{-1}$  impact of tungsten carbide on boron carbide (fig.33) shows high-speed jetting of fine material from the impact site. Lateral cracking was also observed in this specimen along with extensive radial failure and multiple cone cracking. The impact loading causes disintegration of the projectile.

The measured cone crack angles for various impact velocities are presented in Table 7. Above  $350 \text{ m s}^{-1}$  extensive failure made measurement of the cone angle impossible. These results indicate that the primary cone angle decreases as the impact velocity increases. This is in accord with previous results and is



attributed to the expanding contact area during the initial stages of the impact. Similarly, the secondary cone crack angle appears to be independent of impact velocity.

From the limited number of specimens available it is difficult to compare the damaged produced by hardened steel and tungsten carbide projectiles. It appears, however, that the tungsten carbide projectile produces qualitatively more damage than the hardened steel at the same impact velocity. This can be partly attributed to the increase in the initial impact pressure,

$$P_{\text{tungsten carbide}} = 1.25 P_{\text{hardened steel}}$$

Further, the tungsten carbide projectile produces compaction and jetting of the boron carbide, which could not be achieved with the hardened steel sphere. These results further support the inclusion of hardness or yield stress of the materials to characterise the impact.

#### 2.4.6 Front surface photography

In the sequences illustrated in figs. 34 to 36, a 5 mm steel ball impacts various targets. The Imacon camera is positioned so that the front surface of the target is viewed. Fig. 34a shows an impact at  $245 \text{ m s}^{-1}$  onto Sintox alumina in which the ball rebounds with a flattened impact face. In frame 1 the ball, B, approaches the specimen and it's shadow, S, can also be seen. Impact takes place in frame 2 and a plume, P, of metal fragments (not ceramic) ejects sideways. The ball then rebounds leaving a metallic deposit on the specimen. Below  $180 \text{ m s}^{-1}$ , all impacts onto alumina rebounded, while above  $250 \text{ m s}^{-1}$  all impacts caused fragmentation of the ball. The range of behaviour is due to the balls having a range of strengths. Fig. 34b shows an impact at 250 in which the steel ball fractures into a few pieces. Finally, fig. 34c shows an impact onto alumina at  $350 \text{ m s}^{-1}$  which causes intense fragmentation of the ball.

Figure 35\* is an interesting example since the small conical fragment (see figs. 24 and 25c) can be seen detaching from the ball in frames 3 onwards. This impact was at a velocity of  $242 \text{ m s}^{-1}$ .

In fig. 36a, the steel ball impacts a 10 mm thick MDF cement tile. This material has a low hardness and the ball penetrates the surface. Complete penetration occurred for this material at 120, 375 and  $900 \text{ m s}^{-1}$  for 3, 6 and 10 mm thick specimens respectively.

#### 2.4.7 Double layer ceramics

Some of the harder ceramics such as boron carbide and the aluminas may be effective at disrupting a projectile but are expensive (BC) or denser (aluminas) compared with the glass ceramics or MDF cement (see Tables 1-3).

---

\* Note that the small black spot at the centre of each frame on this and some of the other Imacon sequences is an artefact due to a damage mark on the photo-sensitive cathode of the camera.

We have performed some experiments with a harder facing plate of ceramic glued on the front of a softer (cheaper) ceramic. The question we were interested in was the thickness of the facing plate required to disrupt a 5 mm steel projectile. Fig. 36b shows a  $250 \text{ m s}^{-1}$  impact onto a 3 mm thick Sintox alumina plate backed by a 10 mm thick MDF cement plate. In this situation, the steel ball is not broken but the Sintox plate is shattered (clearly the backing plate is not stiff enough to prevent bending and extensive radial fracture ensues).

However, a 4 mm thick front plate of Sintox did disrupt a steel ball at velocities of  $200 \text{ m s}^{-1}$  and above. Since tungsten carbide spheres fragment at lower velocities than steel spheres we would also expect that this arrangement would defeat WC projectiles.

#### 2.4.8 Momentum balance

A momentum balance was designed to catch debris (for example the cone) and the projectile (if it penetrated). The angular deflection of the balance allowed the trapped energy and momentum to be calculated. It was also possible to measure the mass and dimensions of the ejected material and from the measured momenta to calculate the ejection velocity of the debris. Over 100 experiments of this type were made and the data are summarised in figs. 19 and 20 (the cone angles for the Ceran glass ceramic, and Sintox alumina plotted against non-dimensional impact velocity and the absolute impact velocity respectively) fig. 37 (the mass of the ejected cone as a function of velocity), fig. 38 (the velocity of the ejected cone,  $V$ , as a function of velocity) and fig. 39 (the variation of the average base diameter of alumina cones versus velocity). Figs. 21, 27, 28, 29 and 49 gives examples of the trapped cones or fragments. Finally, the two sequences in fig. 40 show the momentum balance,  $M$ , in action. In fig. 40a a 5 mm steel ball,  $B$ , impacts a 10 mm thick specimen of sintox alumina held in a holder,  $H$ , at a velocity of  $290 \text{ m s}^{-1}$ . A single cone, labelled  $S$ , detaches and travels at ca.  $4 \text{ m s}^{-1}$  to be caught in the momentum balance. The impact velocity in fig. 40b is about  $400 \text{ m s}^{-1}$  and a double cone ejects.

The main discussion of the cone angle data (fig. 19 and 20) is reserved until later (section 3-4) but note that with the glass ceramic the angle **decreases** along the curve ABC. At point B, spall and secondary cone formation starts and the conical-shaped crater enlarges. This effect is also apparent in fig. 37 which plots the ejected mass. The cone, which is the only fragment ejected, has a decreasing angle over the region A B but then over the range B D the ejected mass increases due to spall and the secondary cone. Fig. 21 shows what the debris looks like at various velocities for the glass ceramic.

With alumina, the cones persist up to much higher velocities. Fig. 29 includes 8 examples for the velocity range  $300$  to  $650 \text{ m s}^{-1}$  and shows pictorially how their angles, masses and average base diameters,  $d$ , increase with impact velocity.

The curves for the mean velocity of the ejected material,  $V$ , show a steadily rising curve for the alumina. This reflects the changing shape of the cone.

The curve for the glass ceramic is more complex but it is reasonable to relate the onset of spall, secondary cone formation and intense fragmentation with the various stages.

#### 2.4.9 Glass plus metal layer targets

A lengthy series of experiments with soda-lime glass specimens and metal layers has been completed. High-speed sequences were taken in all cases. Variables were as follows:

- (i) Projectile velocities in range 50 to 425 m s<sup>-1</sup>.
- (ii) Glass thickness 8, 10, 19, 25 mm.
- (iii) Steel plates of thickness 0.71 or 2.03 mm added to the rear surface.
- (iv) Steel plates of thickness 1.00, 0.71, 2.03 or 3.05 mm added to the front surface.
- (v) Steel plates of thicknesses 0.71 mm added to both front and rear surfaces.

Table 8 gives details of the sequences illustrated in figs. 41 to 44. In all cases, a 5 mm diameter steel ball was used.

Table 8

Figure No.	Shot No.	$V_0$ /m s <sup>-1</sup>	$T_f$ /μm	t/mm	Steel plate
41	470	92.5	4.7	10	-
42	435	103	4.7	10	B.0.71 mm
43	476	207	4.7	10	F.2.03 mm
44	445	102	0.98	8	F. & B.0.71mm

$V_0$  is impact velocity,  $T_f$  is interframe time,  $t$  is the thickness of the glass,  $t_s$  is the thickness of the mild steel plate and F and B indicate where the mild steel plates were attached i.e. Front or Back. Note the black spot at the centre of each frame is an artefact. It is a damaged area of the tube in the Imacon.

Figure 41 shows the classic development of a Hertzian cone crack. Note the way the cone angle increases after it is about half way through the specimen. This is due to interaction with the stress waves reflected at the rear surface (see fig. 30). In the very final stage the crack curves to meet the rear surface at right angles. In later frames, a plume of debris ejects from the front surface. This is typical behaviour when the projectile is harder than the target.

Figure 42 is for a similar velocity impact but the steel plate at the rear prevents plate bending (which tends to reduce the Hertzian tensile stresses at the front surface). A consequence is that this time several cone cracks develop from the front surface. The cone behaviour is also modified by the stress wave reflection at the glass/steel interface which since it reflects as a **compression** wave makes the cone angle smaller rather than larger when it initially interacts.

Figure 43 is for a higher velocity impact but this time there is a steel plate at the front. At this velocity, this thickness plate is sufficient to prevent Hertzian-type crack growth from the front. However, the rear surface (spall-type) damage remains intense.

Figure 44 is for an impact velocity of  $\sim 100 \text{ m s}^{-1}$  again (as for figures 41 and 42) but with steel plates at front and back surfaces. The plate is thinner than that in figure 43 (about 1/3rd) and this added to the greater rigidity given to the system by the back plate allows both Hertzian crack growth and spall damage.

#### 2.5.0 Front surface photography of impacts on glass

In these experiments, the soda-lime glass specimens were viewed from the front with the angle between the line of flight of the projectile and the axis of the camera equal to  $15^\circ$ . Just the right-hand half of each impact is viewed. Table 9 summarises the experimental details. The symbols are as defined in Table 8.

**Table 9**

All impacts by a 5 mm diameter steel ball.

Figure No.	Shot No.	$V_0/\text{m s}^{-1}$	$T_f/\mu\text{s}$	$t/\text{mm}$
45	499	48.5	4.7	8
46	494	103.5	4.7	8
47	534	207	0.98	8
48	536	402	0.98	10

Figure 45 is for a relatively low impact velocity and although there is some radial cracking, what we see predominantly is the growth of the cone. The banded appearance of the cone (one band is labelled B in frame 4) is due to the slight changes in trajectory caused by interaction with stress waves reflecting to and fro in the plate thickness.

Figure 4b is for a similar experiment but at the higher

impact velocity of  $103.5 \text{ m s}^{-1}$ . The ball impacts in frame 2 and a cone crack, C, can be seen in frame 3. However, the higher velocity causes much more plate bending and radial fracture. These radial cracks start at the rear surface as illustrated in fig. 12. At a velocity of  $207 \text{ m s}^{-1}$ , the radial cracking is more intense (fig. 47) with the crack front moving at about  $1500 \text{ m s}^{-1}$  (the maximum crack velocity for soda-lime glass). However, with further increase in impact velocity the crack pattern, at least initially, becomes increasingly dominated by stress wave damage rather than quasi-static failure modes such as Hertzian or radial cracking. Fig. 48 is an example of impact at  $402 \text{ m s}^{-1}$ . The short circumferential cracks are typical of stress wave damage. The grouping of the cracks into bands is due to reinforcement of the Rayleigh surface wave on the front surface being reinforced by reflected tensile waves from the rear surface. Such cracks have been analysed in detail by Bowden and Field (1964).

### 3. DISCUSSION AND CONCLUSIONS

The mechanical properties of a wide range of brittle materials have been measured. Controlled impact experiments described in this report have identified the failure modes of the target material and projectile for a range of impact velocities and material parameters. The failure produced is, principally, dependent upon the relative hardness of the target and projectile. Materials with a hardness less than that of the projectile produce limited plastic deformation of the sphere. For sufficiently high impact velocities penetration of the target by the projectile can be achieved. Impact of hardened steel and tungsten carbide cause extensive failure of the projectile; penetration of the target by the projectile is not observed. In all the impacts investigated the damage produced by tungsten carbide is significantly greater than that of hardened steel which in turn is greater than that produced by lead projectiles. Further, the tungsten carbide projectile was, for the range of velocities studied, the only one capable of causing compaction, jetting, and lateral cracking in the alumina and boron carbide targets.

Various properties have been suggested as important for a ceramic in body-armour application. These include strength,  $K_{IC}$ , modulus, hardness, crack velocity, stress wave velocities, Weibull parameter, density, Poisson ratio, etc.... The first point to make is that the impact process with a brittle target is so complex that no single property is likely to dominate, but rather a group of properties.

A considerable effort has been made to improve the toughness of ceramics. While this can be beneficial in many applications, our view is that it is not of major importance compared with hardness. The hardness of the ceramic, compared with that of the projectile, has been shown conclusively by our research to be the dominant property (when just a single plate is involved).

### 3.1 Fracture modes

Table 10 summarizes the critical velocities for damage modes produced by 5 mm diameter ball impacts. Most of the values are given in the text. The table summarises a very large amount of data. On the other hand, it has to be appreciated that in some cases the number of specimens was very limited and they were not always of the optimum thicknesses. The data for steel ball impacts are the most precise.

Note the very different behaviour depending on whether the projectile or specimen hardness is the greater. The aluminas are harder than steel and lead but not so hard as the tungsten carbide. Tungsten carbide projectiles are able to plastically deform the aluminas and give, for example, lateral cracks which are a result of residual stresses resulting from plastic flow. It was also possible to observe a plume of ceramic debris from the impact site for tungsten carbide impacts and alumina see Table and fig. 33. However, although very hard the tungsten carbide fractures relatively easily.

### 3.2 Energetics of Impact

Using data obtained above, it is useful to consider the energetics of a typical impact with a single tile. As an example we take a 5 mm steel ball impacting a ceramic at  $300 \text{ m s}^{-1}$ . Two cases are of interest: (i) impact with, for example, an alumina tile which deforms and breaks the projectile; and (ii) impact with, for example, a glass ceramic tile which does not deform the projectile.

#### (a) Alumina

Experiment shows that the projectile is plastically deformed from a diameter of 5 mm to ca. 4.1 mm in the direction of impact (pushed in an amount  $h = 0.9 \text{ mm}$ ), the rebound energy of the projectile fragments is about 15% of the input energy, a cone is produced of mass  $2 \times 10^{-3} \text{ kg}$  which ejects at ca.  $4 \text{ m s}^{-1}$  (note, very slowly!). The calculated energies are:

$$\begin{aligned} \text{Input energy} &= 23 \text{ J,} \\ \text{Rebound energy} &= 3.5 \text{ J.} \end{aligned}$$

Energy to create a cone (area  $\times$  fracture surface energy =  $17 \text{ J m}^{-2}$  for alumina) =  $0.005 \text{ J}$  (note, very small!). Kinetic energy of cone =  $0.016 \text{ J}$  (note, very small). Energy to plastically deform projectile =  $\int_0^h Y \times \text{area } dx$ , where  $Y$  = yield strength (taken as hardness/3) =  $18.5 \text{ J}$  (note, very large). Small amounts of energy will go into heat, sound, and tile vibrations.

The conclusion is that the fracture properties (fracture surface energy,  $K_{Ic}$ ) have an almost negligible effect, and that the ability to deform the projectile plastically is paramount. Efforts to increase the  $K_{Ic}$  of a ceramic are unlikely to be beneficial.

### (b) Glass Ceramic

Experiment shows that at  $300 \text{ m s}^{-1}$  the projectile is **not** deformed or fractured. There is intense fragmentation in the vicinity of the impact. The projectile penetrates the tile:

Input energy = 23 J.

Energy to fragment a volume of ceramic of roughly the dimension of the projectile to micron size =  $0.76 \text{ J}$  (the calculations assumes a fracture surface energy of  $19 \text{ J m}^{-2}$  and that micron-sized cubes are formed. If ten micron-sized cubes were found the energy used would be  $0.076 \text{ J}$ . Both are very small).

The conclusion is that most of the energy continues as kinetic energy of the ball plus fragments. Again the small effect of fracture surface energy, or toughness ( $K_{Ic}$ ), is emphasized, particularly if the ceramic can not deform the projectile.

### 3.3 The Cone

The two great advantages of a ceramic armour compared to a metallic are: (i) the lower density; (ii) the load spreading. The point is that whereas the hole formed by impact with a metal has a diameter of about the same size as the projectile the ceramic forms a conoid which spreads the load. This conoid of damage may be a coherent cone (see earlier) or a collection of fragments. The cone tends to have an apex angle less than for static loading (figs.13,19, 20 and 49) but with alumina impacted by steel the angle increases with velocity. Further, the stress wave interaction (fig.30) increases the angle further so that at an impact velocity of  $300 \text{ m s}^{-1}$  on alumina of 9 mm thickness, the base has a diameter of ca. 19 mm and at  $600 \text{ m s}^{-1}$  a diameter of ca. 30 mm (fig. 39). Clearly, the thicker the ceramic the greater the base area. This is an added reason why the best potential ceramics are those with a large  $H/\rho$  ratio where  $H$  is hardness and  $\rho$  is density, though with the added restriction that the  $H$  for the ceramic  $H_c$  needs to be greater than the projectile hardness  $H_p$ .

### 3.4 Variation of cone angle with velocity

In earlier work in this laboratory, (Knight et al. 1977 and Chaudhri 1985) a similar trend of decreasing  $\theta$  with increasing velocity for impacts on "pyrex" and fused silica glasses with steel balls was observed. The variation of  $\theta$  with impact velocity is attributed to the expanding contact radius between the impacting projectile and the target. The typical stress trajectories for a Hertzian stress field are shown in fig.50 (Huber 1904; Lawn et al. 1974). These trajectories are such that the tangents and normals to the curves at any point indicate the directions of the principal stresses. The contact radius between the sphere and flat is represented by  $oa$ . For quasi-static indentations, a ring crack initiates from a suitable defect just outside the contact radius when sufficient stress has been generated in the specimen by the indentation load. Subsequent growth of the ring crack follows a stress trajectory, thereby producing a cone crack.

During quasi-static indentation, if subsequent loading results in the contact area encompassing the surface traces of the cone crack, the cone crack ceases to propagate. In the case of a dynamic indentation, however, cone cracks within the area of contact continue to grow. A cone crack which initiates during the impact loading at a point just outside the contact area will initially propagate along a stress trajectory near the point *a*. As the impact loading continues, the contact area expands and the crack follows a stress trajectory which is in the region *oa*. From fig.50, it can be seen that these trajectories are at a steeper angle. The resulting cone crack therefore, has a smaller semi-apex angle compared with the quasi-static value.

For all impact velocities, the ring crack initiates at approximately the same contact radius because the stresses generated in the substrate are principally dependent upon the contact area (Andrews 1931; Adler 1975). As the velocity of the impact area increases, the final contact area between the ball and the flat increases. The final stages of the cone crack propagation therefore, follow stress trajectories closer to *o* as the velocity of the impact increases. This results in a decrease in the semi-apex angle of the cone crack with increasing velocity as observed. Further work is needed to **quantitatively** analyse the variation of the cone angle with impact velocity.

Impacts on a small number of specimens produced cone cracks with an uncharacteristically small semi-apex angle (fig.13). The formation of these small angled cones is attributed to the presence of a large failure-initiating defect at the impact site. A ring crack will initiate from this defect at a low stress which corresponds to a small contact area. The later stages of cone crack propagation will, therefore, follow stress trajectories near the origin of the impact, *o*, resulting in a small angled cone.

For similar reasons, the values of  $\theta$  for aluminas are smaller than those for static loading. The small but definite increase of  $\theta$  with velocity (figs. 19 and 20) is we think due to the fact that the projectile plastically deforms on impact and the radial flow over the tile surface generates shear stresses which influence the cone crack propagation.

The fact that tungsten carbide projectiles fracture relatively easily may explain why the cone angle decreases, at least initially, with increasing velocity (Table 5). The eventual increase of  $\theta$  for the highest velocity may be because the very finely divided debris flows laterally and modifies the stress distribution.

#### 4. CONCLUSIONS

The report summarises a large amount of data on the impact behaviour of a wide range of ceramic systems obtained using high speed photography, a momentum balance and post impact microscopy.

Glass ceramics have the advantage of relatively low density compared with the aluminas so that for a given weight thicker



samples can be used. This allows the base diameter of the cone of debris to be larger. However, their hardnesses are less than steel and they do not damage the projectile significantly. Experiments with layered systems have shown that a front plate of alumina or other hard material (if of sufficient thickness) can break up a steel projectile. Such systems can then use a lower hardness and/or cheaper backing ceramic.

The cone not only spreads the load but produces fragments of relatively low velocity (see for example fig. 38). It is reasonably easy to "catch" such material with a polymer fabric or composite.

The work has shown that several of the properties of a ceramic are important. However, it appears that  $K_{IC}$  is **not** particularly important. A key ratio is that of  $H/p$  where  $H$  is the hardness and  $p$  the density with the added restriction that the hardness of the ceramic needs to be greater than that of the projectile.

## REFERENCES

- Adler W.F. - (1975) *J. Non-cryst. Solids* **19**, 335.
- Andrews J.P. - (1930) *Lond. Edinb. Dubl. Phil. Mag.* **9**, 593.
- Andrews J.P. - (1931) *Proc. Phys. Soc. Lond.* **43**, 18.
- Arbiter N., Harris C.C. & Stamboltzis G.A. - (1969) *Trans. AIME* **244**, 118.
- Bowden F.P. & Brunton J.H. - (1961) *Proc. Roy. Soc. A* **262**, 433.
- Bowden F.P. & Field J.E. - (1964) *Proc. Roy. Soc. A* **282**, 331.
- Chaudhri M.M. - (1985) in **Strength of Inorganic Glass**, NATO Conference Series VI: Materials Science, Plenum Press.
- Chaudhri M.M., Knight C.G. & Swain M.V. - (1976) *Proc. 12th Cong. on High-speed Photography*, Toronto, 371.
- Dorre E. & Hubner N. - (1984) **Alumina Materials Research and Engineering**, publ. Springer-Verlag, Berlin.
- Ferguson W.J. & Rice R.W. - (1971) *Mat. Sci. Research* **5**, 261.
- Field J.E. - (1962) Ph.D. Thesis, University of Cambridge.
- Field J.E. - (1971) *Contemp. Phys.* **12** (1), 1.
- Field J.E. - (1983) *Contemp. Phys.* **24** (5), 439-459.
- Field J.E., Camus J-J. & Gorham D.A. - (1970) *Proc. 3rd Int. Conf. on Rain Erosion and Associated Phenomena*, Royal Aircraft Establishment, England, 303.
- Field J.E., Gorham D.A. & Rickerby D.G. - (1979a) in **Erosion: Prevention and Useful Applications**, ASTM STP 664, ed. Adler W.F., American Society for Testing and Materials, 298.
- Field J.E., Gorham D.A., Hagan J.T., Matthewson M.J., Swain M.V. & van der Zwaag S. - (1979b) *Proc. 5th Int. Conf. on Erosion by Liquid and Solid Impact*, paper 13, Cambridge: Cavendish Laboratory.
- Field J.E., van der Zwaag S. & Townsend D. - (1983) *Proc. 6th Int. Conf. on Erosion by Liquid and Solid Impact*, paper 19, Cambridge.
- Gorham D.A. & Rickerby D.G. - (1975) *J. Phys. E* **8**, 794.
- Hagan J.T. & Swain M.V. - (1978) *J. Phys. D: Appl. Phys.* **11**, 2091.
- Huber M.T. - (1904) *Ann. Physik. U. Chemie* **14**, 153.
- Hutchings I.M. & Winter R.E. - (1975) *J. Phys. E* **8**, 84.
- Johnson W. - (1972) **Impact Strength of Materials**, publ. Arnold, London.
- Kaye G.W.C. & Laby T.H. - (1973) **Tables of Physical and Chemical Constants**, 13th edn., publ. Longman, London.
- Knight C.G., Swain M.V. & Chaudhri M.M. - (1977) *J. Mat. Sci.* **12**, 1573.
- Lawn B.R., Wilshaw T.R. & Hartley N.E.W. - (1974) *Int. J. Fract.* **10**, 1.
- Lynch C.T. - (1975) **Handbook of Materials Science Vol. II**, CRC Press, U.S.A.
- Matthewson M.J. & Field J.E. - (1980) *J. Phys. E* **13**, 355.
- Morrell R. - (1985) **Handbook of Properties of Technical and Engineering Ceramics**, Her Majesty's Stationery Office.
- Pope P.H. - (1985) Cavendish Laboratory, Private Communication.
- Rice R.W. - (1977) **Treatise on Materials Science and Technology**, ed. MacCrone R.K., **11**, 199.

- Schardin H. - (1959) in **Fracture**, ed. Auerbach et al., Wiley, New York.
- Schott - **Schott Glass in Formation**, .....
- Seigel A.E. - (1965) **The Theory of High-speed Guns**, AGARDograph, **91**.
- Swain M.V. & Hagan J.T. - (1980) J. Mat. Sci. **15**, 387.
- Townsend D. & Field J.E. - (1987) Annual Report on Contract DAJA45-85-C-0021
- Tilly G.P. & Sage W. - (1970) Wear **16**, 447.
- With G. de - (1984) J. Mat. Sci. **19**, 2195.
- Woodward A.C. & Field J.E. - (1974) 11th Int. Cong. on High-speed Photography, London.
- Zwaag van der S. - (1981) Ph.D. Thesis, University of Cambridge.
- Zwaag van der S. - (1983) Eng. Frac. Mech. **17**, 367.

Table 1

Material	$K_{Ic}$ / MN <sup>3/2</sup>	$\sigma_f$ / MPa	Flaw size / $\mu$ m	Threshold Water / m s <sup>-1</sup>	Threshold Velocity / m s <sup>-1</sup>	Threshold Mild Steel / m s <sup>-1</sup>	Velocity / m s <sup>-1</sup>	Vickers Hardness / GPa
Sapphire	1.80	362	~ 10	300 - 350		20 < $v_s$ < 23		12.0
Alumina	2.71	146	250	300 - 350		22 < $v_s$ < 25		12.0
MDF Cement	3.0	124	300	250 - 275		34		2.2
Soda-lime- glass	0.75	100	40	150 <sup>(1)</sup>		19		4.5
Hot-pressed silicon nitride	5.2	265	260	500 <sup>(2)</sup>		38		16.0

(1) van der Zwaag (1981)

(2) Matthewson (1978)

TABLE 2

Material	Density $\rho/\text{kg m}^{-3} \times 10^{-3}$	Hardness $H_V/\text{GPa}$	Fracture Toughness $K_{IC}/\text{MN}^{-3/2}$
Alumina	3.69	$11.9 \pm 1.6$	$2.99 \pm 0.17$
CDM	2.48	$9.2 \pm 0.5$	$1.77 \pm 0.12$
Ceran	2.59	$8.2 \pm 1.1$	$0.42 \pm 0.05$
Robax	2.52	$9.2 \pm 1.6$	$0.44 \pm 0.04$
WC	14.9	16	
Lead	11.4	0.04	
Boron carbide	2.52	$20.6 \pm 3.3$	$2.5 - 5.0^{(1)}$
Soda-lime glass	2.50	$4.5 \pm 0.5$	$0.75 \pm 0.02$
MDF - cement	2.48	$2.2 \pm 0.2$	$3.0 \pm 0.2$
Hardened steel	7.8	10	

<sup>(1)</sup> Morrell (1985)

Table 3

Material	Density $\rho/10^3 \text{ kg m}^{-3}$	Longitudinal Stress Wave $C_L/\text{m s}^{-1}$	Shear Stress Wave Velocity $C_S/\text{m s}^{-1}$	Shear Modulus G/GPa	Bulk Modulus K/GPa	Youngs Modulus E/GPa	Poissons Ratio $\nu$
Ceran 0.24 (1)	2.59	6360	3640 $\pm 50$	34.3 $\pm 0.9$	59	92 (1)	
Robax	2.52	5870 $\pm 100$	3630 $\pm 50$	33.3 $\pm 0.9$	42.5 $\pm 2.6$	79.2 $\pm 4.0$	0.19 $\pm 0.012$
Soda-lime glass	2.50	5600 $\pm 100$	3325 $\pm 50$	27.6 $\pm 0.8$	42.5 $\pm 2.7$	79.2 $\pm 3.0$	0.19 $\pm 0.02$
CDM glass ceramic	2.47	6100 $\pm 150$	3760 $\pm 50$	34.8 $\pm 0.9$	45.5 $\pm 3.4$	83.3 $\pm 4.0$	0.20 $\pm 0.03$
Sintox alumina	3.69	8890 $\pm 300$	5415 $\pm 100$	108 $\pm 4$	147 $\pm 10$	260 $\pm 10$	0.21 $\pm 0.03$
Deranox 975 alumina	3.75	9700 $\pm 300$	5510 $\pm 100$	114 $\pm 4$	200 $\pm 15$	288 $\pm 15$	0.26 $\pm 0.03$
Hilox 973 alumina	3.77	9760 $\pm 300$	5450 $\pm 100$	112 $\pm 4$	210 $\pm 15$	285 $\pm 15$	0.27 $\pm 0.03$
Alumina + zirconia	3.99	9570 $\pm 300$	5580 $\pm 100$	124 $\pm 4$	200 $\pm 15$	310 $\pm 20$	0.24 $\pm 0.03$
Alumina + zirco- nia duplex duplex structure	4.12	9710 $\pm 300$	5710 $\pm 100$	134 $\pm 5$	210 $\pm 15$	330 $\pm 20$	0.24 $\pm 0.03$
Boron carbide	2.50	12,800 $\pm 600$	7640 $\pm 150$	146 $\pm 5$	215 $\pm 20$	360 $\pm 30$	0.22 $\pm 0.03$
MDF cement	2.48	5,100 $\pm 100$	2960 $\pm 20$	21.8 $\pm 0.3$	35.4 $\pm 2.5$	54.3 $\pm 3.0$	0.24 $\pm .02$
Hardened steel	7.8	5850	3150	77.4	163.7	201	0.30
Tungsten carbide	14.9	6650	3980	236	344.2	576	0.22
Lead	11.4	2000	700	5.59	38.2	16	0.43

(1) Schott glass information

TABLE 4

Property	Techniques
Hardness, H	Vickers hardness indentation.
Fracture toughness, $K_{IC}$	Crack growth from a Vickers hardness indentation (Lawn and Fuller, 1975).
Wave velocities	Shear and longitudinal wave velocities determined from the transit time of pulses through a measured thickness using transducers.
Elastic moduli and Poisson ratio	Calculated from the wave velocities.
Fracture velocities	High-speed photography and ultrasonic modulation techniques (Schardin 1959, Field 1971).

Table 5

Semi-apex Cone Angle produced by Tungsten Carbide  
Sphere Impact on Alumina at various Velocities

Impact Velocity / $\text{m s}^{-1}$	Semi-apex Cone Angle, $\theta^\circ$
80	$52 \pm 3$
110	$47 \pm 2$
175	$48 \pm 2$
200	$45 \pm 2$
280	$46 \pm 3$
460	$42 \pm 3$
710	$45 \pm 3$



Table 6

Semi-apex Cone Angles produced by Hardened Steel  
Sphere Impact on Boron Carbide at various Velocities

Impact Velocity / $\text{m s}^{-1}$	Primary Cone Semi-apex Angle	Secondary Cone Semi-apex Angle
120	$47^\circ \pm 2^\circ$	$61^\circ \pm 3^\circ$
225	$37^\circ \pm 2^\circ$	$64^\circ \pm 3^\circ$
255	$39^\circ \pm 2^\circ$	$60^\circ \pm 3^\circ$
330	$32^\circ \pm 2^\circ$	$64^\circ \pm 3^\circ$

Table 7

Semi-apex Cone Angles produced by Tungsten Carbide  
Sphere Impacts on Boron Carbide at various Velocities

Impact Velocity / $\text{m s}^{-1}$	Primary Cone Semi-apex Angle	Secondary Cone Semi-apex Angle
105	$51^\circ \pm 2^\circ$	-----
225	$40^\circ \pm 3^\circ$	$60^\circ \pm 40^\circ$
345	$37^\circ \pm 3^\circ$	$59^\circ \pm 40^\circ$

TABLE 10

Critical velocities for damage modes produced by 5 mm ball impacts.

Mode of failure	CDM		CERAN		ALUMINA (SINTOX)		BC		MDF CEMENT	
	Steel	WC	Steel	WC	Steel	WC	Steel	WC	Steel	WC
Onset of damage	20		18		23				34	
Hertzian crack initiated	40	<100	20						50	
Cone ejected	55 (9.8)	<100 (9.8)	40 (10)	30 (10)	220 (8.6)	80(8.6)	<120	<105	50 (6mm)	
Lateral crack	80		32 (8.1)	<100	None	Yes	None	760	100	
Lateral cracks reach surface	200	<100		<100	>900(8.6)	300(8.6)	>400(6.7)	760	200	
Spall	120 (9.8)	<100 (9.8)	100(10)						120(3)	
									300(6)	
									600(10)	
									100(3.6)	
									180(10)	
									300	
Radial	60 (9.8)				200(8.6)	50	120(6.7)	<105 6.7)	120 (3)	
Second cone Penetration	300			<100	None<1000		<120		375 (6)	
	450 (9.8)	400 (9.8)	300 (10)	270(10)			None<830		900 (10)	
Static $\theta$	72 $\pm$ 3		69 $\pm$ 3		64 $\pm$ 3				None	
Projectile damage	None	None	None	None	Yes	Yes	Yes	Yes	100	
Plume of debris	120	Yes	150	Yes	Not of Ceramic	>400	None	>760		
Rebound of sphere										
Fragmentation of sphere					<180	<80				
					>250	>80	Yes			

**Footnote**

All velocities in  $m s^{-1}$ . The figures in brackets refer to specimen dimension in mm. A gap in the Table does not mean that the particular damage mode is absent but lack of specimens prohibited measurement.

**FIGURE CAPTIONS**

- Fig.1 Schematic diagram of the various stages in the impact of a cylindrical jet on a solid target.
- Fig.2 (a) Schematic diagram of the nozzle assembly (not to scale).  
(b) The variable velocity air gun (not to scale).
- Fig.3 Impact damage produced in zinc sulphide by a 0.8 mm water jet with velocity of  $200 \text{ m s}^{-1}$ .
- Fig.4 Schematic diagram of the hydraulic pressure tester apparatus.
- Fig.5 Variation of the residual fracture stress with jet impact velocity for soda-lime glass. Jet from the 0.8 mm orifice (van der Zwaag and Field 1983):  
(a) Plateau region, specimen strength comparable with unimpacted material.  
(b) Transition region.  
(c) All specimens damaged by impact in this region.
- Fig.6 Residual strength curves for sapphire, alumina, macro-defect-free cement, hot-pressed silicon nitride, and soda-lime glass (Matthewson 1978; van der Zwaag 1981).
- Fig.7 Schematic diagram of gas gun (not to scale).
- Fig.8 Schematic diagram of specimen holder (not to scale).
- Fig.9 (a) Schematic of ultrasonic technique for fracture velocity measurement.  
(b) Ultrasonic markings on soda-lime glass; vertical dimension of the surface is 6.3 mm.  
(c) Ceran.  
Both at a frequency  $5 \times 10^6 \text{ Hz}$ .
- Fig.10 A 50 mm x 50 mm x 9.8 specimen of glass ceramic after a  $240 \text{ m s}^{-1}$  impact with a 5 mm diameter hardened steel sphere.  
(a) Impact face with extensive radial cracking and removal of material from lateral crack formation.  
(b) Rear surface of specimen showing area of failure produced.
- Fig.11 Schematic diagram of the crack formation during the impact of a sphere upon a brittle material. The dark area corresponds to the permanent deformation of the material. Hertzian cone cracks, c, initiate near the edge of the contact area during the loading cycle. Under continued loading secondary cone cracks form. Lateral cracks, lc, occur on the unloading cycle.
- Fig.12 Schematic diagram of initiation of radial cracks, rc, before cone crack, c, propagation is completed.

- Fig.13 Semi-apex cone angle,  $\theta$ , versus impact velocity for glass ceramic. a and b are uncharacteristically small angle cone cracks (see text).
- Fig.14 Imacon sequences, with interframe time of  $4.25 \mu\text{s}$ , of the impact of a 5 mm diameter hardened steel sphere. The frames are numbered 1 to 8:  
 (a) Impact velocity of  $310 \text{ m s}^{-1}$  on a 6mm thick, specimen of soda-lime glass, s. A plume of high velocity fine particles, p, is produced by the impact. Fine particles of spalled material, m, are produced from the rear of the specimen with a maximum velocity of approx.  $250 \text{ m s}^{-1}$ .  
 (b) A  $240 \text{ m s}^{-1}$  impact on a 9.8 mm thick specimen, s, of glass ceramic. Jetting of fine particles, p, due to deformation of the material underneath the projectile is observed from frame 2. Cracks, c, are visible on the front face of the specimen.
- Fig.15 (a) Scanning electron micrograph of a 5 mm diameter hardened steel sphere after impact at  $240 \text{ m s}^{-1}$  on glass ceramic.  
 (b) Impact area showing central undamaged region, u, the eroded zone, e, and the embedded glass particles, g.  
 (c) A high magnification view of the impact area.
- Fig.16 Schematic diagram of the propagation of the crushed zone and formation of the fine particle jetting material:  
 (a) Contact velocity  $>$  propagation velocity of crushed zone (dark region).  
 (b) Contact velocity  $<$  propagation velocity of crushed zone, and jetting can occur.
- Fig.17 Imacon sequence, with transmitted illumination and an interframe time of  $0.95 \mu\text{s}$ , of the crack system produced by the impact of a 5 mm diameter hardened steel sphere at a velocity of  $250 \text{ m s}^{-1}$  on the edge of a plate 50 mm x 50 mm x 5 mm of: (a) transparent glass ceramic; and (b) soda-lime glass. The crack velocity in the material is estimated from the growth of the cracks labelled c. Surface defects in the material, r, are extended by the Rayleigh surface wave. The plume of fine particles, p, is also evident.
- Fig.18 Imacon sequences, with transmitted illumination and  $0.95 \mu\text{s}$  interframe time, of the crack systems produced by a  $250 \text{ m s}^{-1}$  impact of a 3 mm diameter hardened steel sphere on: (a) transparent glass ceramic (6 mm x 50 mm x 5 mm); and (b) soda-lime glass (12 mm x 50 mm x 5 mm). The rear surface cracks, s, are caused by reflection of the compressive loading pulse as a tensile surface wave. Lateral cracks, l, are formed which reach the surface of the specimen resulting in material removal. The plume of fine particles, p, and the surface defects, r, extended by the Rayleigh surface wave are also evident.

- Fig.19 Semi-apex cone angle plotted against the non-dimensional velocity  $V/V_c$  where  $V$  is the absolute velocity and  $V_c$  the velocity for a cone crack to be ejected.  $V_c = 32 \text{ m s}^{-1}$  for the glass ceramic Ceran and  $220 \text{ m s}^{-1}$  for the Sintox alumina. With the glass ceramic  $\theta$  decreases (curve ABC). At point B the conical crater has an increasing  $\theta$  due to secondary cone formation and spall (curve BD).
- Fig.20 The same data as for fig. 19, but plotted in terms of absolute velocity.
- Fig.21 Damage to  $50 \times 50 \times 8.1 \text{ mm}$  specimens of Ceran at different velocities. All viewed from the rear. With this material, the cone ejects at a velocity of  $32 \text{ m s}^{-1}$ . Ejected debris recovered from the momentum balance.
- Fig.22 Imacon sequences of a  $5 \text{ mm}$  diameter hardened steel sphere impact on aluminium. The specimen is labelled "s" and the frames numbered 1 to 8:  
 (a) Impact velocity of  $160 \text{ m s}^{-1}$ , interframe  $17.2 \mu\text{s}$ . The impact occurs between frames 2 and 3. Ball rebounds from frame 3 onwards with a velocity of  $60 \pm 5 \text{ m s}^{-1}$ . Note the flattened surface of the projectile, F, after impact. Material is expelled from the rear of the specimen after impact. In the photographs, this appears as an apparent increase in specimen thickness.  
 (b) Impact velocity of  $295 \text{ m s}^{-1}$ , interframe time  $4.25 \mu\text{s}$ . The projectile fractures on impact. Cracks, C, are observed in the rear surface of the specimen from frame 6 onwards.
- Fig.23 Scanning electron micrograph of a  $5 \text{ mm}$  diameter hardened steel sphere after impact at  $200 \text{ m s}^{-1}$  on alumina. A flat, f, is formed on the projectile and cracks, c, are observed.
- Fig.24 Schematic diagram of the failure observed in a hardened steel sphere after impact on alumina. An inverted cone, n, is formed in the sphere and fracture planes, r. The arrows indicated the radial movement of material observed with high velocity impacts.
- Fig.25 Scanning electron micrographs of the fragments of a hardened steel sphere produced by impact on an alumina at a velocity of  $275 \text{ m s}^{-1}$ :  
 (a) Cross-section of the sphere showing fracture plane, c, the flat, f, the flow lines, l, and the region, n, of the inverted cone.  
 (b) High magnification of the impact area shown in (a).  
 (c) The inverted cone of material produced in the sphere by the impact.

Fig.26 Scanning electron micrographs of a hardened steel sphere after impact at  $460 \text{ m s}^{-1}$  on an alumina specimen:  
 (a) The contact area between sphere and specimen showing the base of the inverted cone, n, and extensive radial, q.  
 (b) Side view of specimen shown in (a).

Fig.27 Impact damage produced in a  $50 \text{ mm} \times 50 \text{ mm} \times 10.5 \text{ mm}$  specimen of Sintox alumina by a  $5 \text{ mm}$  diameter hardened steel sphere impact at a velocity of  $250 \text{ m s}^{-1}$ :  
 (a) Impact face.  
 (b) Rear surface of specimens showing the area of failure due to cone crack formation.  
 (c) The cone of material produced by the impact. The upper portion of the cone corresponds to the propagation of the Hertzian crack. Interaction between the reflected tensile wave and the cone crack produces the roughening on the lower portion of the cone. The line of interaction between the cone crack and reflected wave is indicated, y.

Fig.28 Impact damage produced in a  $50 \text{ mm} \times 50 \text{ mm} \times 8.6 \text{ mm}$  piece of Sintox alumina by a hardened steel sphere impact at a velocity of  $225 \text{ m s}^{-1}$ :  
 (a) Impact face.  
 (b) Rear face of specimen illustrating area of cone failure.  
 (c) Cross-section of specimen through the impact area. The line of interaction between the crack front and the reflected tensile wave is indicated, y.  
 (d) Cone of material produced by the impact with upper smooth face and lower roughened face. The onset of the interaction between the reflected tensile wave and the propagating cone crack is shown at position y.  
 (e) Cross-section of specimen with cone of material.  
 (f) Plan view of the alumina cone produced by the impact.

Fig.29 Impacts on Sintox alumina at different velocities.  
 (a) the cones (b) the  $50 \times 50 \times 8.6 \text{ mm}$  plates viewed from the rear.

Fig.30 Schematic representation of the cone crack with the reflected tensile wave.

Fig.31 Imacon sequences of a 5 mm diameter hardened steel sphere impact with an interframe time of 4.25  $\mu$ s. The frames are numbered 1 to 8:

- (a) Impact velocity of 265 m s<sup>-1</sup> on an alumina specimen, s. The projectile fractures on impact.
- (b) An impact at a velocity of 255 m s<sup>-1</sup> on boron carbide. Failure of the ball, f, occurs on impact. Cracks, c, on the impact face of the material can be observed in frames 4-8.

Fig.32 A 50 mm x 50 mm x 6.7 mm specimen of boron carbide after 255 m s<sup>-1</sup> with a 5 mm diameter hardened steel sphere:

- (a) Impact face showing extensive radial cracking.
- (b) Rear surface of specimen.
- (c) Cross-section of specimen through the impact area. V denotes the impact direction of the projectile.

Fig.33 Impact of a tungsten carbide sphere at 760 m s<sup>-1</sup> on boron carbide. Note the plume of fragments which is reminiscent of a steel sphere on a glass ceramic.

Fig.34 Front surface photography of 5 mm steel ball impacts on 10 mm thick alumina specimens at (a) 245 m s<sup>-1</sup> (b) 250 m s<sup>-1</sup> and (c) 350 m s<sup>-1</sup>. B is the ball, S is the shadow and D a metallic deposit. The balls are successively flattened, shattered and fragmented frame interval 17.2 $\mu$ s. **Note** the black spot at the centre of each frame in this and the sequences in figs. 35, 36, 40, 45, 46, 47, 48 is an artefact due to a damage mark on the image tube of the Imacon.

Fig.35 An impact of a 5 mm steel ball onto an alumina specimen at 242 m s<sup>-1</sup>. The conical fragment (see text and figs. 24 and 25) can be seen detaching from the ball. Frame interval 17.2 $\mu$ s.

Fig.36 (a) A 5 mm steel ball impacts a 10 mm thick MDF cement tile and penetrates completely into the material ejecting a plume of debris, The ball was not damaged. Frame interval 17.2 $\mu$ s.  
(b) A ball, B, impacts a layered system with a 3 mm thick Sintox alumina tile glued to a 10 mm thick MDF cement tile at 250 m s<sup>-1</sup>. The Sintox is too thin and shatters, However, 4 mm thick Sintox front layers fractured steel spheres in the velocity range 250 and above, S is the shadow of the ball. Frame interval 17.2 $\mu$ s.

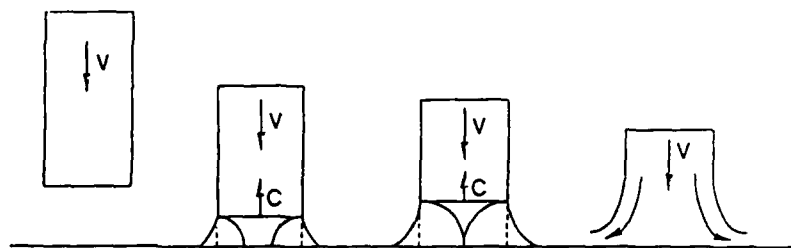
Fig.37 Data obtained with the momentum balance of the mass,  $m_c$  of the conical fragment for Sintox alumina and Ceran glass ceramic. See figs. 19 and 20 for a definition of  $V_c$ .

Fig.38 The mean velocity,  $V$ , of the conical fragments.

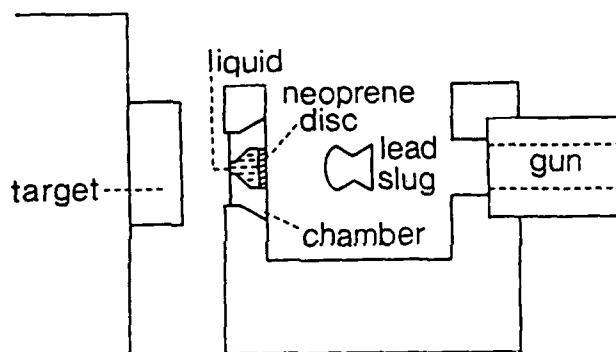
Fig.39 The mean base diameter,  $d$ , of the conical fragments.



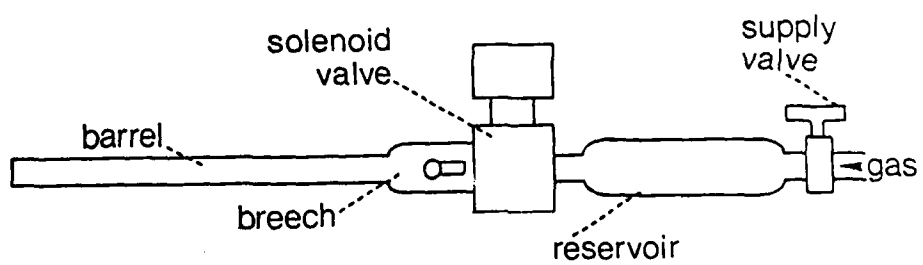
- Fig.40 Impacts of a 5 mm steel ball, B, at (a)  $290 \text{ m s}^{-1}$  and (b)  $400 \text{ m s}^{-1}$  against 10 mm thick Sintox alumina specimens. The specimens are held in a holder H. In (a), a single cone ejects and travels to the momentum balance, M, at about  $4 \text{ m s}^{-1}$ . In (b), a double cone ejects, frame interval  $17.2 \mu\text{s}$ .
- Fig.41 Impact of a 5 mm steel sphere onto a 10 mm thick soda-lime glass specimen at  $92.5 \text{ m s}^{-1}$ . A Hertzian cone forms. There is a small amount of rear surface damage, s, and lateral crack, l, formation. Frame interval  $4.7 \mu\text{s}$ .
- Fig.42 Impact of a 5 mm steel sphere onto a 10 mm thick soda-lime glass specimen backed by a 0.71 mm steel plate at  $103 \text{ m s}^{-1}$ . Frame interval  $4.7 \mu\text{s}$ .
- Fig.43 Impact of a 5 mm steel sphere onto a 10 mm thick soda-lime glass specimen with a 2.03 mm front steel plate at  $207 \text{ m s}^{-1}$ . Frame interval  $4.7 \mu\text{s}$ .
- Fig.44 Impact of a 5 mm steel sphere onto an 8 mm thick soda-lime specimen with front and rear steel plates of thickness 0.71 mm. Frame interval  $0.98 \mu\text{s}$ .
- Fig.45 Front surface angled view, with  $\theta$  the angle between the flight of the projectile and the axis of the camera  $= 15^\circ$ , of an impact onto 8 mm thick soda-lime glass at  $48.5 \text{ m s}^{-1}$ . The growth of the cone has a banded appearance due to interaction with stress waves. See text. Frame interval  $4.7 \mu\text{s}$ .
- Fig.46 As for fig. 45 but at  $103.5 \text{ m s}^{-1}$ .
- Fig.47 As for fig. 45 but at  $207 \text{ m s}^{-1}$ . Frame interval  $0.98 \mu\text{s}$ .
- Fig.48 As for fig. 45 but at  $402 \text{ m s}^{-1}$  and glass thickness 10 mm. **Note** the dominance at this velocity of stress wave damage. See text. Frame interval  $0.98 \mu\text{s}$ .
- Fig.49 Conical fragments (a) alumina at  $302 \text{ m s}^{-1}$  (b) alumina at  $356 \text{ m s}^{-1}$  (c) Ceran glass ceramic at  $33.5 \text{ m s}^{-1}$  and (d) ceran at  $35.6 \text{ m s}^{-1}$ . The changes in cone angle and surface roughness with the alumina samples are due to interaction with the reflected stress wave. With the glass ceramic, the reflected waves are much weaker and only have small effect.
- Fig.50 Side view of stress trajectories in Hertzian stress field. Plotted for  $v = 0.33$ ,  $oa$  denotes radius of contact.



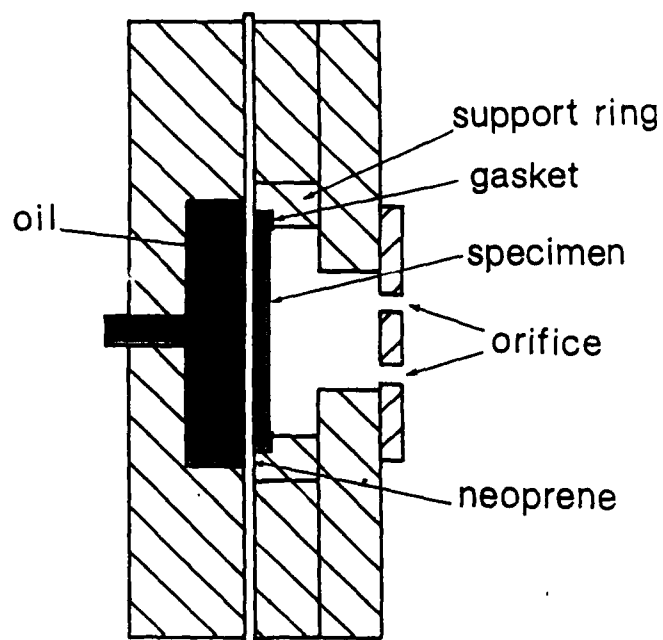
**1**



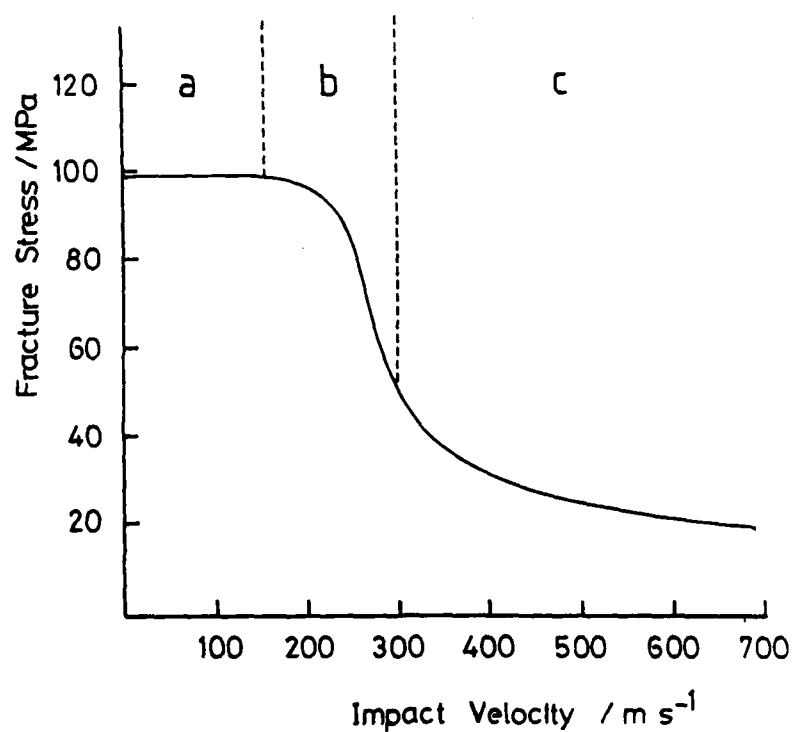
**2a**



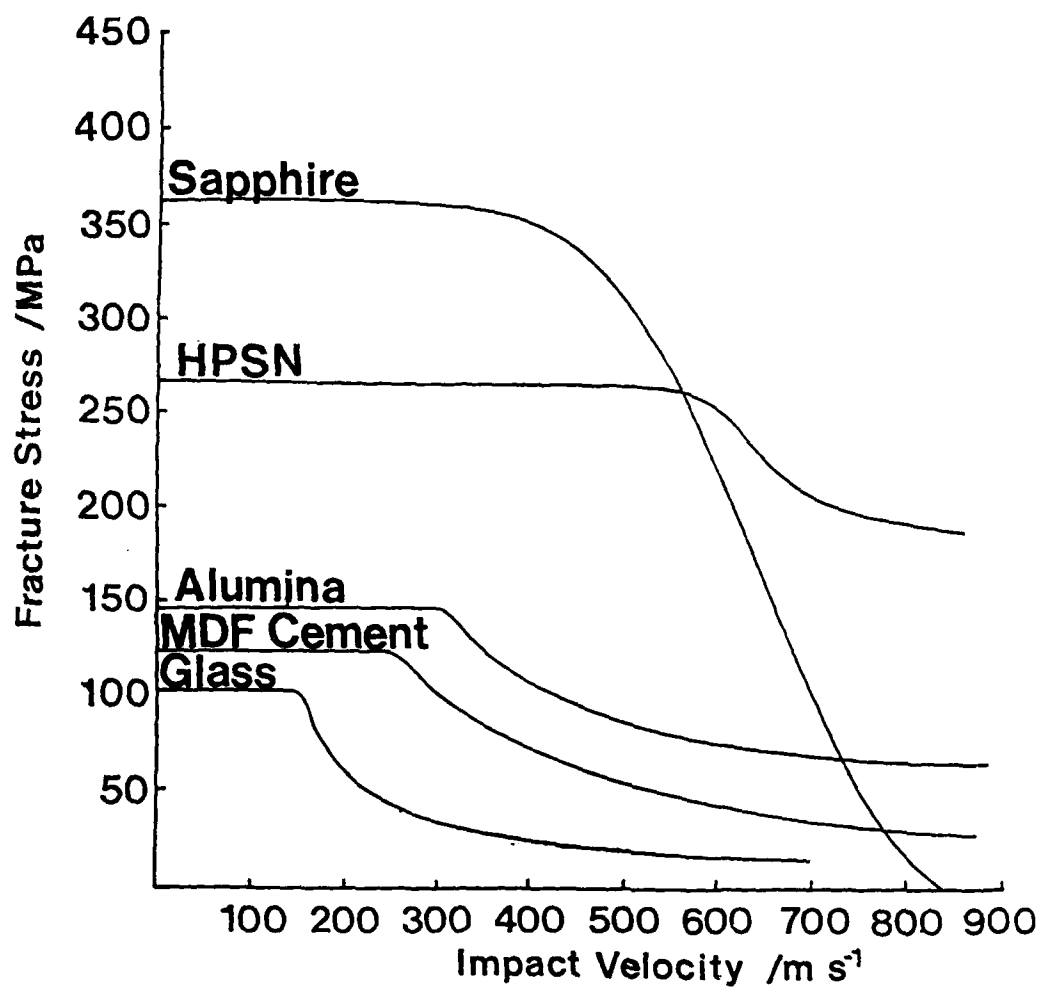
**2b**

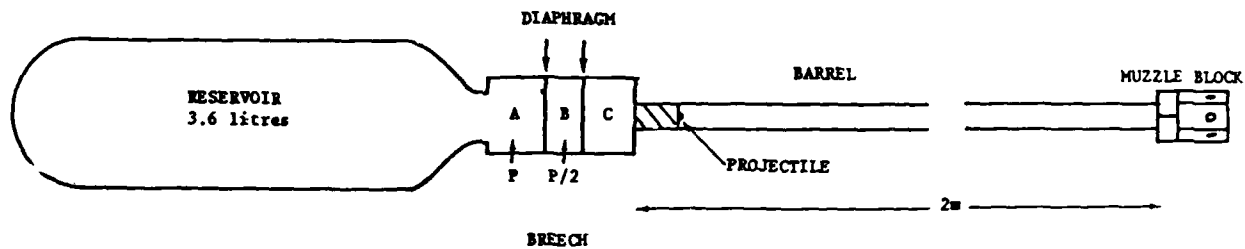


4

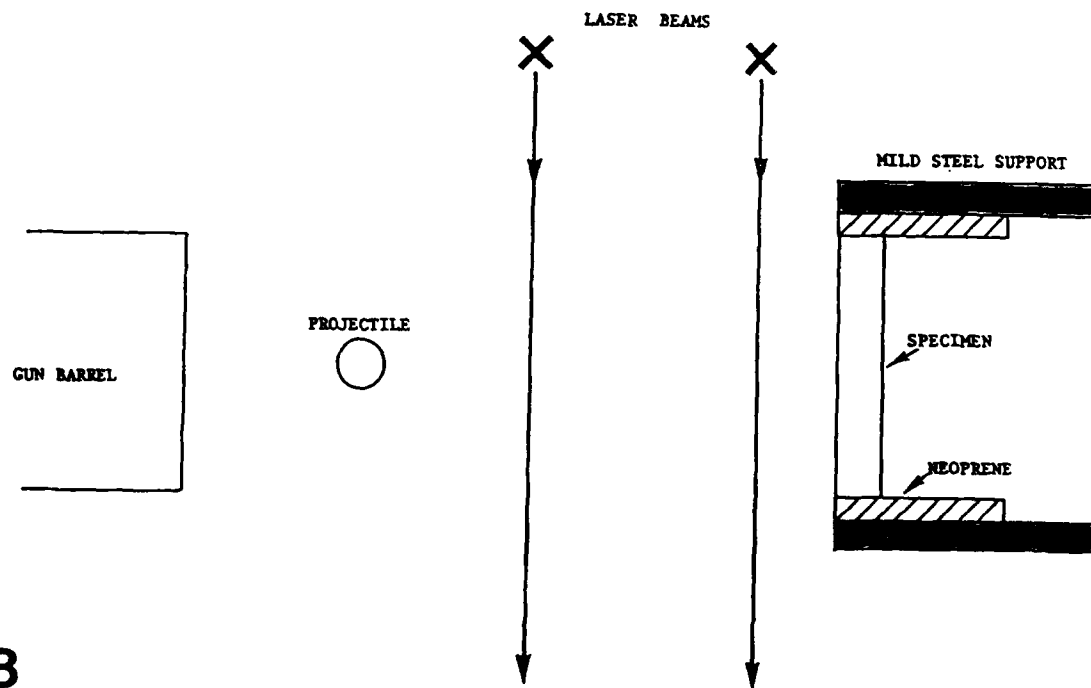


5

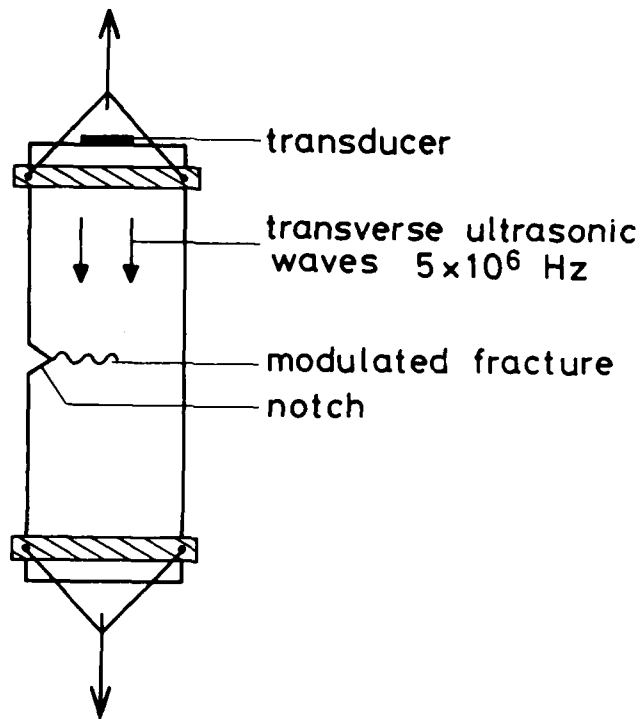




7

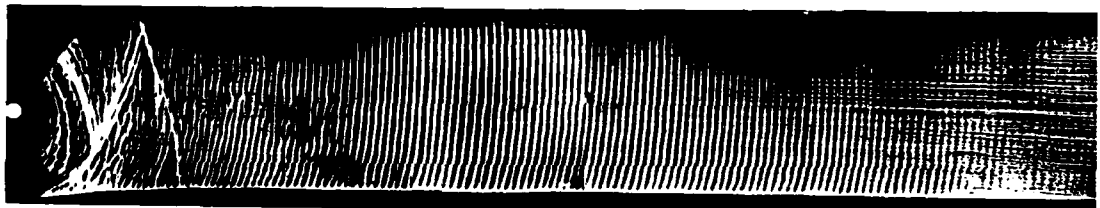


8

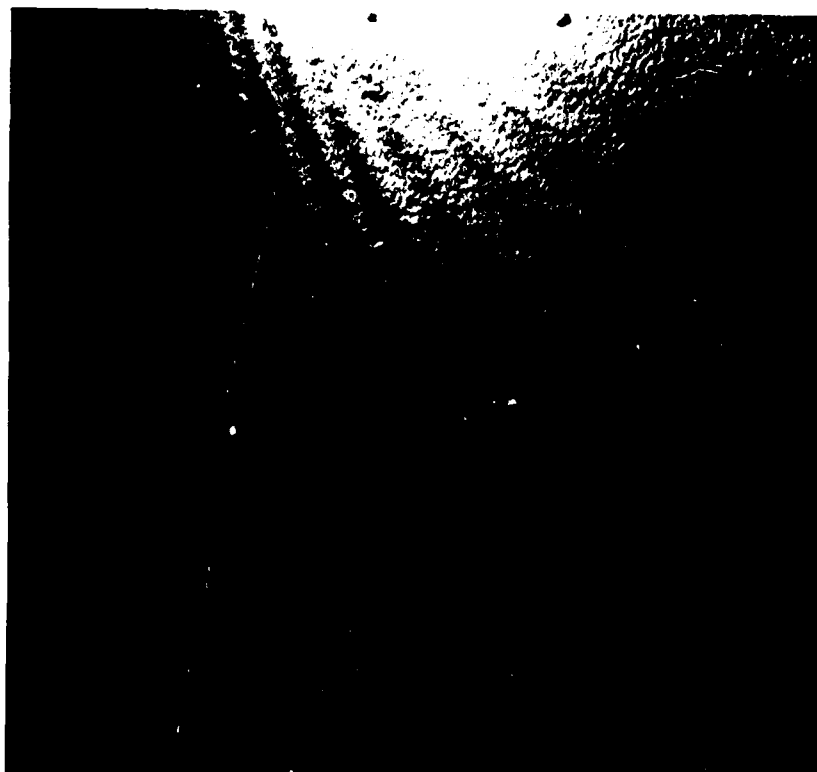


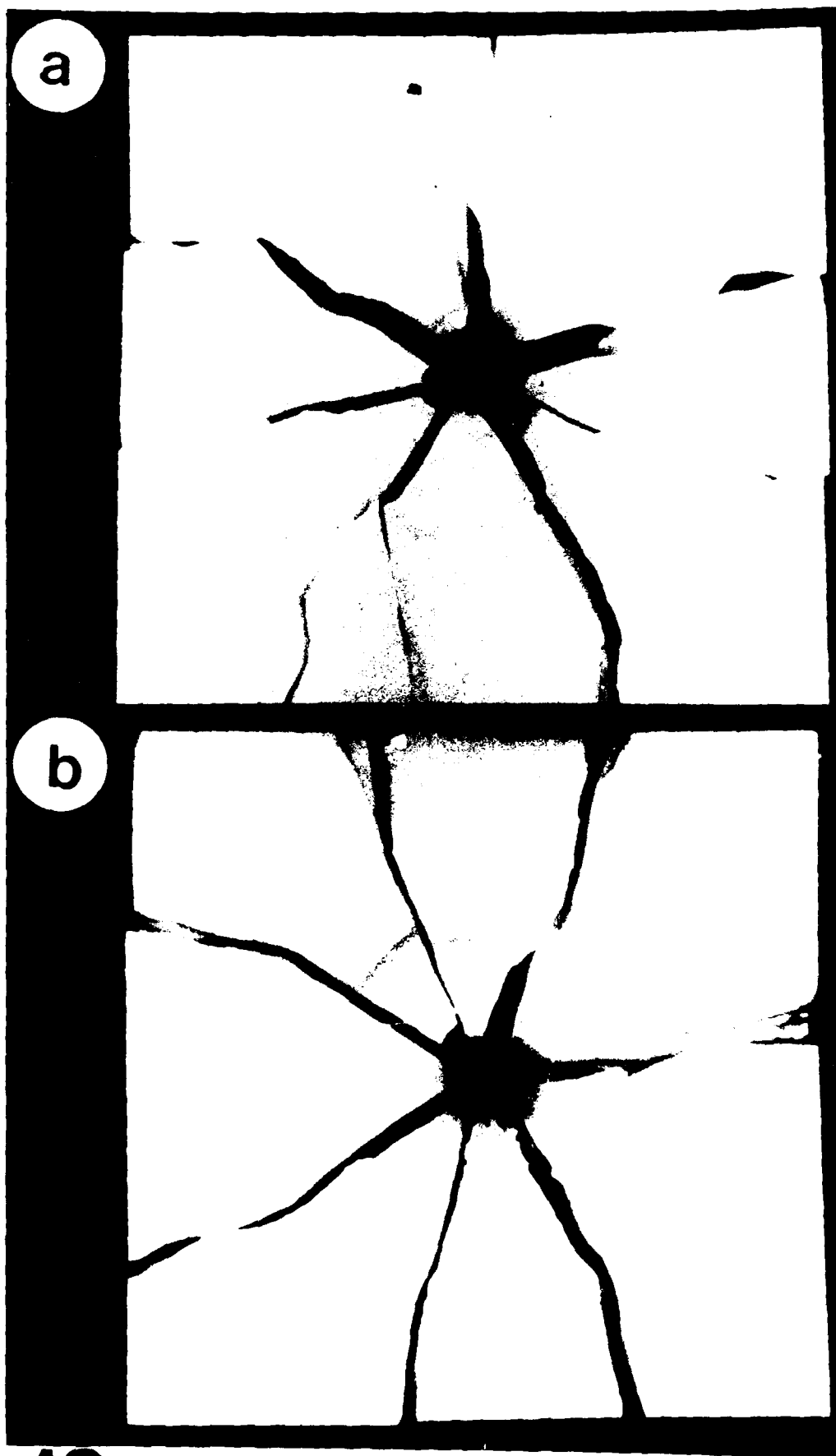
**a**

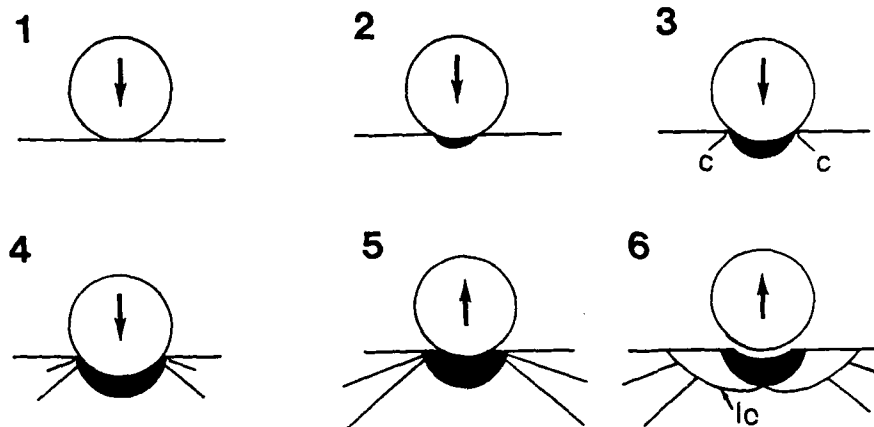
**b**



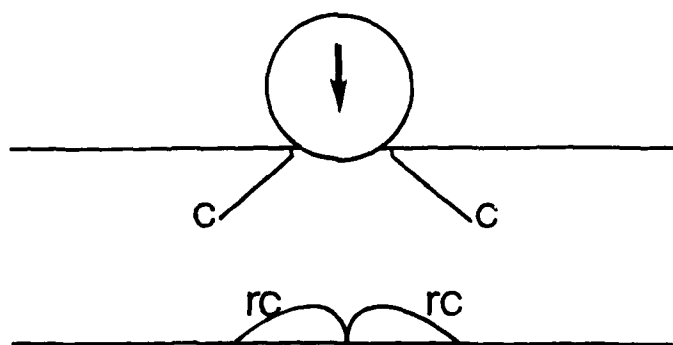
**c**  
**9**





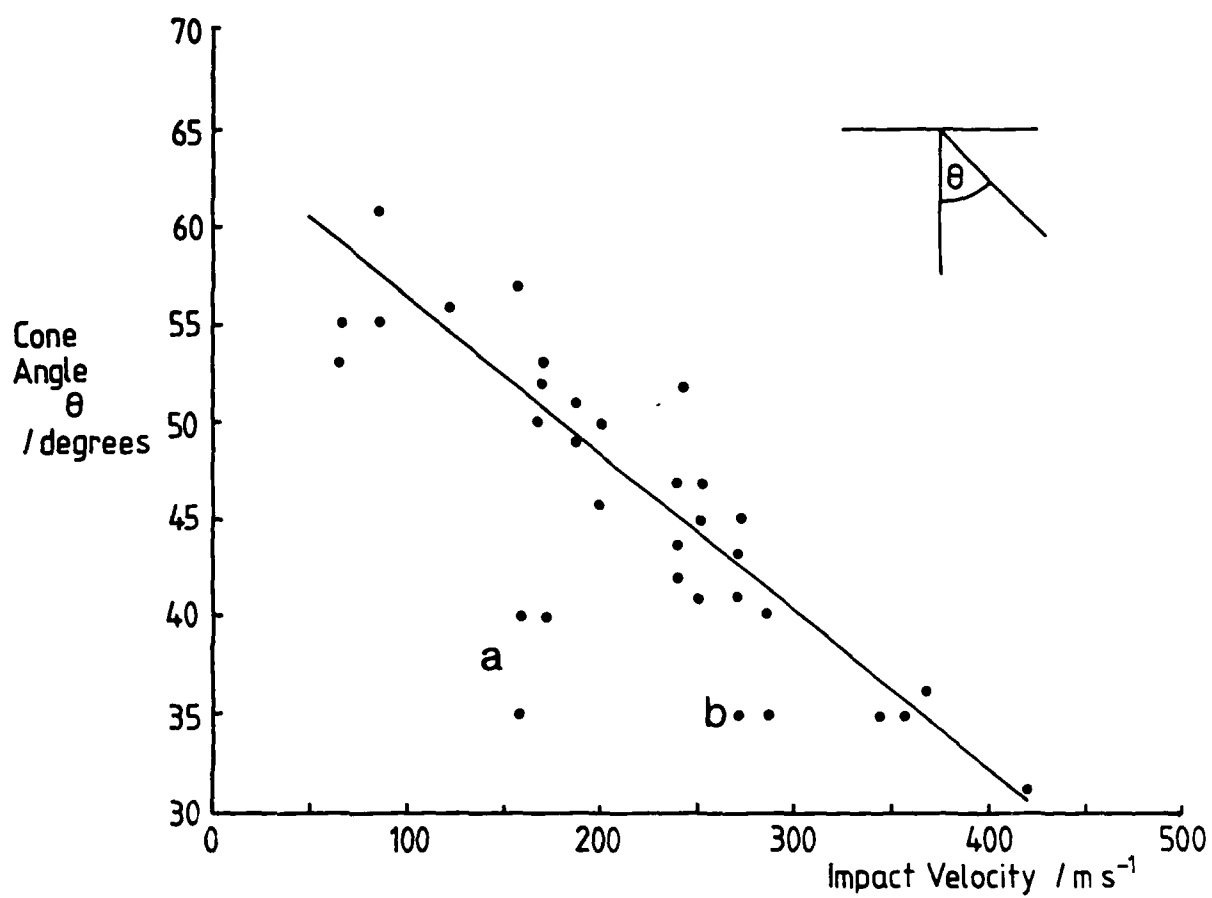


11

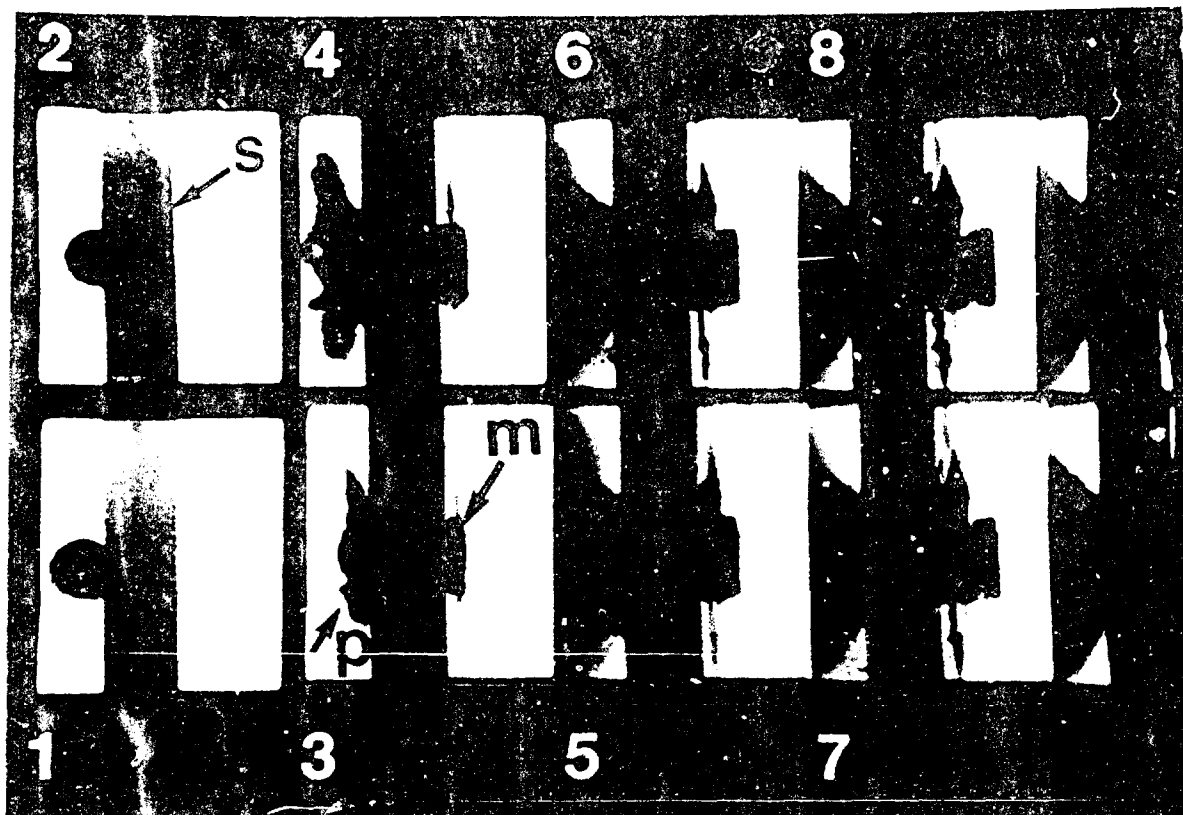


12

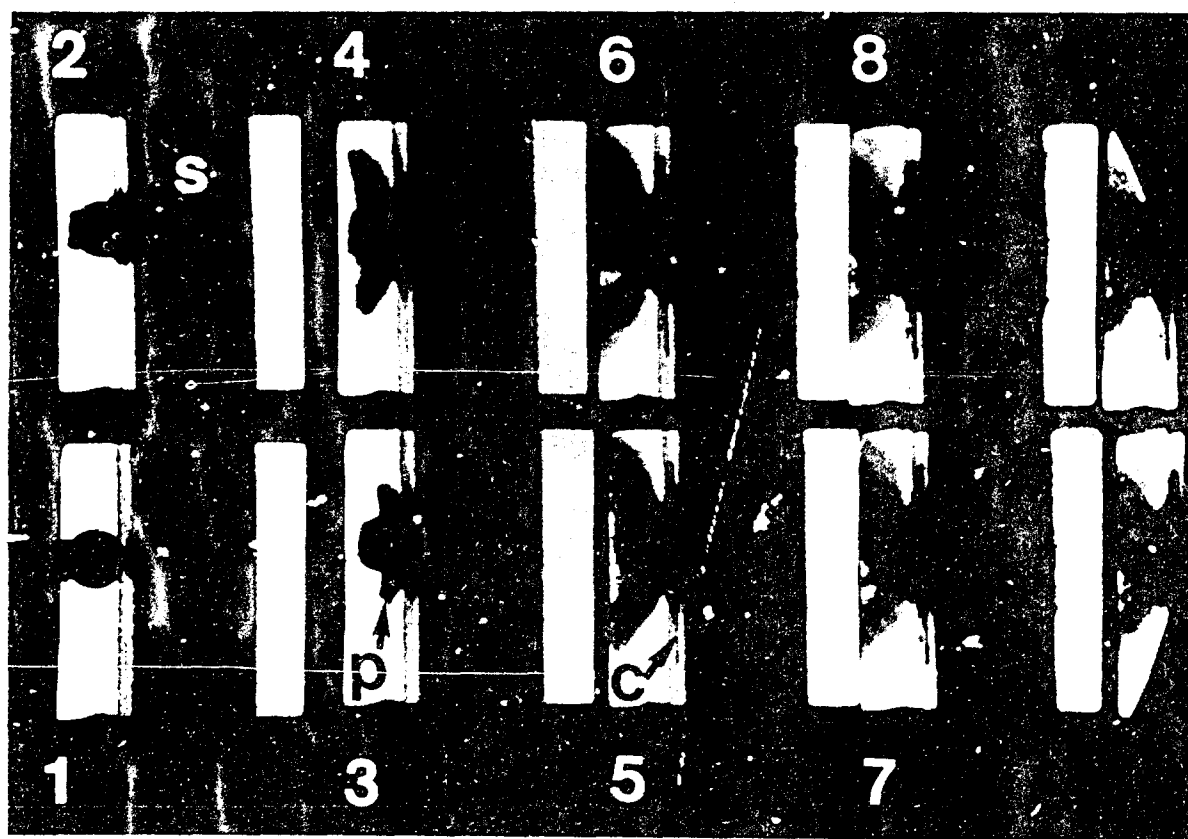


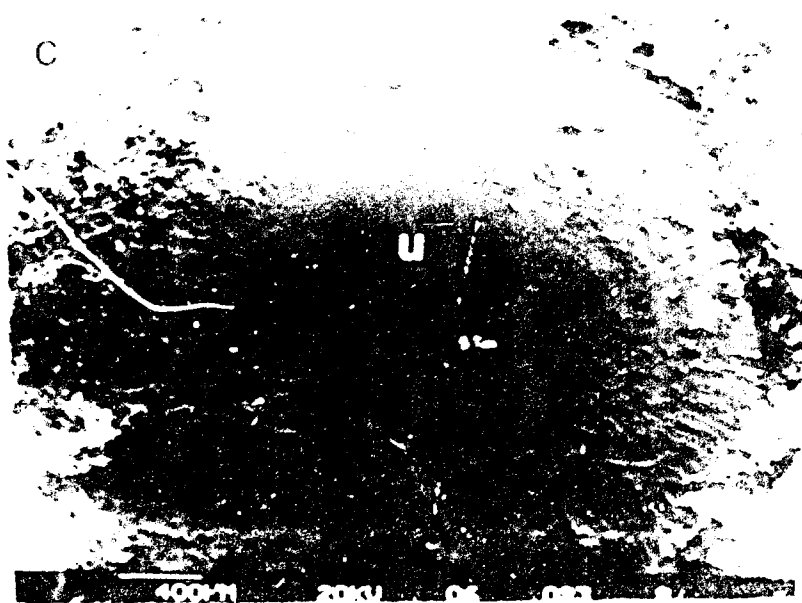
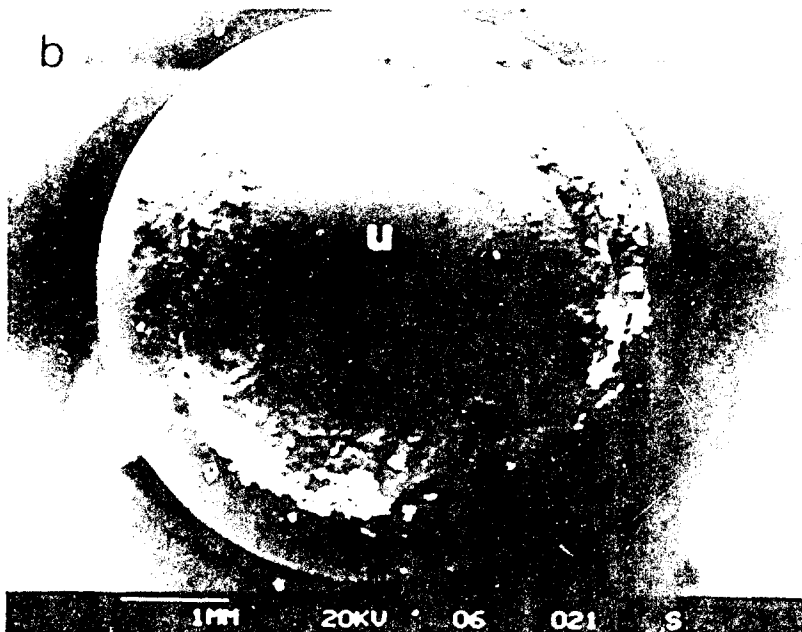
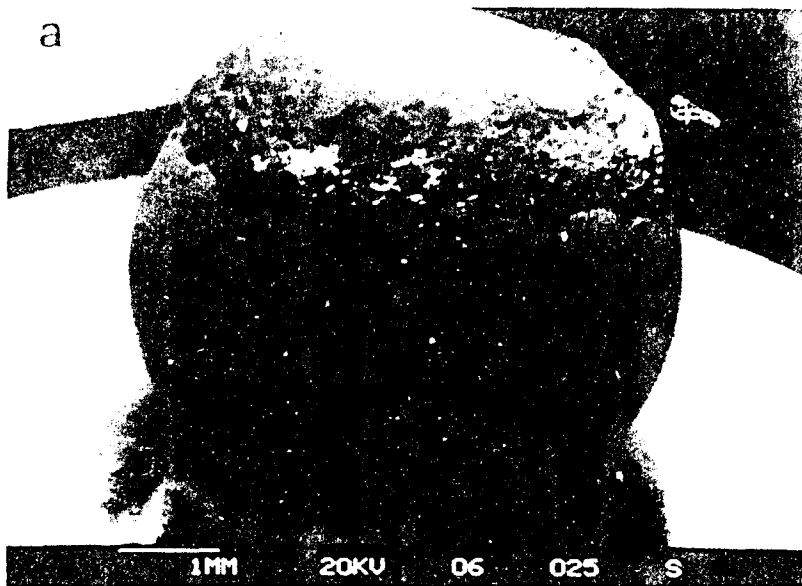


a

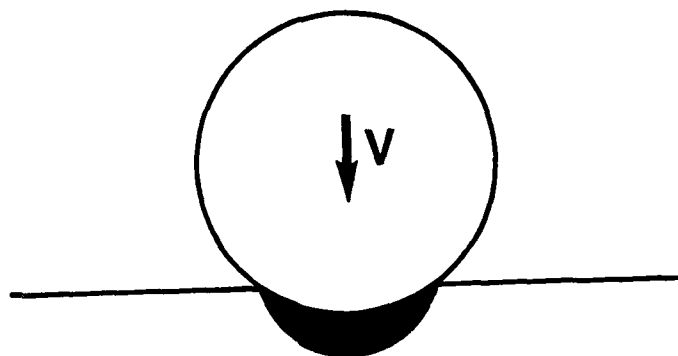


b

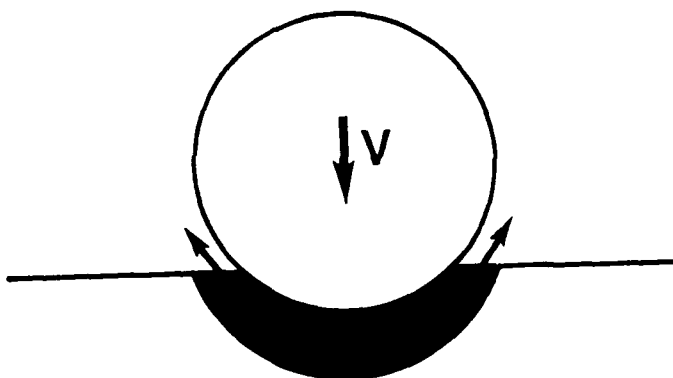




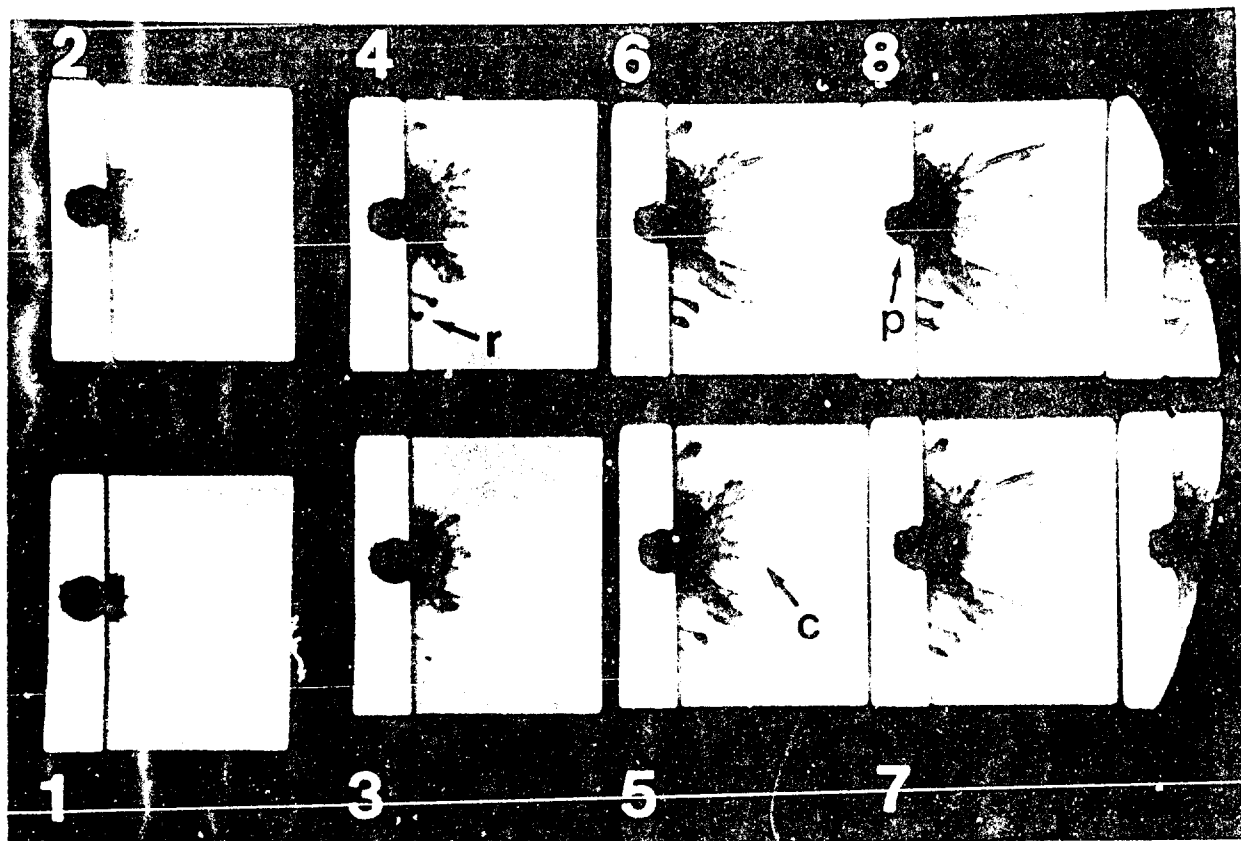
**a)**



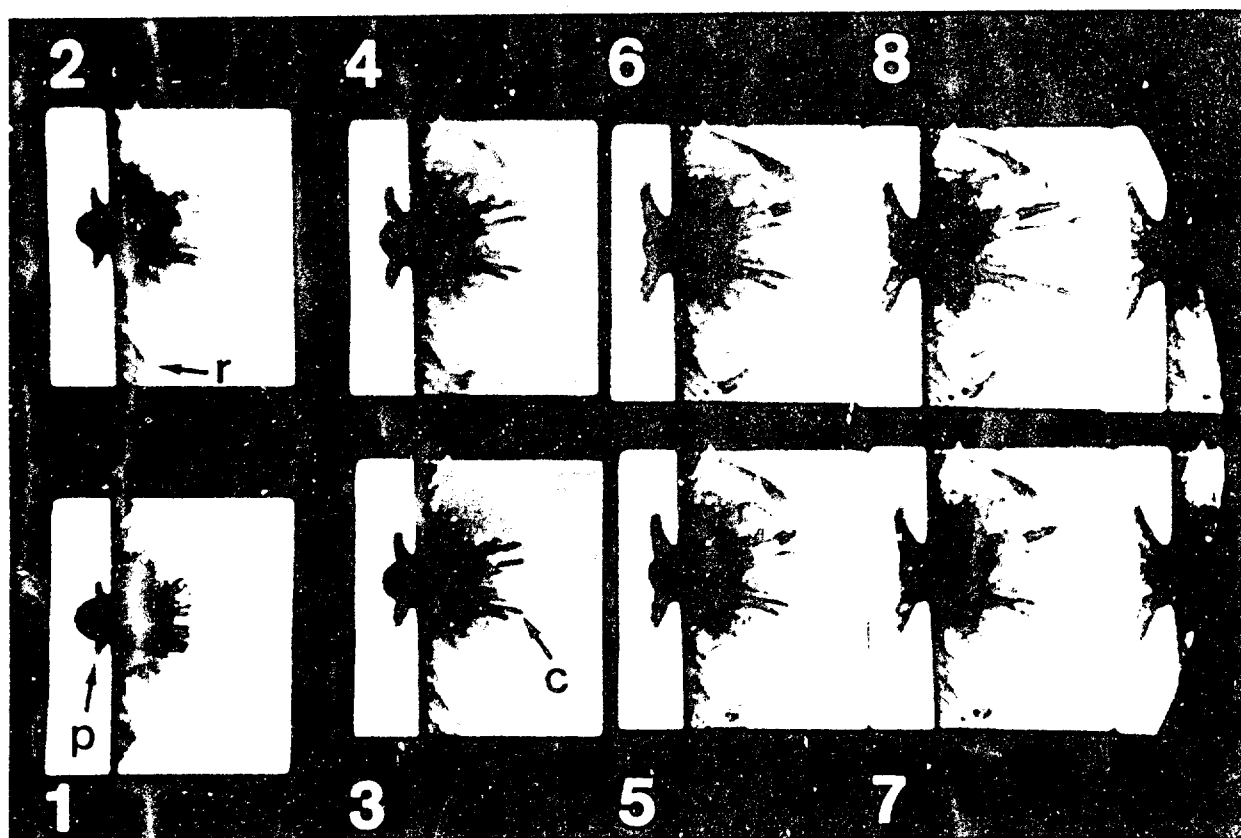
**b)**



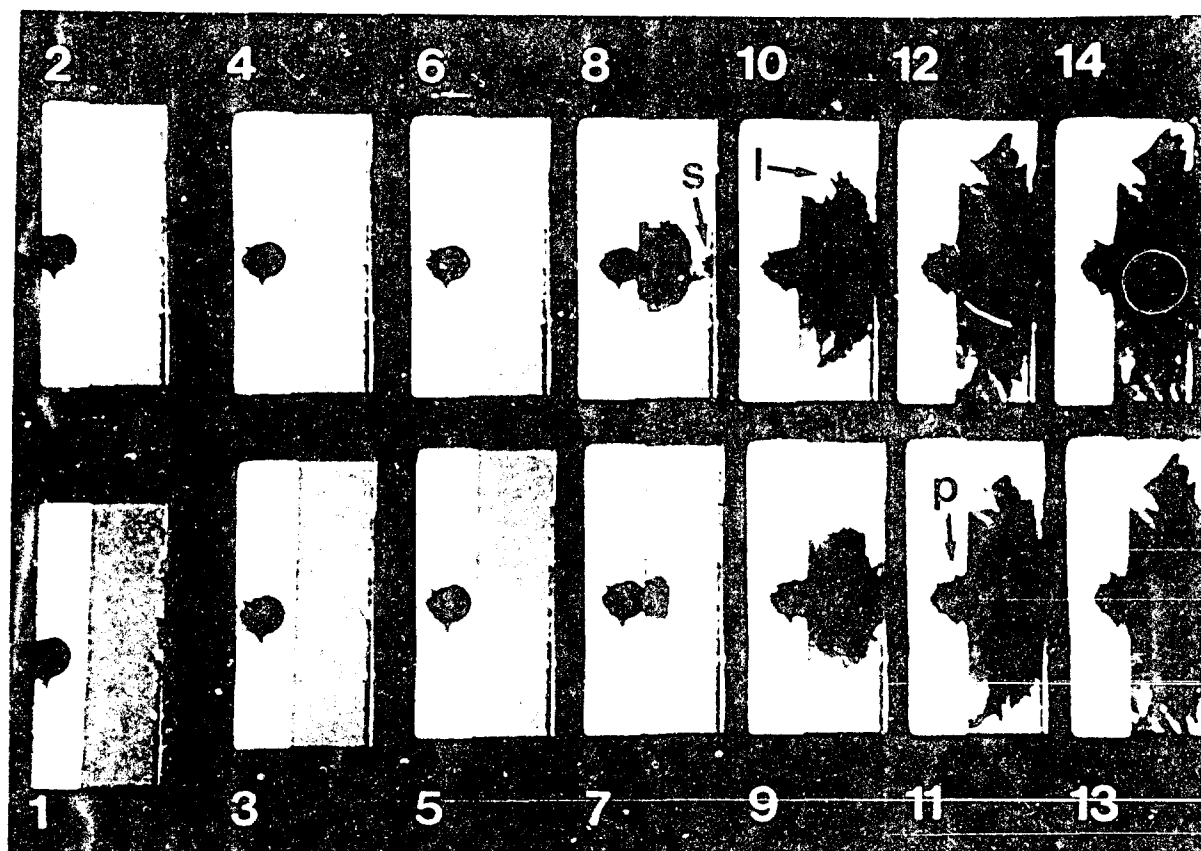
a



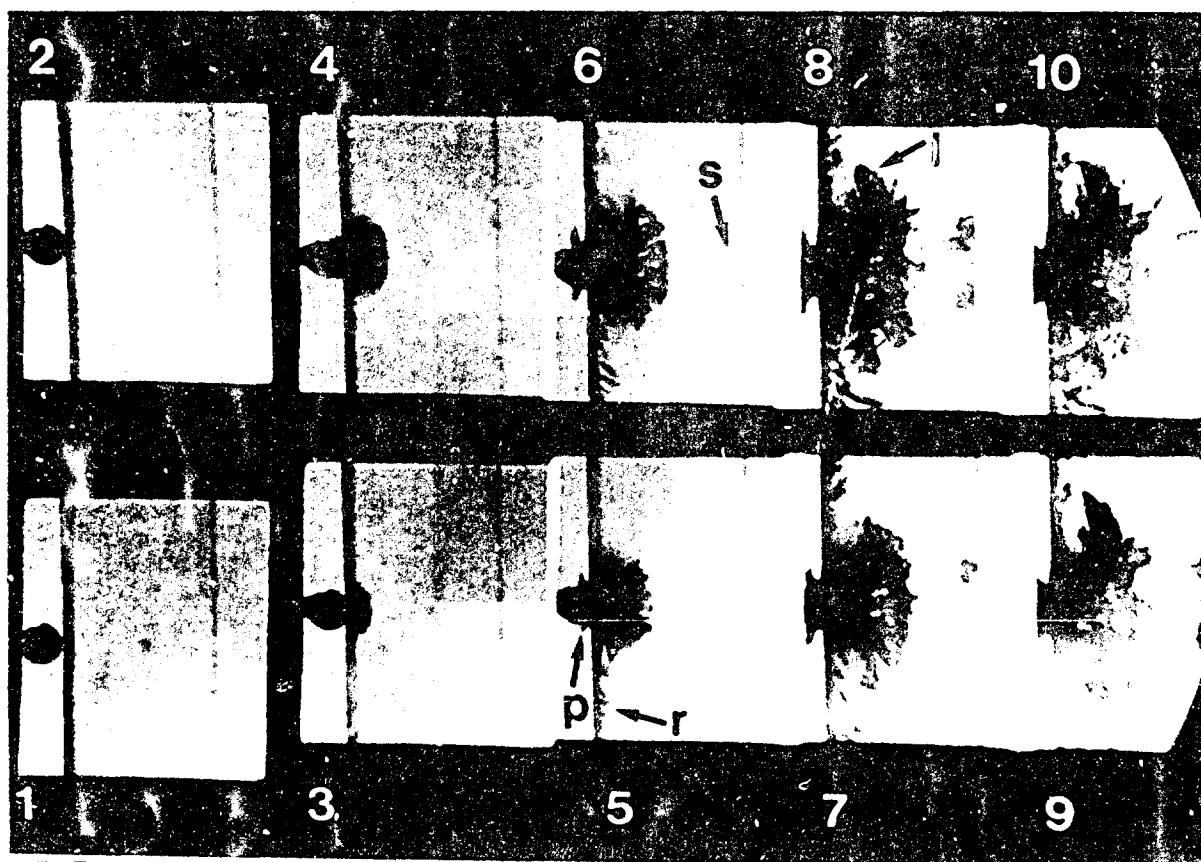
b

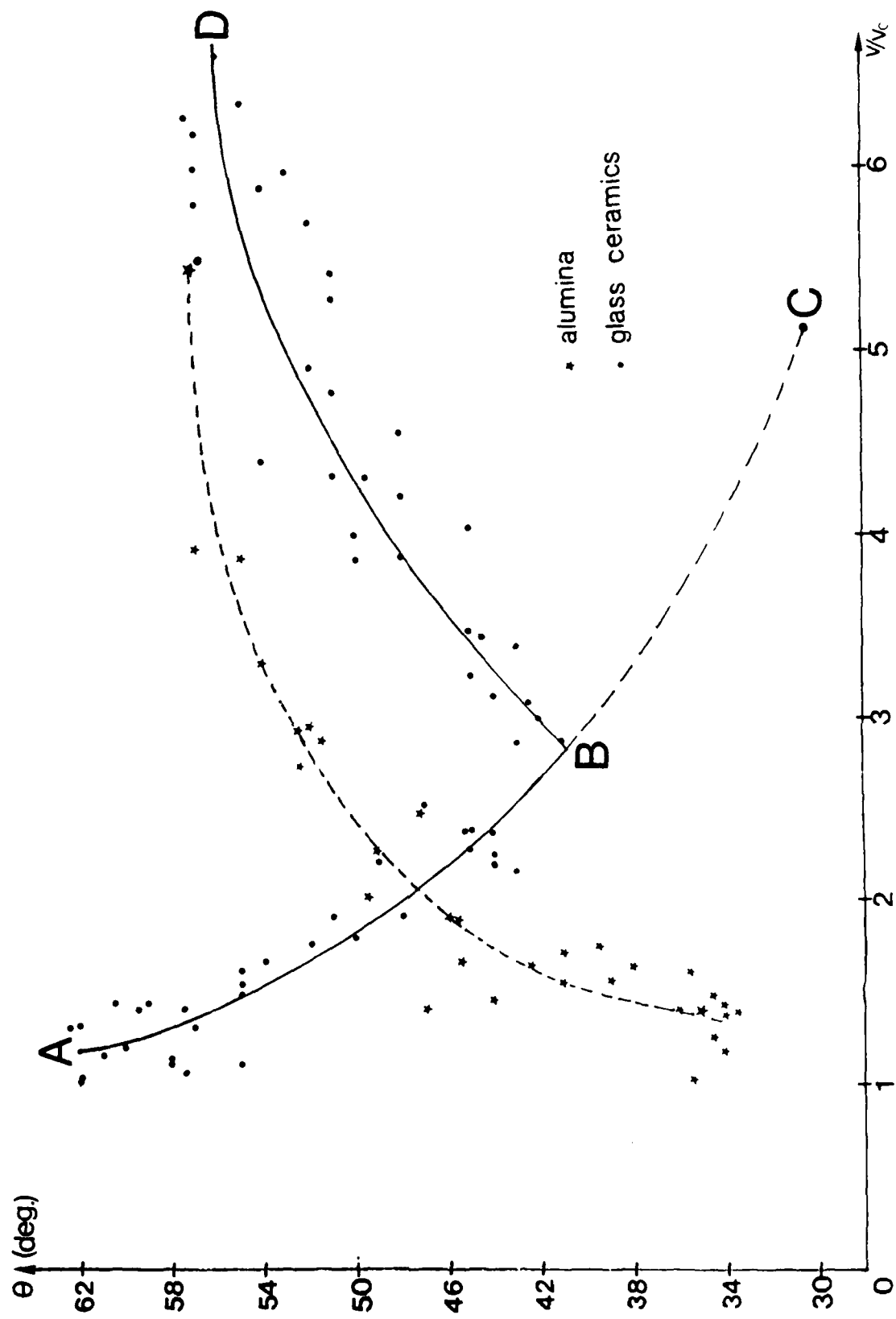


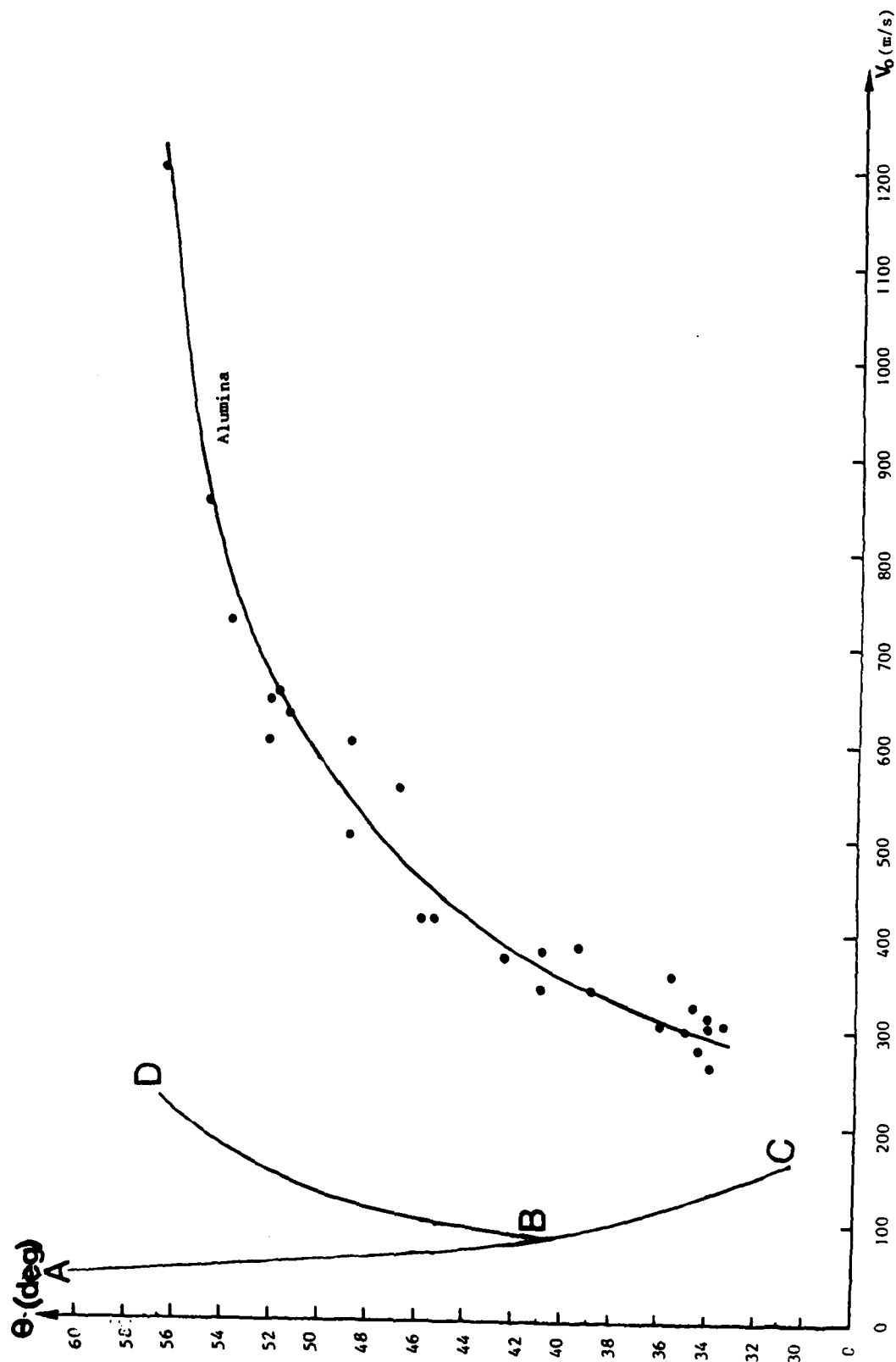
a



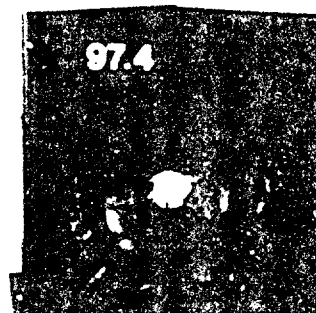
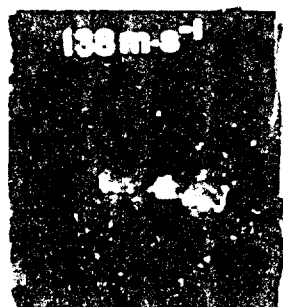
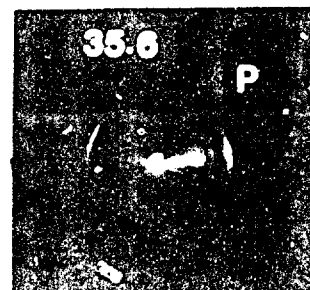
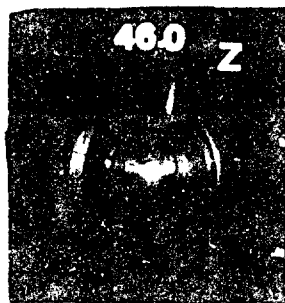
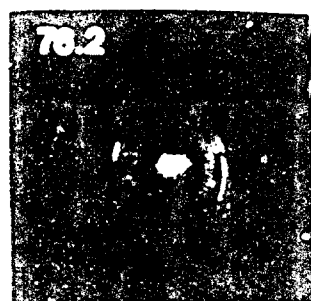
b



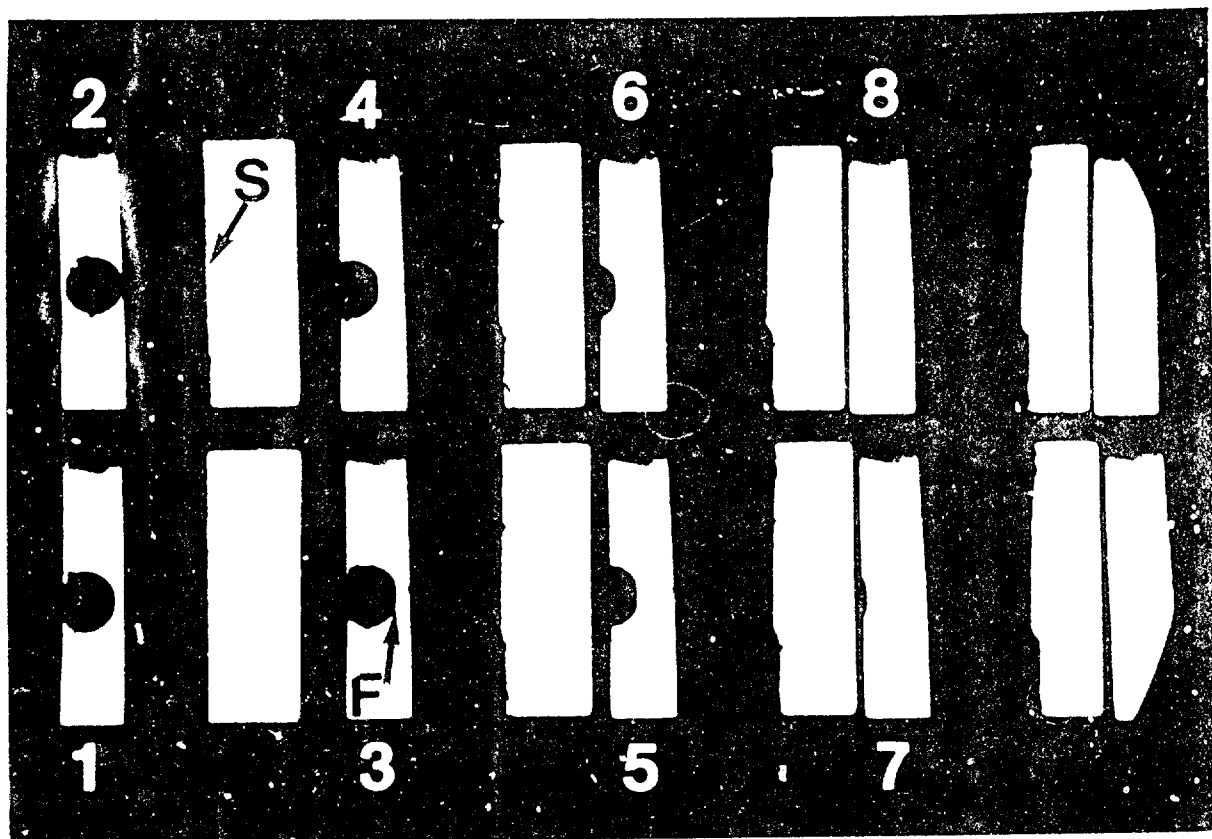




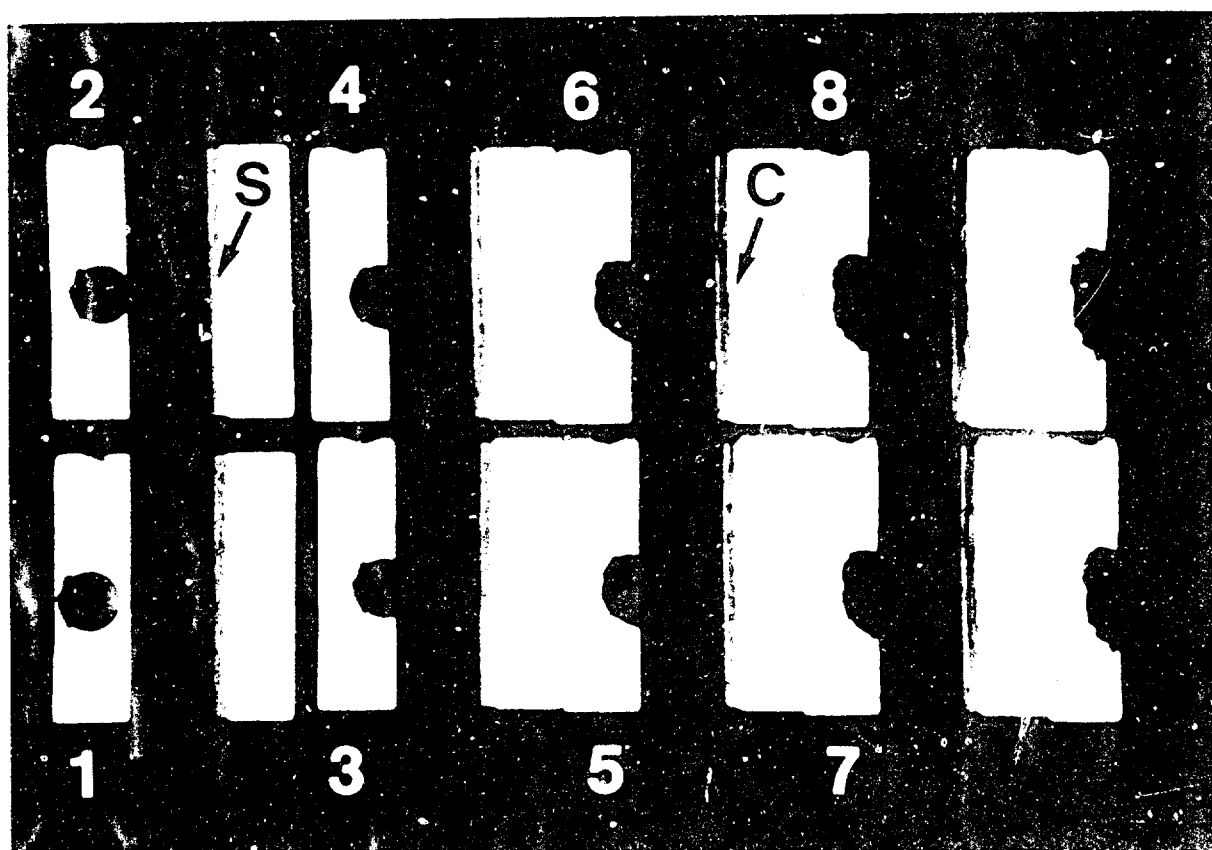


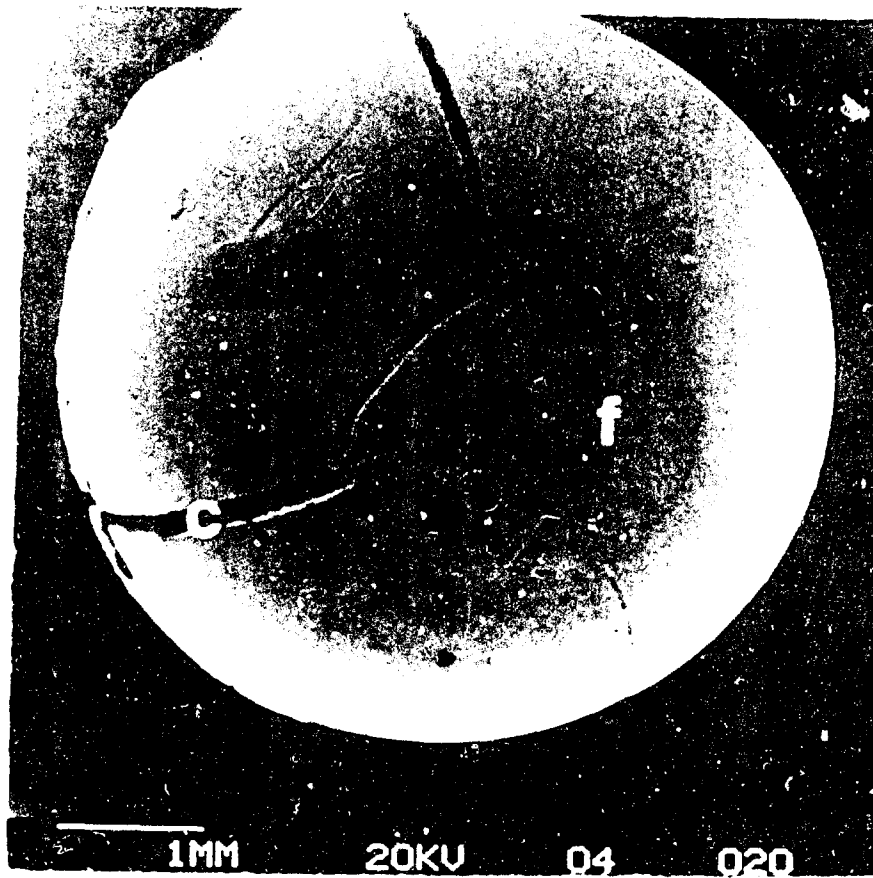


a

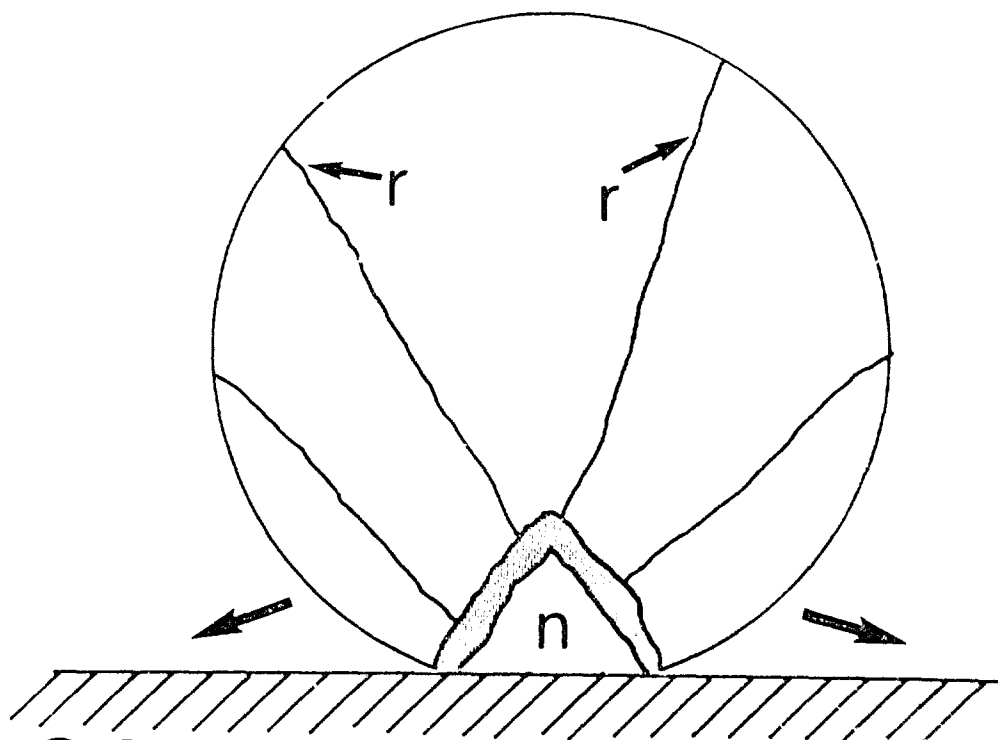


b

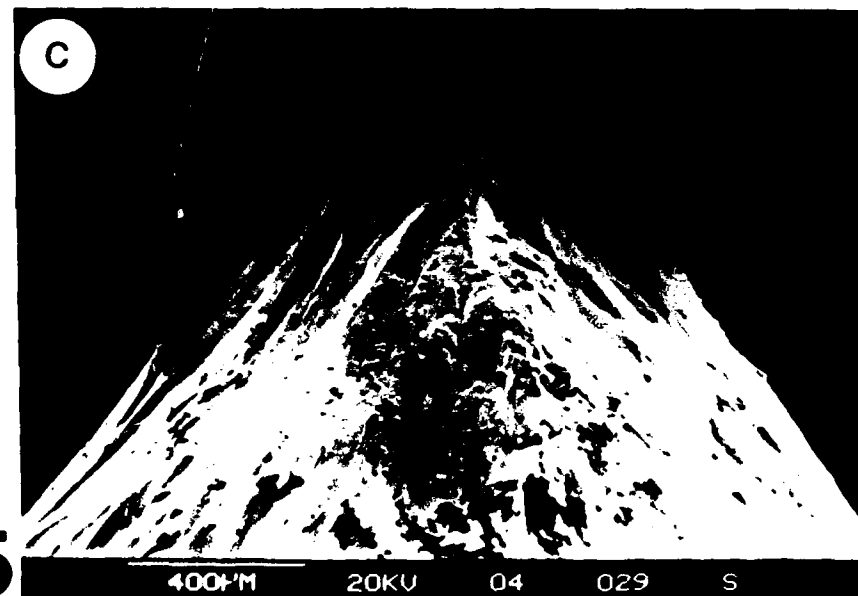
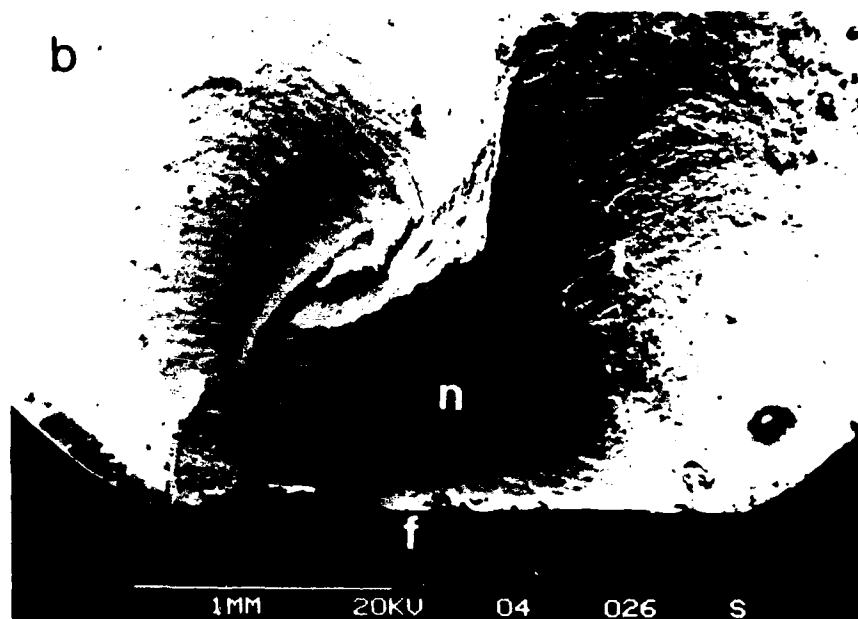
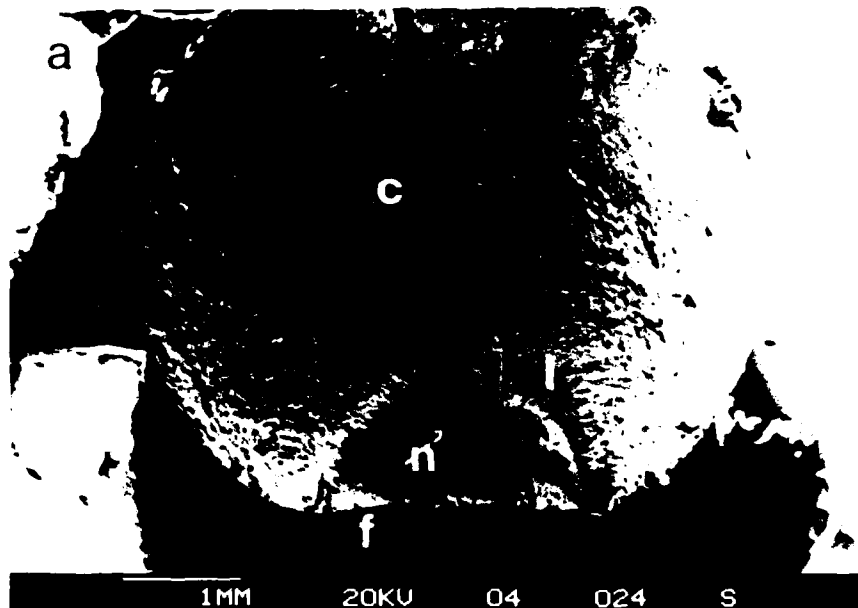


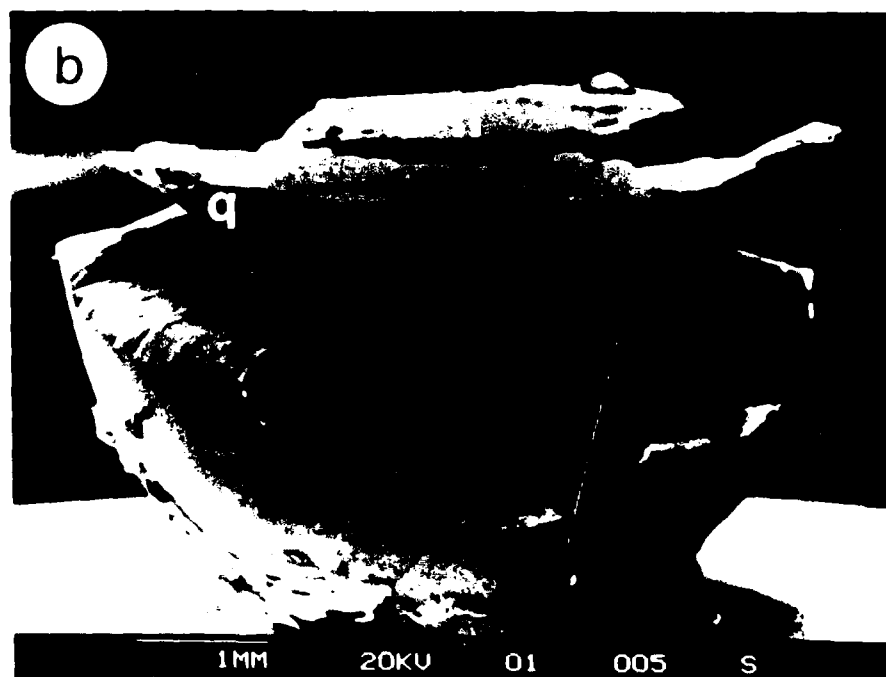
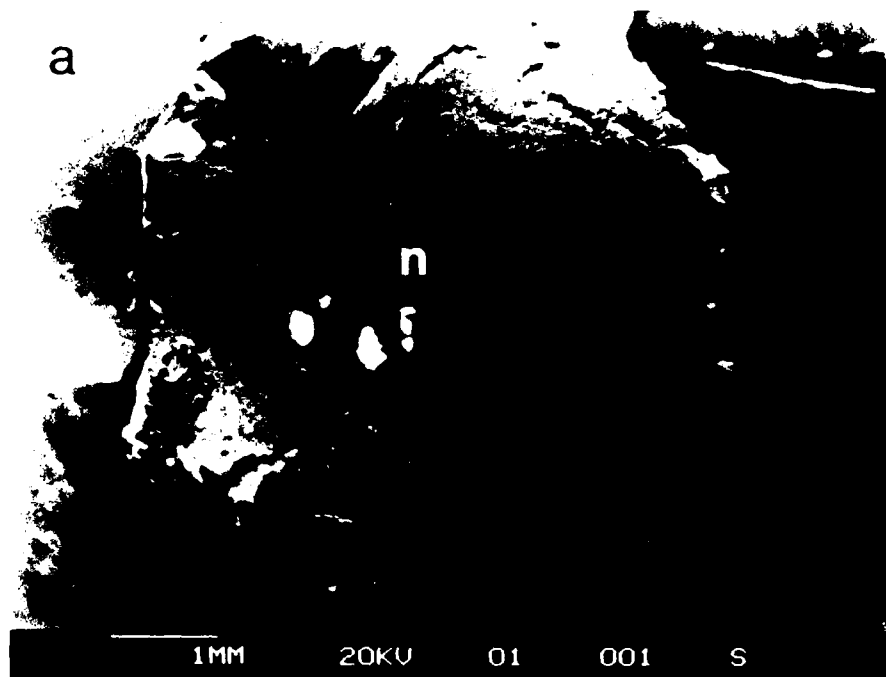


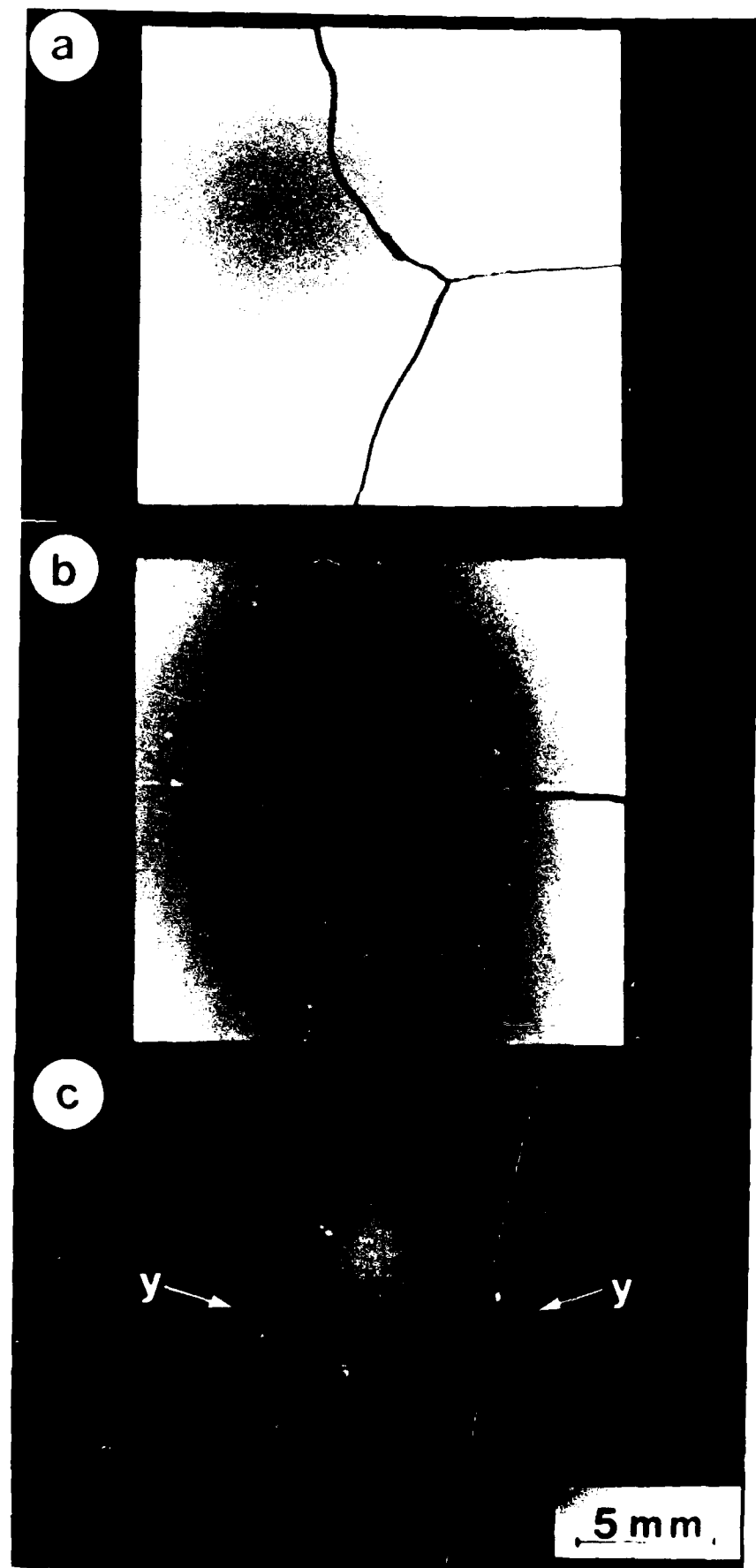
23

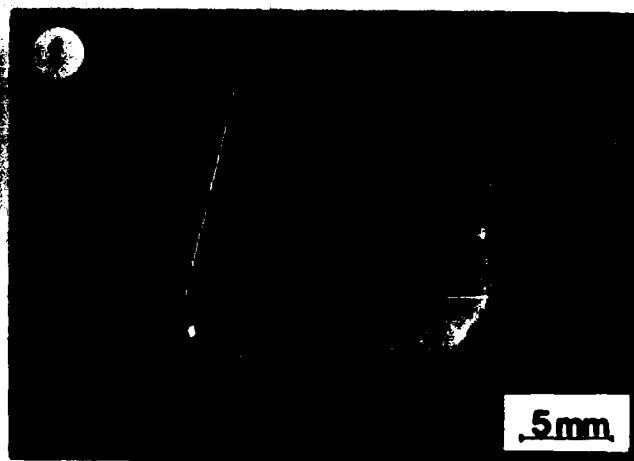
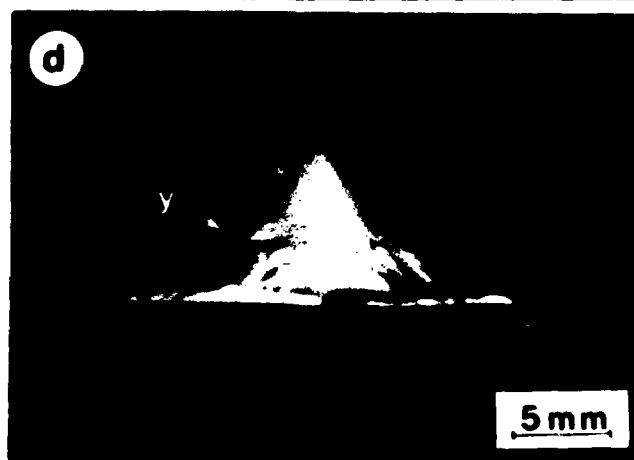
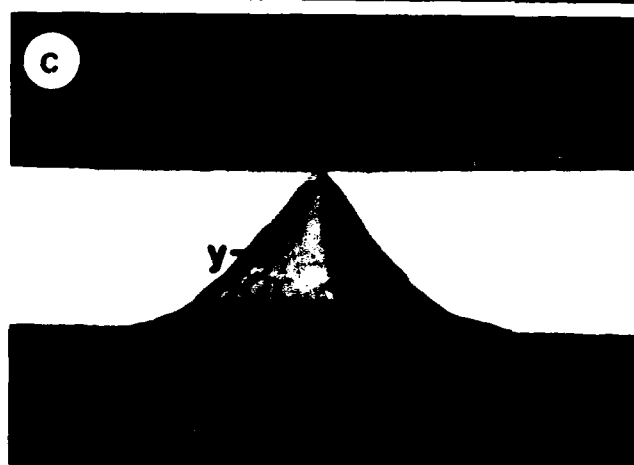
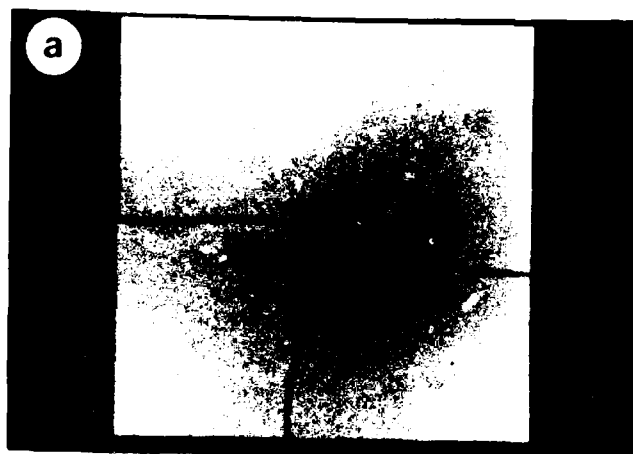


24











V=302m/s



V=328m/s



V=356m/s



V=385m/s



V=412m/s



V=550m/s

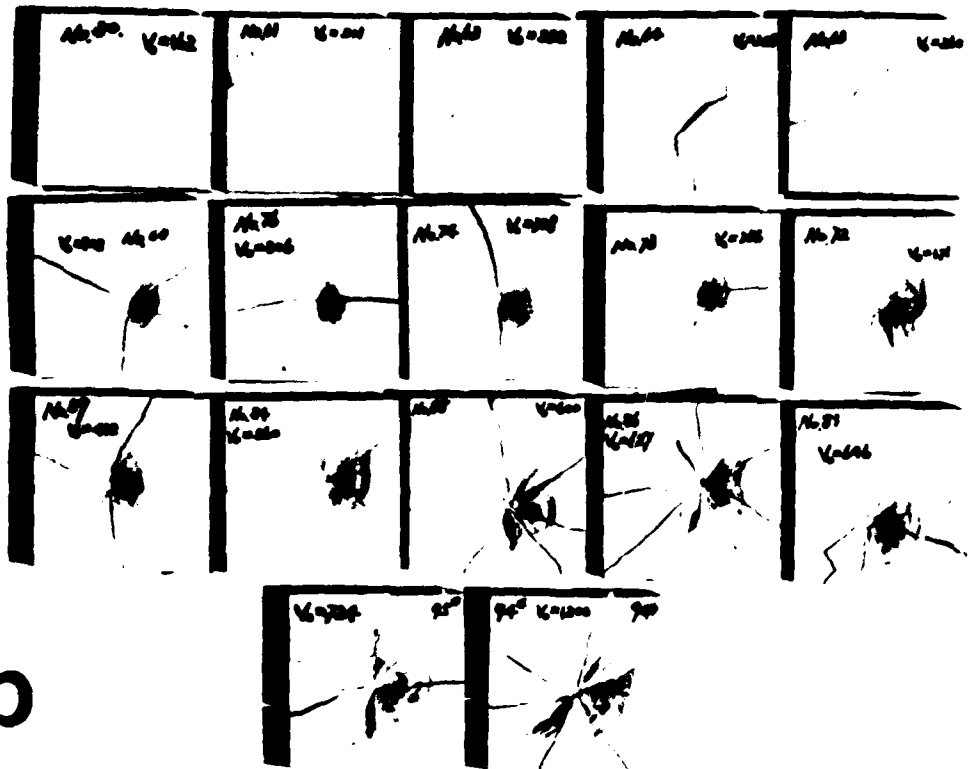


V=600m/s



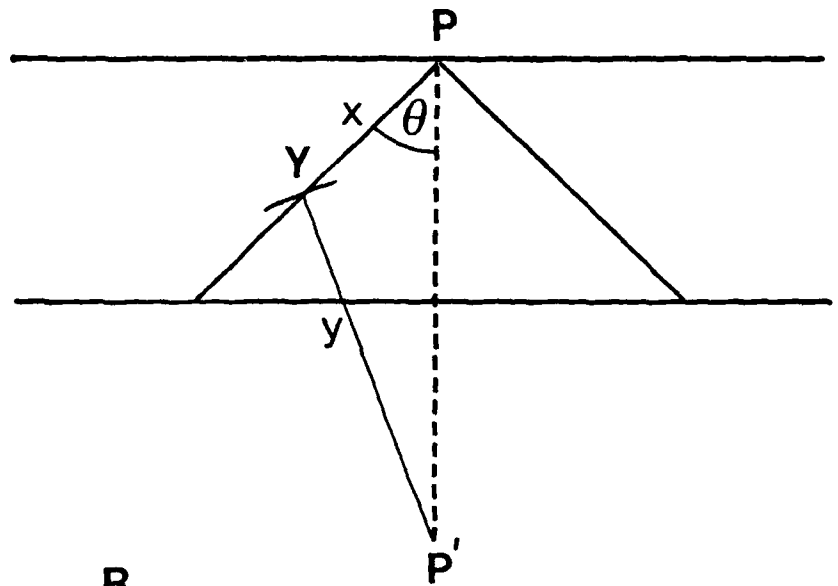
V=646m/s

a

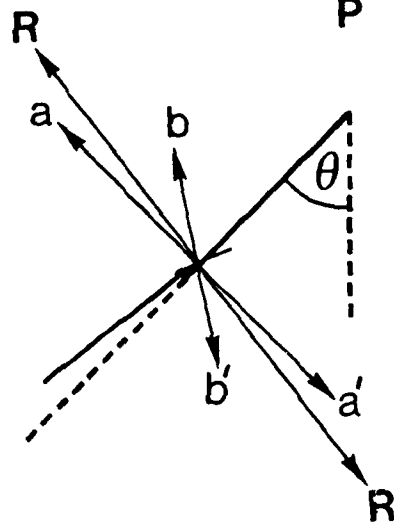




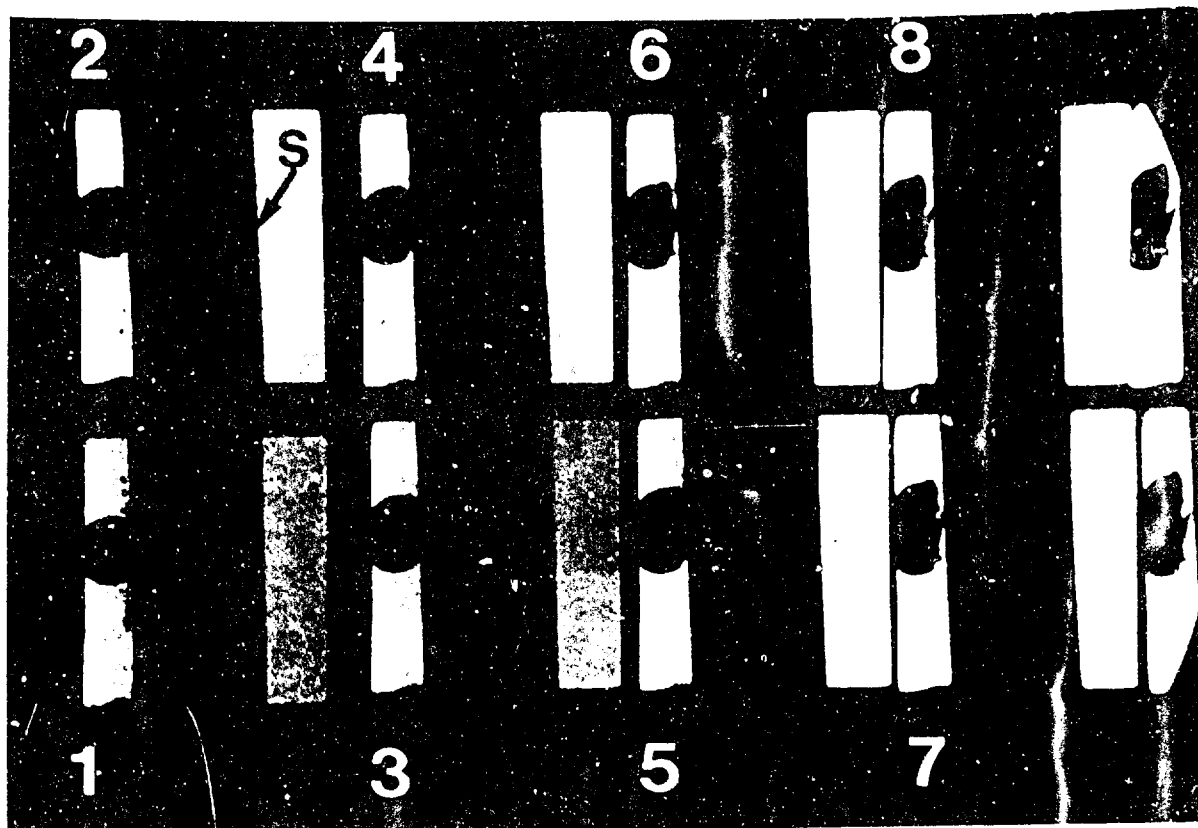
a)



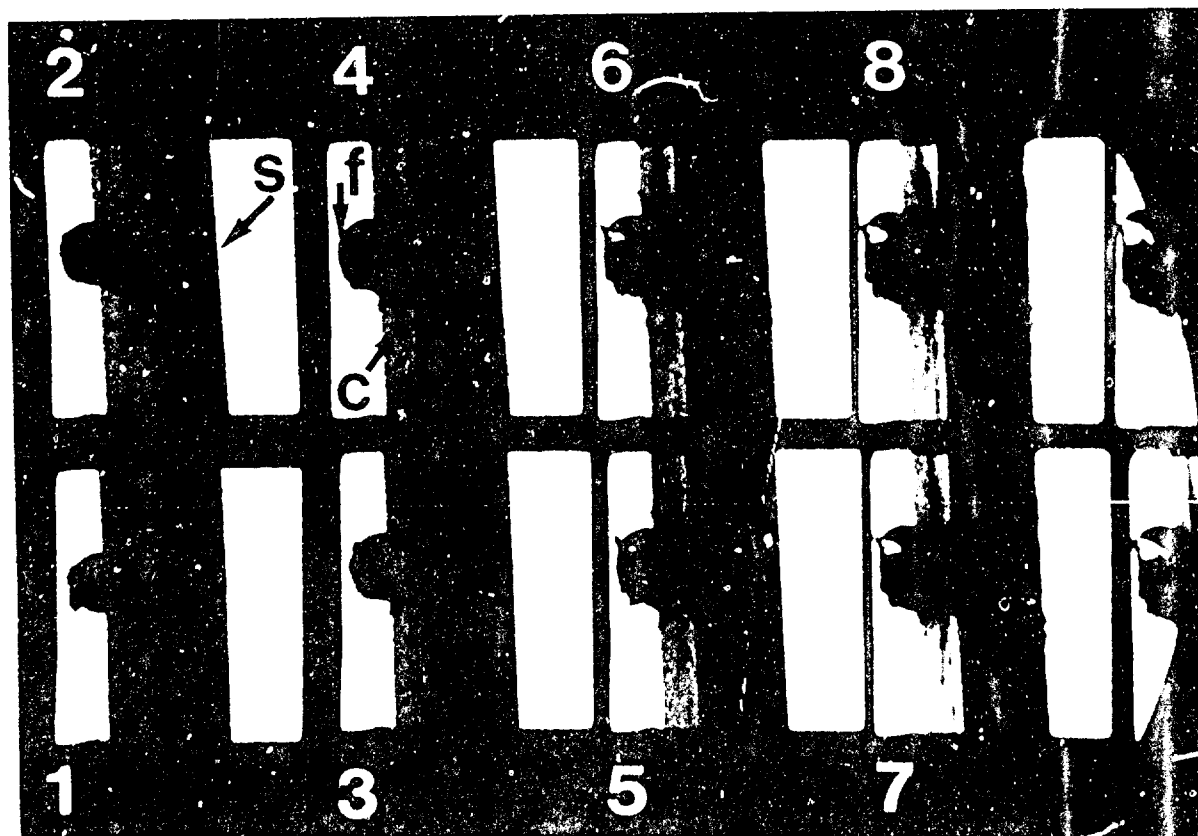
b)



a



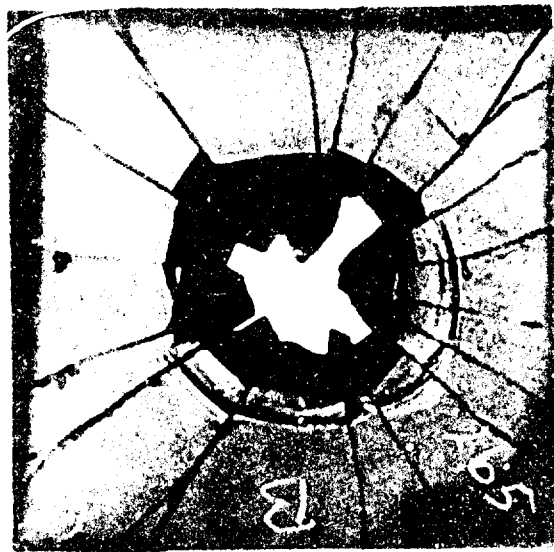
b



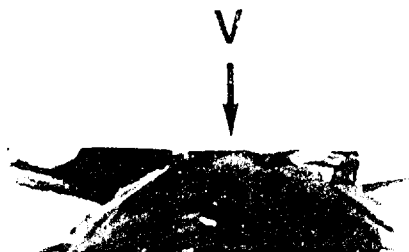
a



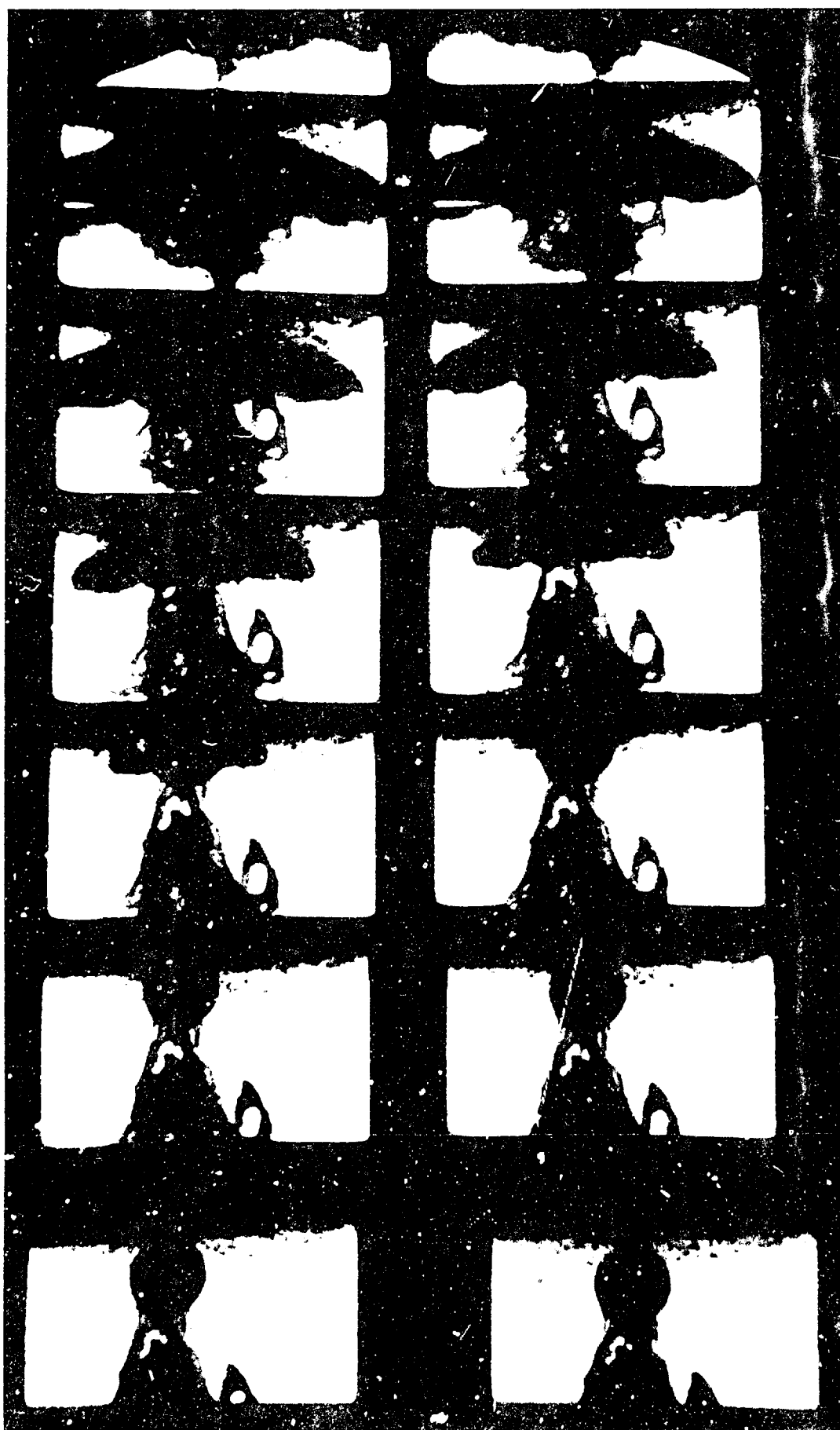
b

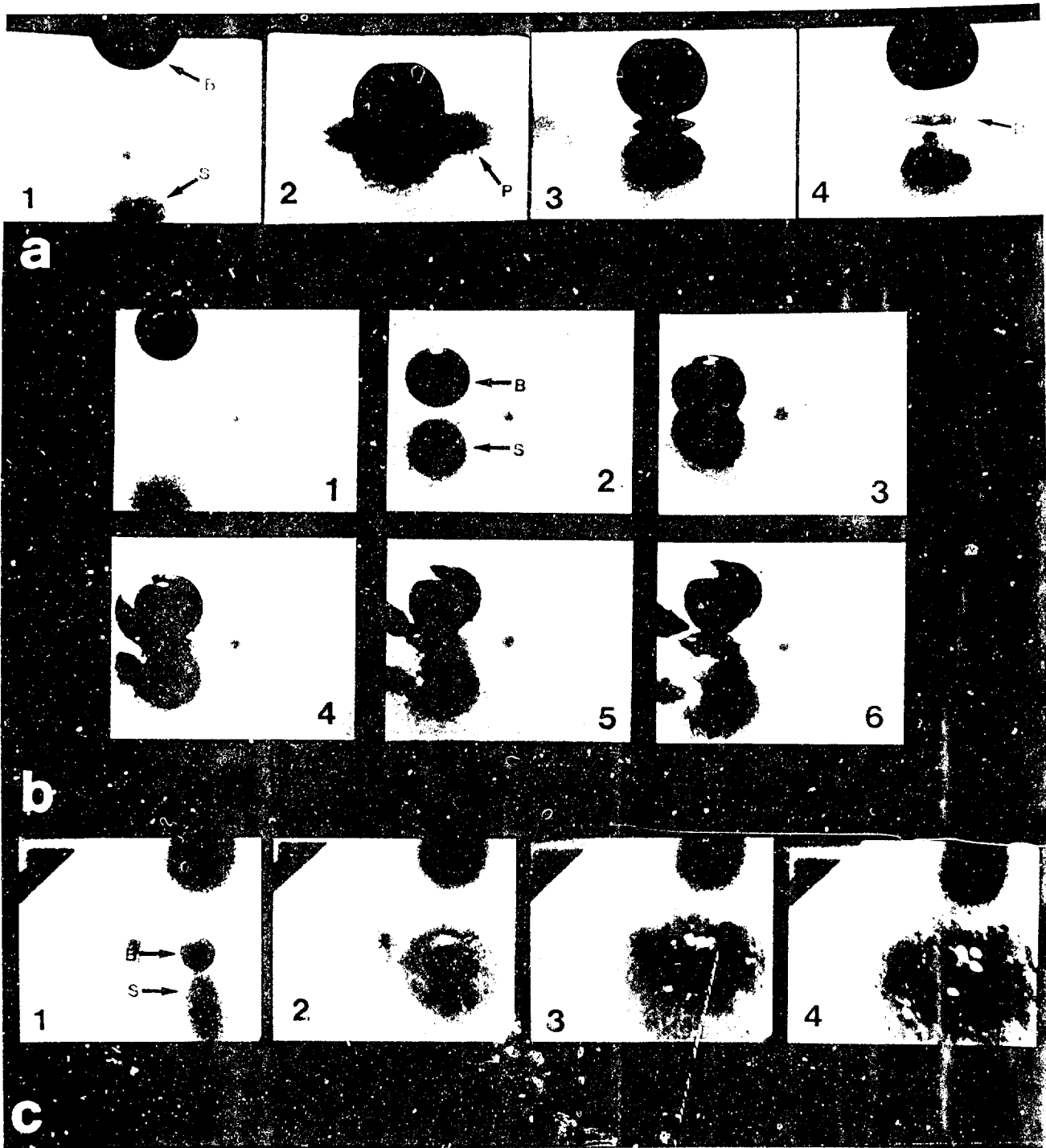


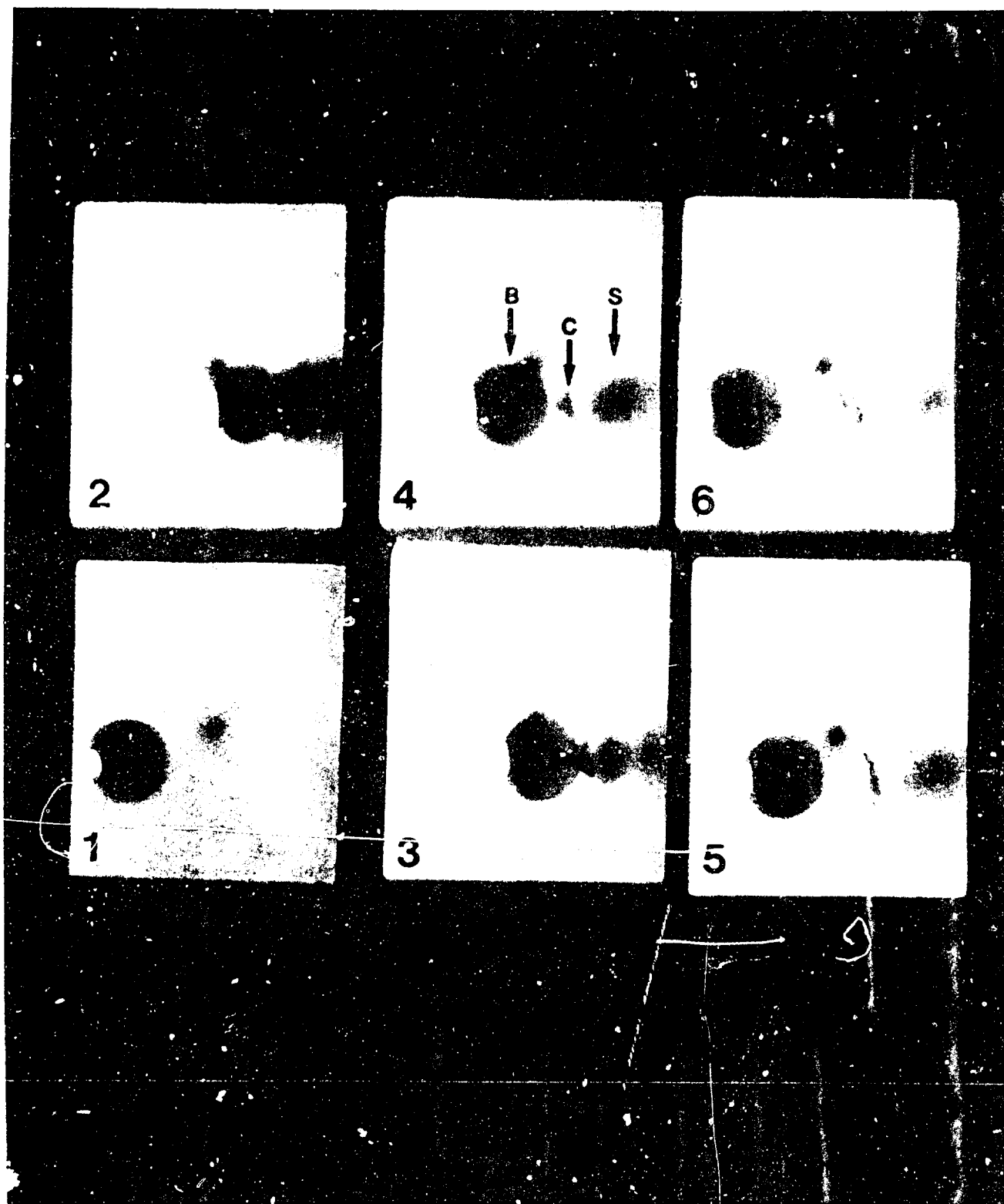
c



10mm

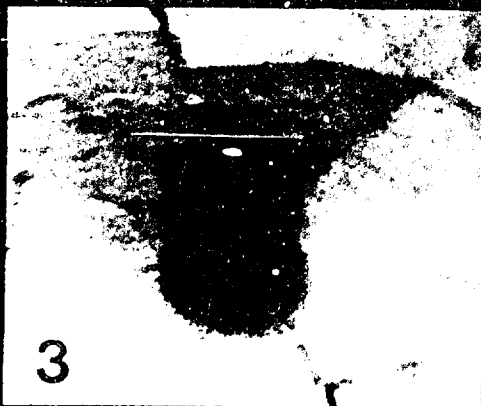
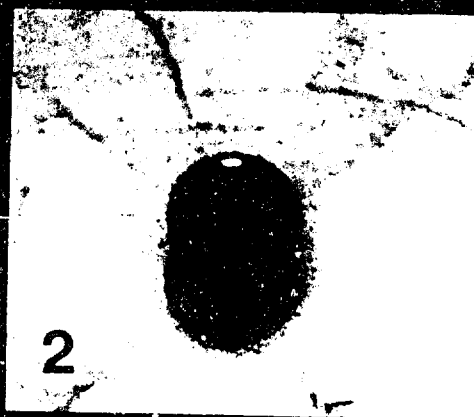
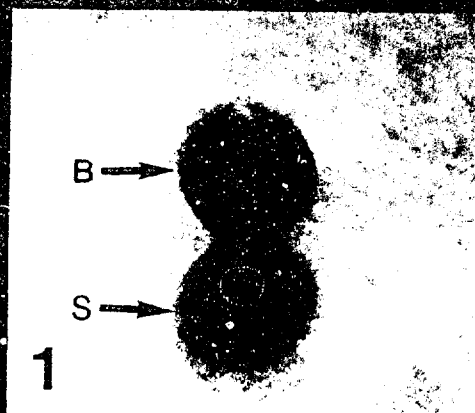




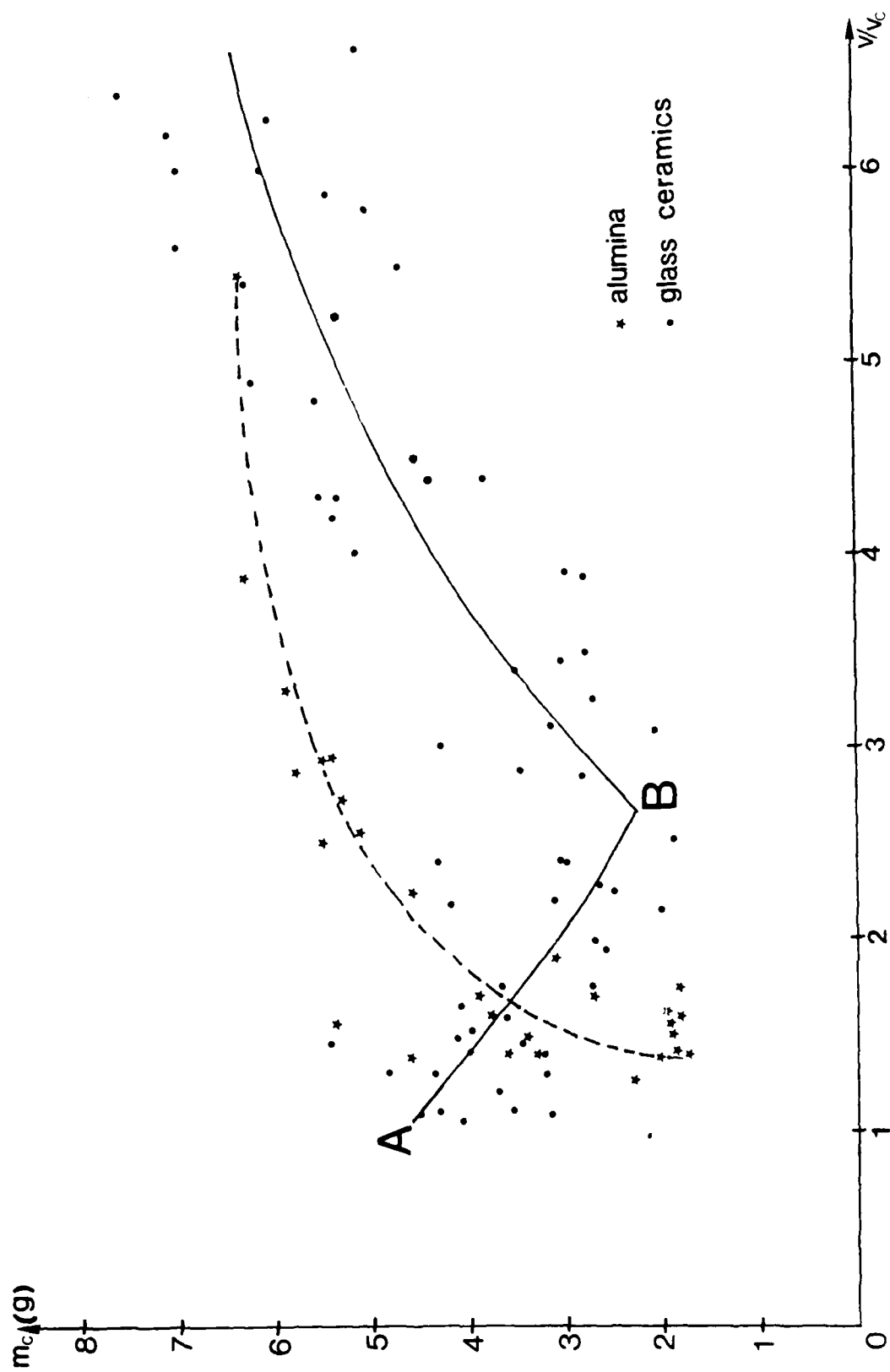




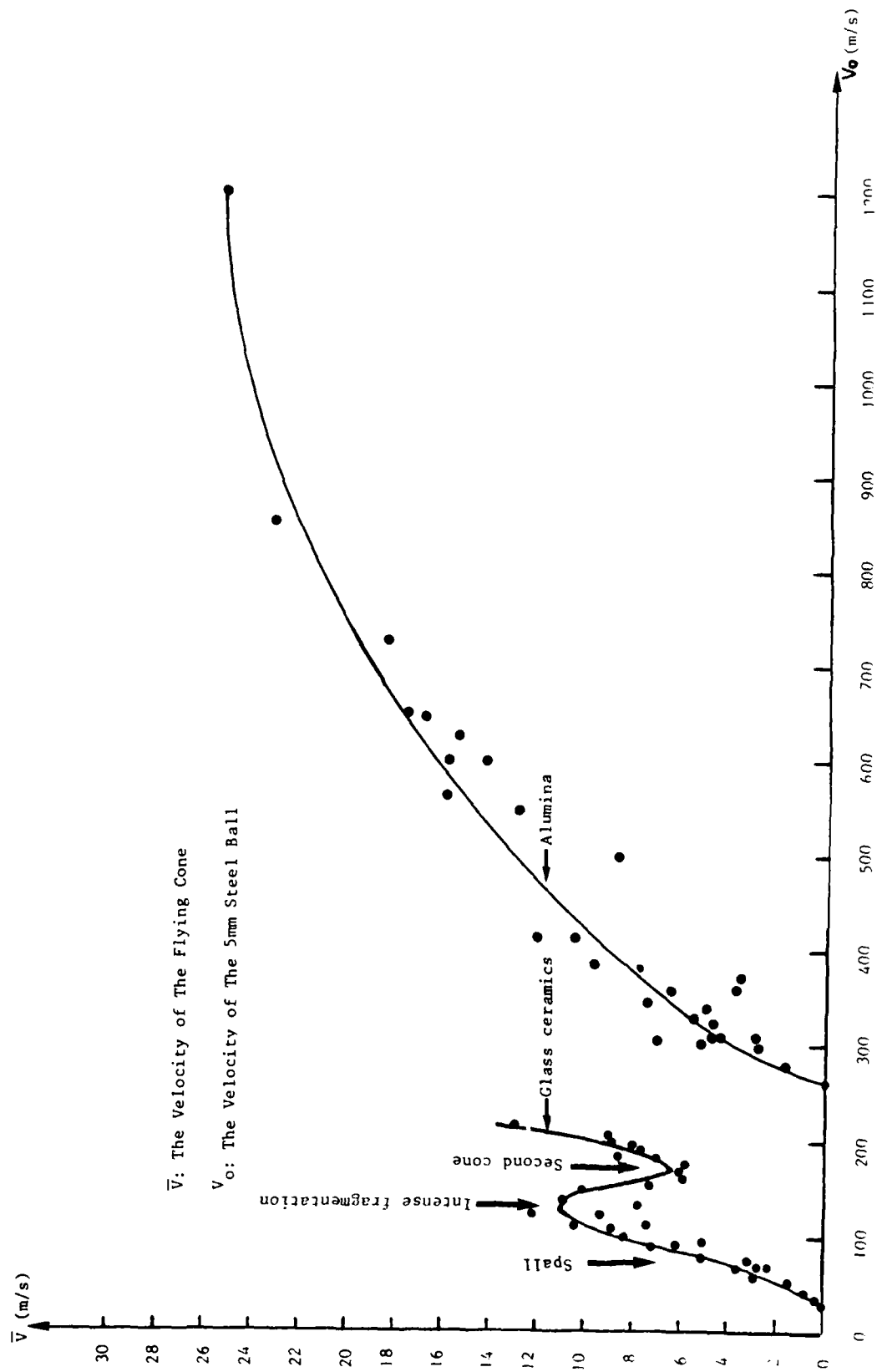
**a**

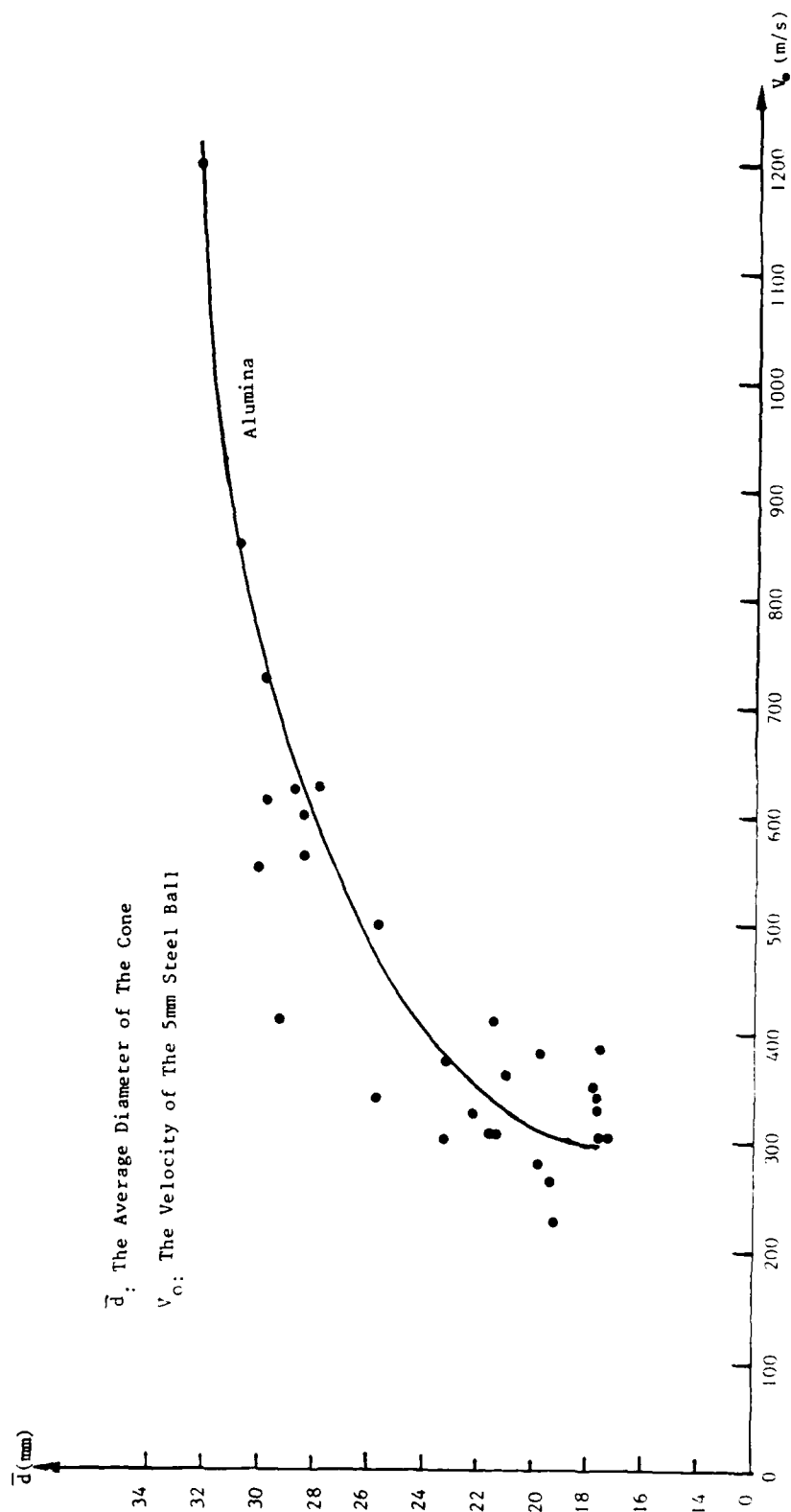


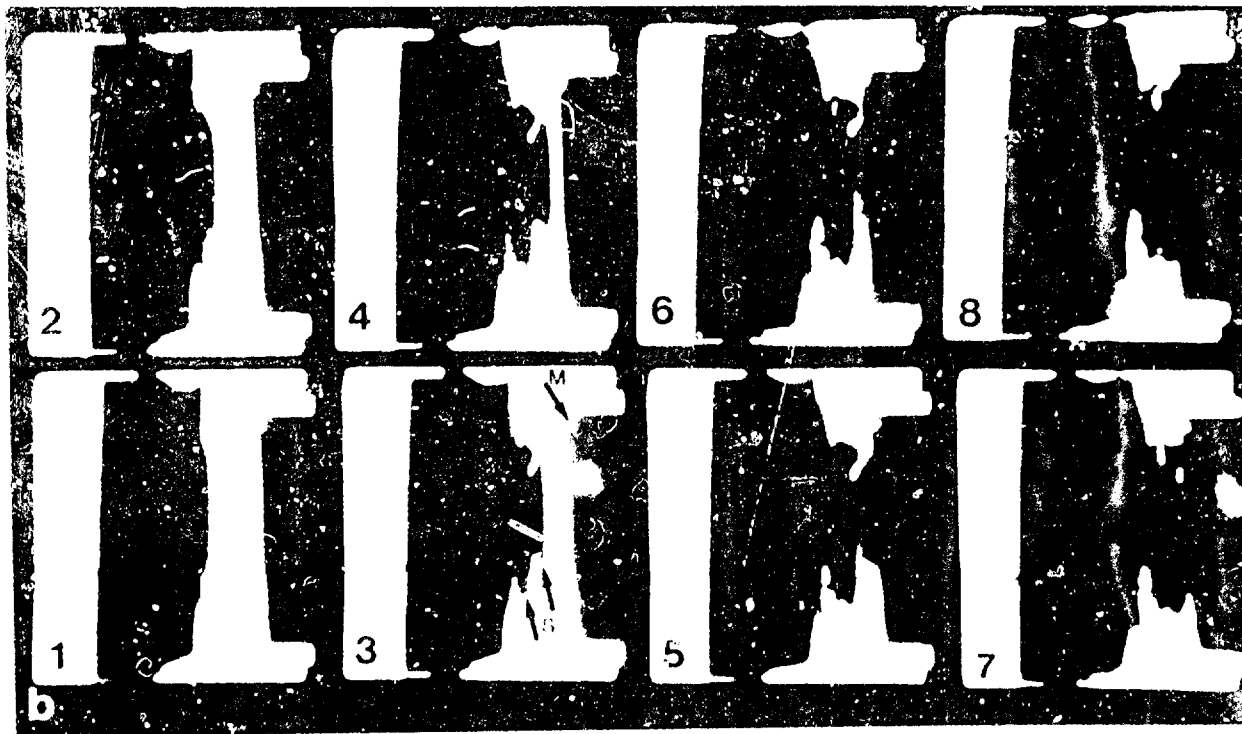
**b**

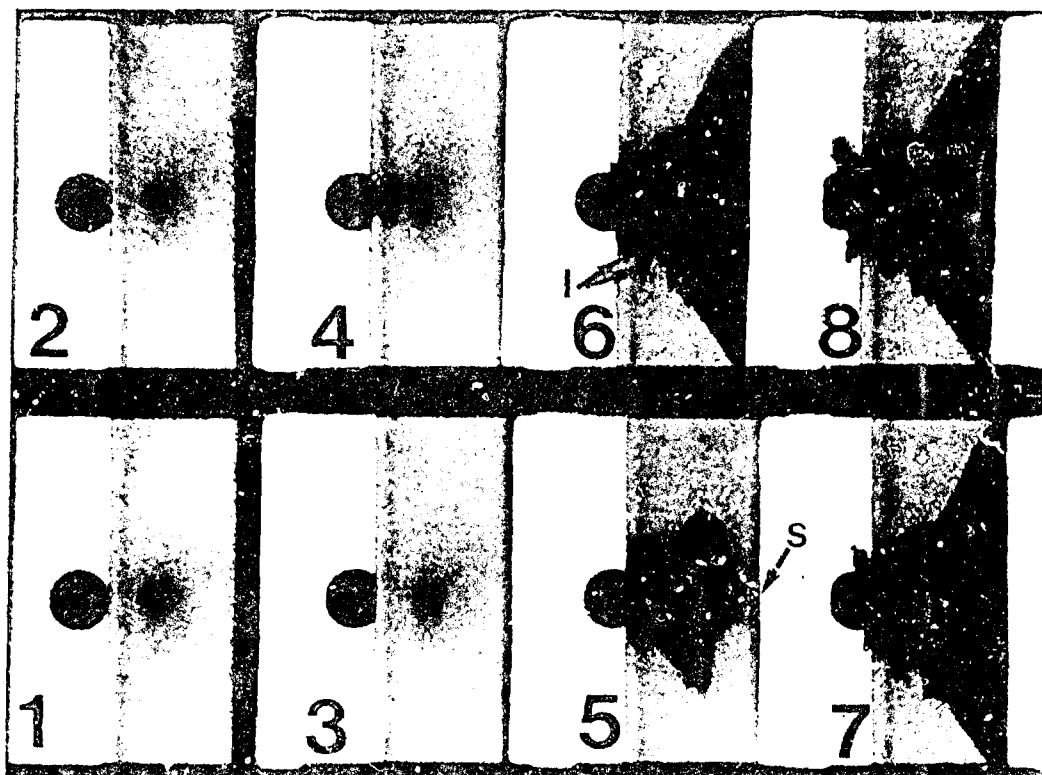




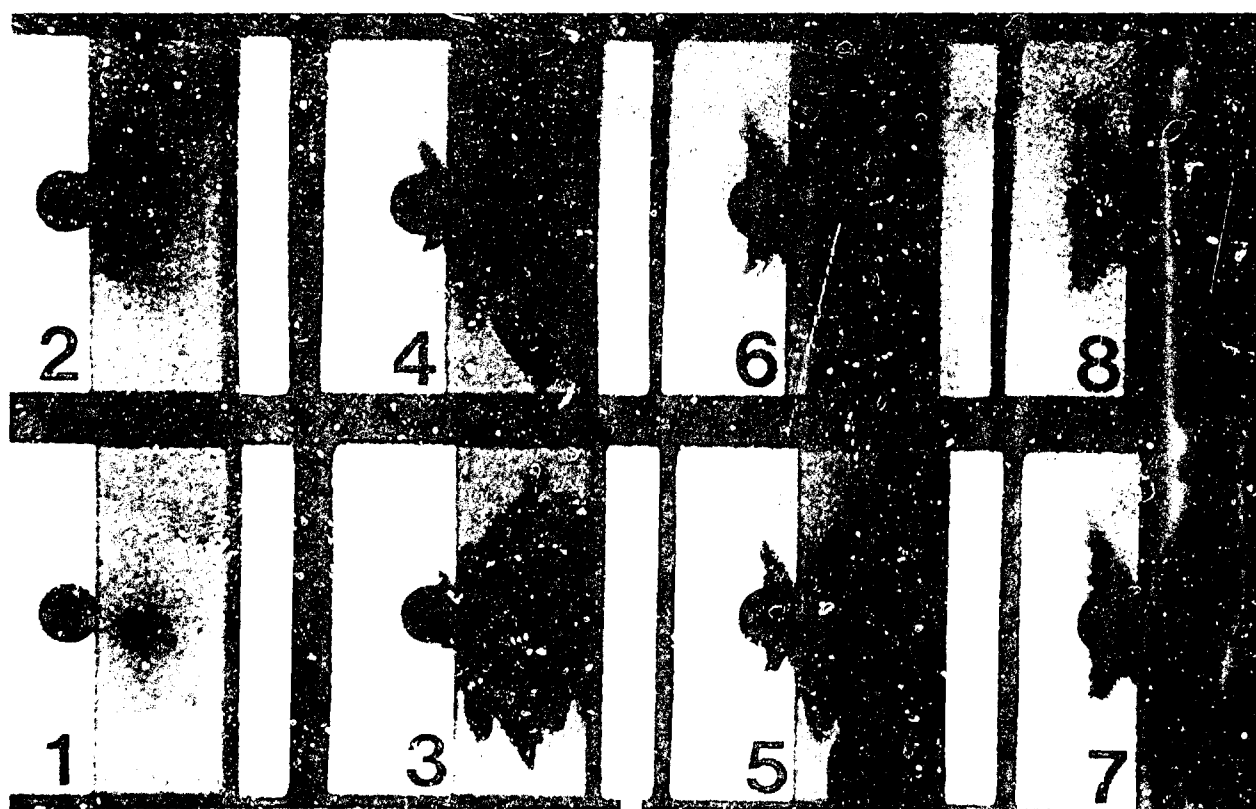




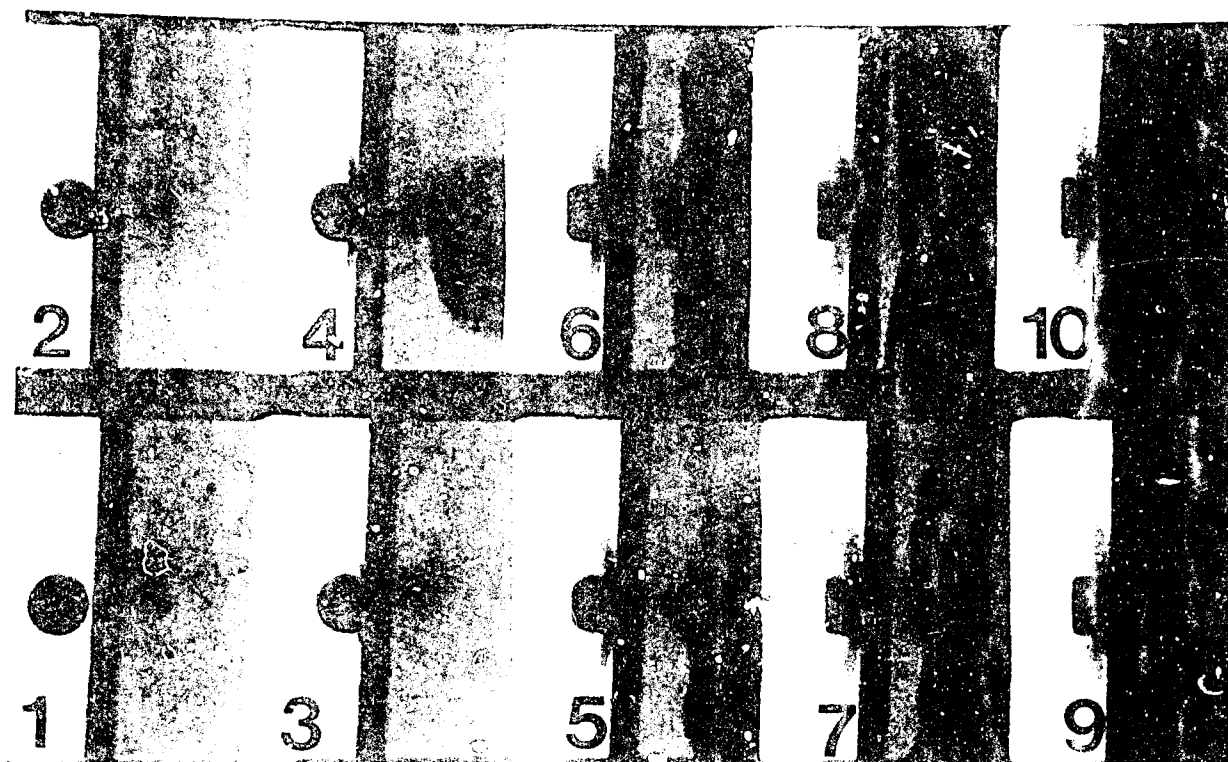




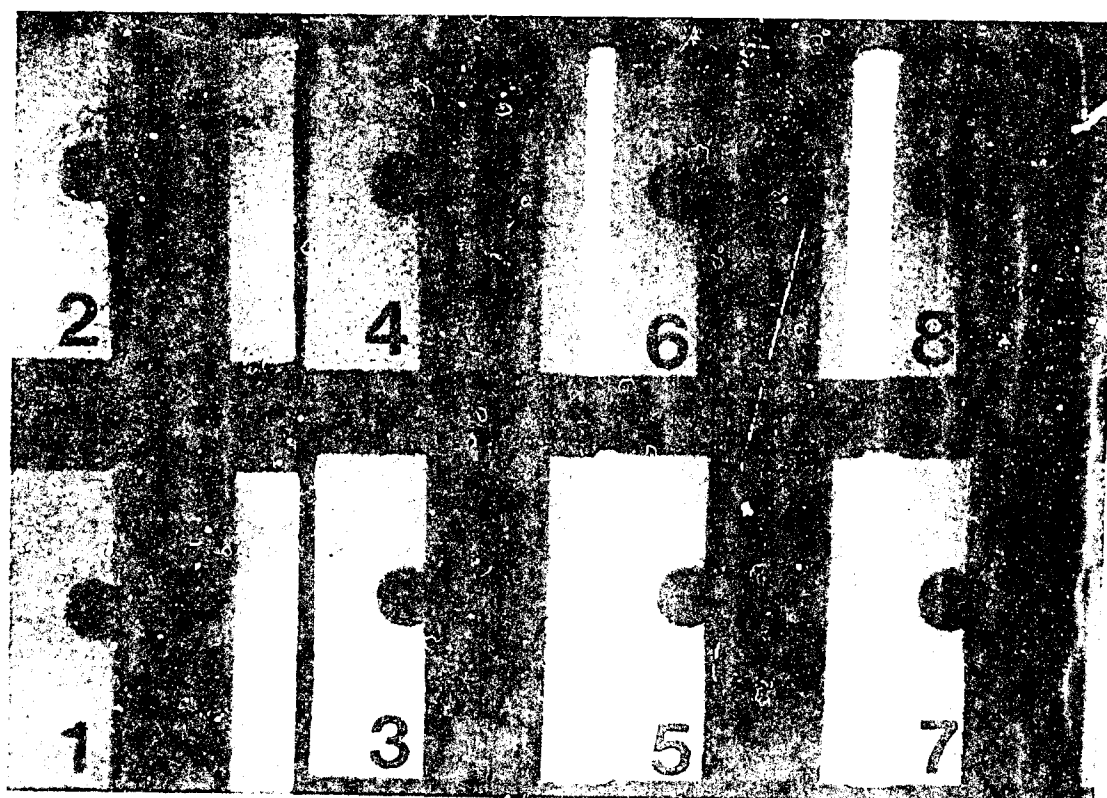
41



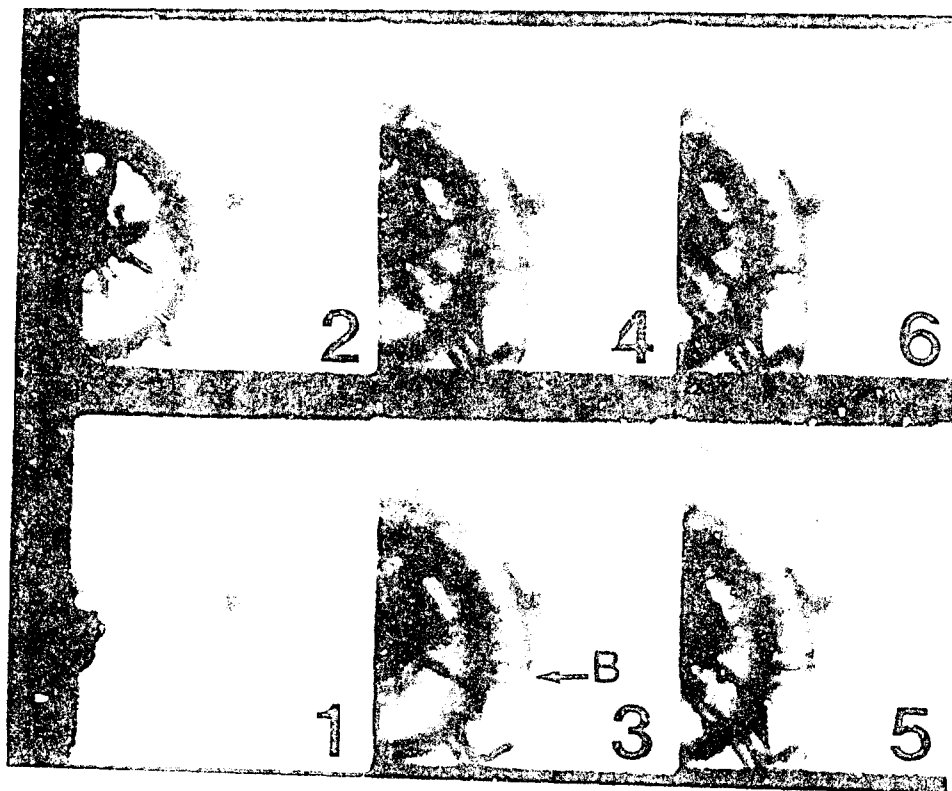
42



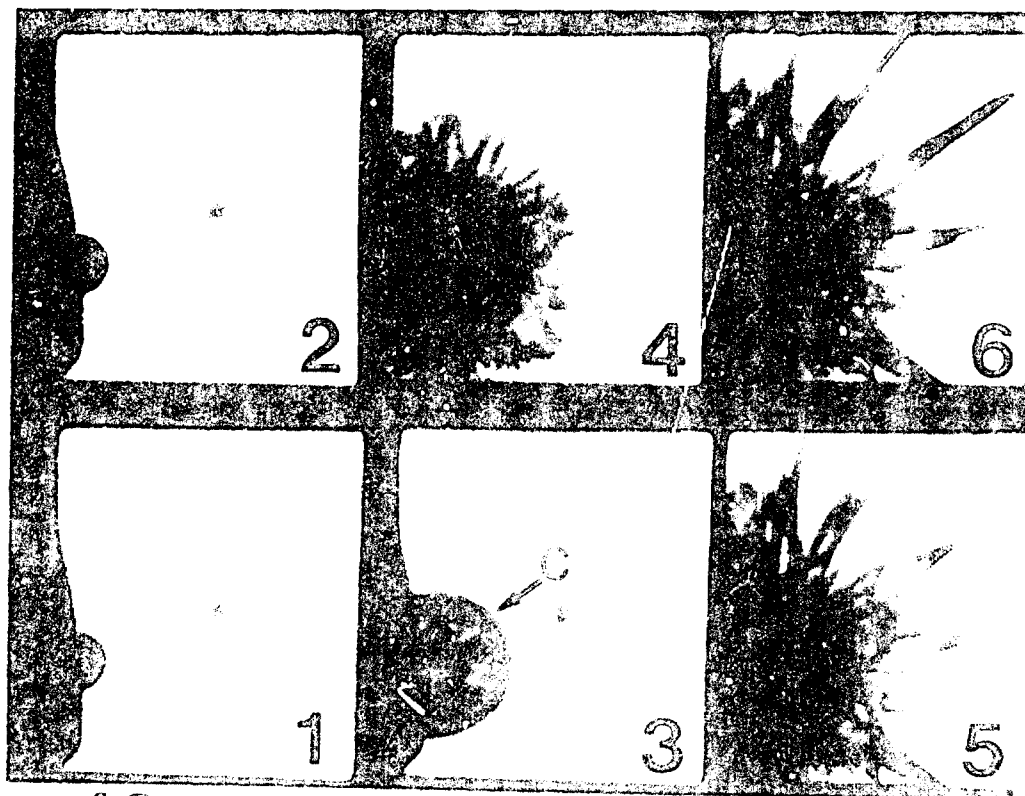
43



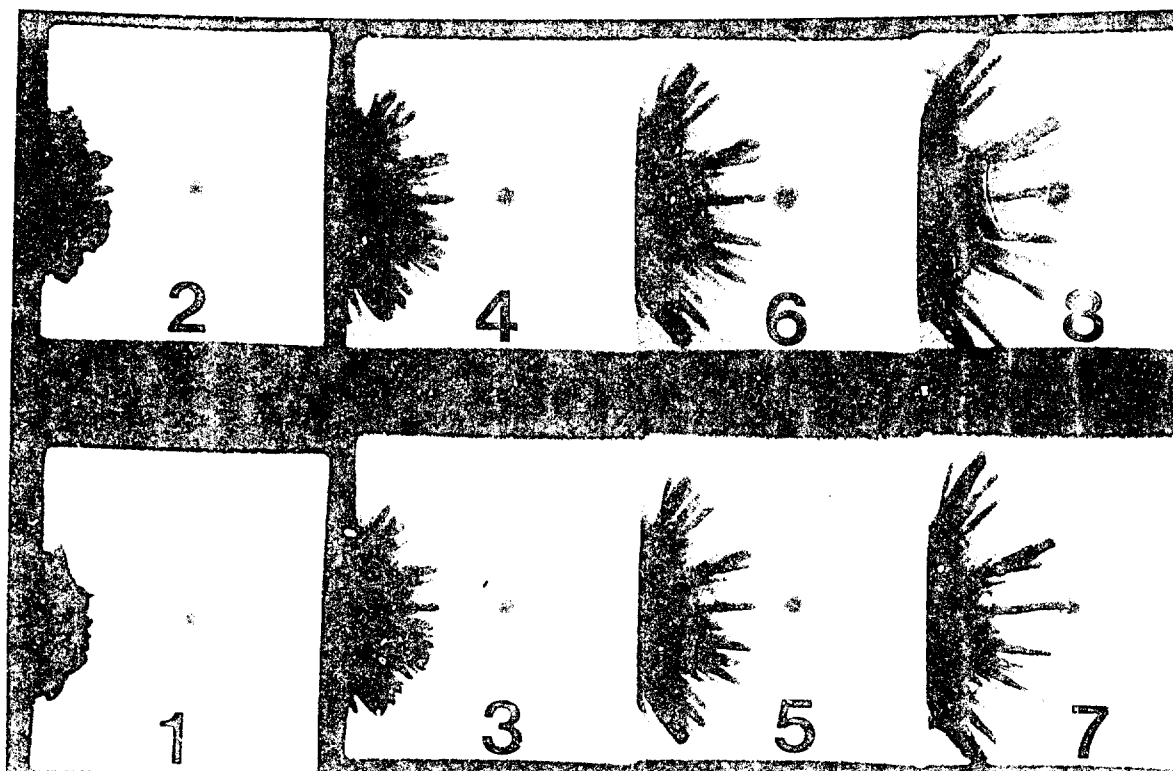
44



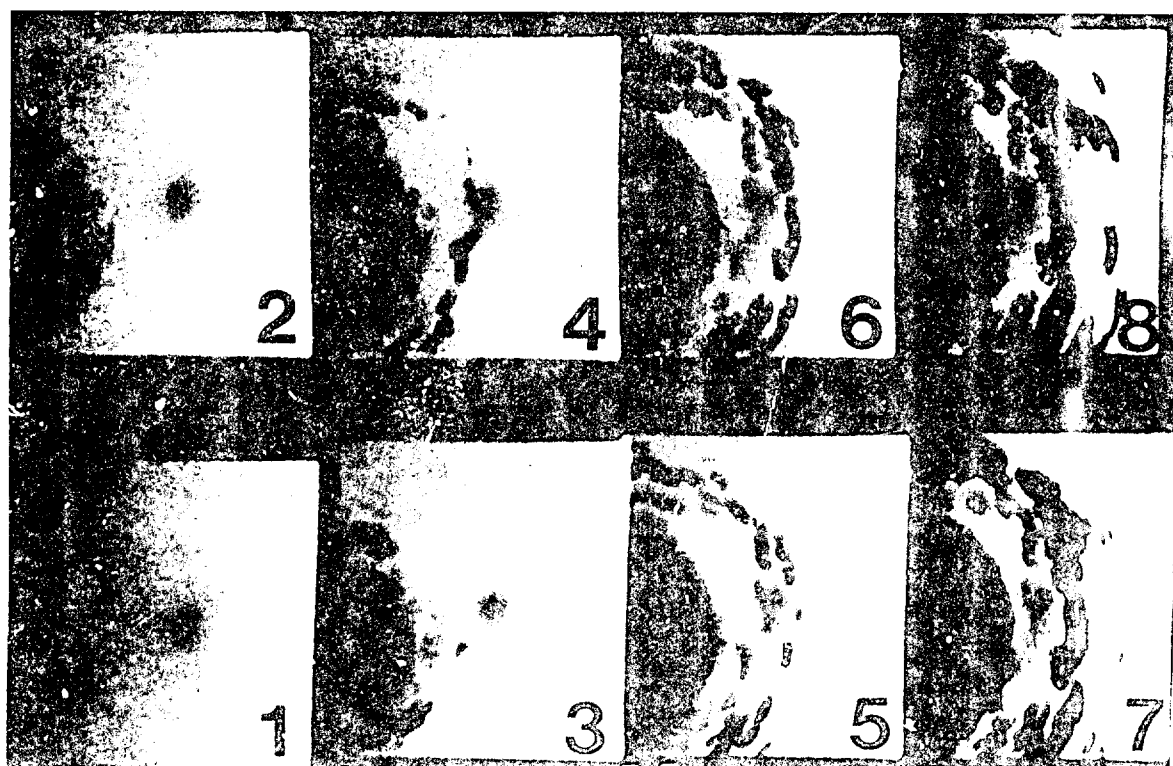
45



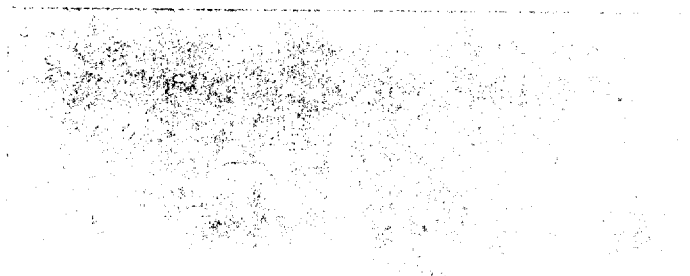
46



47



48



a

b



c



d



